Mid-infrared resonant nanostructures for in-vitro monitoring of polypeptides

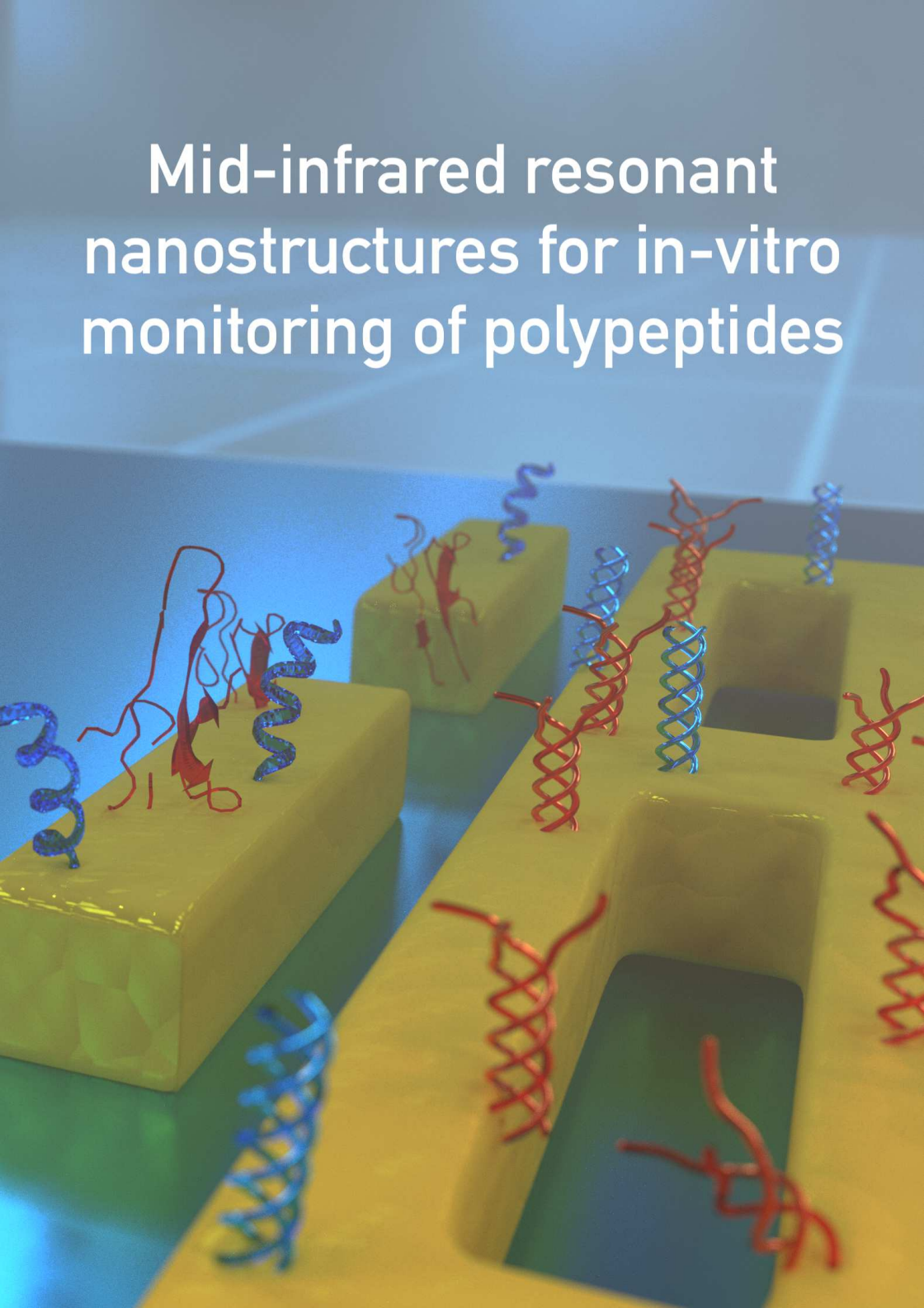

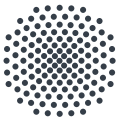

University of Stuttgart
Germany

Mid-infrared resonant nanostructures for in-vitro monitoring of polypeptides

Von der Fakultät Mathematik und Physik der Universität Stuttgart
zur Erlangung der Würde eines Doktors der
Naturwissenschaften (Dr. rer. nat.) genehmigte Abhandlung

vorgelegt von

Rostyslav Volodymyrovych Semenyshyn

aus Vyhoda, Ukraine

Hauptberichter: Prof. Dr. Harald Giessen
Mitberichterin: Prof. Dr. Stefanie Barz
Vorsitzender: Prof. Dr. Christian Holm

Tag der mündlichen Prüfung: 11.11.2019

4. Physikalisches Institut der Universität Stuttgart

Oktober 2019

Declaration

I hereby certify that this dissertation is entirely my own work except where otherwise indicated. Passages and ideas from other sources have been clearly indicated.

Stuttgart, September 2019
Rostyslav Semenyshyn

Abstract

Infrared vibrational spectroscopy is a technique based on the molecular vibrations, that is, the oscillation of individual atoms with respect to each other. Each of these vibrations has a characteristic resonance frequency which leads to the distinct vibrational fingerprint of a molecule and thus enables a label-free, non-destructive, and chemically specific detection of molecular species.

The infrared absorption cross-sections, which characterize the optical interaction strength, are relatively small. This is of minor importance for conventional spectroscopy, where large ensembles of molecules can be measured and thus contribute to the overall signal. However, the small infrared absorption hampers detection of molecules at low concentrations, which is of large importance for medical diagnostics, for instance, where the determination of the secondary structures of proteins is crucial due to their role in many incurable diseases. A key to overcome this limitation is to utilize plasmonic nanostructures, which confine the electromagnetic radiation on the nanometer scale and allow higher overall absorption.

In this dissertation, it is demonstrated that even a monolayer of proteins can be detected using mid-infrared resonant gold nanostructures. We use polypeptides as a model system and were able to investigate the secondary structure of molecular monolayers in-vitro. Applying different external stimuli, we are able to induce structural changes of polypeptides in aqueous environments. In addition to a mid-infrared resonant nanoantenna, nanoslits (or inverse antennas) can also enhance the optical response of polypeptides, which allowed us to detect the secondary structure of minicollagen monolayers. Both nanostructure designs provided the possibility even to monitor reversible conformational transitions of molecular monolayers.

Scaling this approach down to a single nanostructure allows to detect only a few thousands of polypeptides in liquid environments. The demonstrated concept could lead to integrated chip-level technology for biological and even medical applications, where biosamples with minute concentrations are investigated. With further advances, it could be possible to scale the process to a few or single proteins and observe the structural changes of individual entities.

Zusammenfassung

Infrarot-Vibrationsspektroskopie ist ein optisches Messverfahren, das auf Molekülschwingungen beruht. Dabei untersucht man die Schwingungen einzelner Atome im Molekül relativ zueinander. Jede dieser Schwingungen hat eine cha-rakteristische Resonanzfrequenz, welche dem Molekül einen individuellen Fingerabdruck verleiht und somit einen markierungs- und zerstörungsfreien, sowie chemisch spezifischen Nachweis molekularer Spezies ermöglicht.

Die Stärke der optischen Wechselwirkung wird durch den jeweiligen Absorptionsquerschnitt bestimmt, der im infraroten Spektralbereich ziemlich klein ist. Für konventionelle Spektroskopie Methoden ist dies von geringerer Bedeutung, da hier eine große Anzahl Moleküle betrachtet wird, die zum Gesamtsignal beiträgt. Die geringe Absorption im Infraroten erschwert jedoch den Nachweis von kleinen Molekülkonzentrationen, was aber von großer Bedeutung in der medizinischen Diagnostik ist. Zum Beispiel ist hier die Erkennung der Sekundärstruktur eines Proteins entscheidend, da diese eine bedeutende Rolle bei vielen unheilbaren Erkrankungen spielt. Ein Schlüssel dies zu umgehen, ist die Adsorption dieser Proteine an plasmonische Nanostrukturen. Diese konzentrieren elektromagnetische Strahlung in ein Volumen auf der Nanometer Skala, was zu einer größeren Gesamtabsorption führt.

In dieser Arbeit wird gezeigt, dass mit Hilfe von Goldnanostrukturen, die im mittleren Infrarotbereich resonant sind, sogar eine Proteinmonolage nachgewiesen werden kann. Dazu verwenden wir Polypeptide als Modellsystem, was eine in-vitro Untersuchung der Sekundärstruktur der molekularen Monolage ermöglicht. Durch Änderung der äußeren Umgebung können strukturelle Änderungen der Polypeptide in wässriger Umgebung hervorgerufen werden. Neben Nanoantennen, die im mittleren In-

frarotbereich resonant sind, können auch Nanoschlitze (bzw. inverse Antennen) die optische Antwort von Polypeptiden verstärken, was den Nachweis der Sekundärstruktur von Minikollagenmonolagen ermöglicht. Zusätzlich ermöglichen diese beiden Nanostruktur-Varianten die umkehrbare Konformationsänderung der molekularen Monolage zu beobachten.

Skaliert man diesen Ansatz nun herunter auf eine einzelne Nanostruktur, so erhält man ein System, mit dem man nur wenige Tausend Polypeptide in Wasser basierten Lösungen nachweisen kann. Dieses Konzept soll eine integrierte Technologie auf Chip-Ebene für biologische und medizinische Anwendungen ermöglichen, wo organische Proben kleinster Konzentrationen untersucht werden müssen. Ein nächster Schritt wäre, den Prozess noch weiter bis auf einige wenige oder einzelne Proteine zu reduzieren, um somit strukturelle Änderungen einzelner Bausteine beobachten zu können.

Publications

Parts of this work have already been published in scientific journals:

1. R. Semenyshyn, F. Mörz, M. Ubl, M. Hentschel, F. Neubrech, and H. Giessen,
   "Pushing down the limit : In-vitro detection of a polypeptide monolayer on a single infrared resonant nanoantenna",
   ACS Photonics, submitted (2019).

2. R. Semenyshyn, M. Hentschel, C. Huck, J. Vogt, F. Weiher, H. Giessen, and F. Neubrech,
   "Resonant plasmonic nanoslits enable in-vitro observation of single monolayer collagen-peptide dynamics",
   ACS Sensors 4, 1966 (2019).

3. R. Semenyshyn, M. Hentschel, C. Stanglmair, T. Teutsch, C. Tarin, C. Pacholski, H. Giessen, and F. Neubrech,
   "In-vitro monitoring conformational changes of polypeptide monolayers using infrared plasmonic nanoantennas",
   Nano Letters 19, 1 (2018).

Parts of this thesis have also been presented at international conferences:

1. R. Semenyshyn, M. Hentschel, C. Stanglmair, T. Teutsch, C. Tarin, C. Pacholski, H. Giessen, and F. Neubrech,
   "In-vitro monitoring secondary structure of polypeptides using mid-IR resonant nanoantennas",
   Nanometa Conference, Seefeld, Austria (2019).

2. R. Semenyshyn, M. Hentschel, C. Stanglmair, T. Teutsch, C. Tarin, C. Pacholski, H. Giessen, and F. Neubrech,
   "Principal component analysis for SEIRA-based monitoring of structural changes in polypeptides",
   Spring Meeting of the German Physical Society, Berlin, Germany (2018).

3. R. Semenyshyn, M. Hentschel, J. Vogt, C. Huck, C. Stanglmair, C. Pacholski, F. Neubrech, and H. Giessen,
   "Monitoring structural changes of polypeptides using resonant surface enhanced infrared spectroscopy",
   Spring Meeting of the German Physical Society, Dresden, Germany (2017).

4. R. Semenyshyn, F. Neubrech, M. Hentschel, X. Yin, J. Vogt, C. Huck, F. Weiher, C. Stanglmair, C. Pacholski, and H. Giessen,
   "Surface-enhanced infrared spectroscopy for poly-peptide sensing on single nanostructures",
   Spring Meeting of the German Physical Society, Regensburg, Germany (2016).

5. R. Semenyshyn, F. Neubrech, X. Yin, F. Weiher, C. Stanglmair, C. Pacholski, and H. Giessen,
   "Poly-peptide sensing with nanoantenna-assisted surface-enhanced infrared spectroscopy",
   Spring Meeting of the German Physical Society, Berlin, Germany (2015).

Further publications and contributions which are not covered in this dissertation:

1. L. Kühner, R. Semenyshyn, M. Hentschel, F. Neubrech, C. Tarin, and H. Giessen,
   "Vibrational sensing using infrared nanoantennas: towards the non-invasive quantitation of physiological levels of glucose and fructose",
   ACS Sensors, 4, 1973 (2019).

2. C. Huck, M. Tzschoppe, R. Semenyshyn, F. Neubrech, and A. Pucci,
   "SEIRA Based Chemical Identification of Single Ultrafine Particles",
   Phys. Rev. Appl. 11, 014036 (2019).

3. F. Mörz, R. Semenyshyn, T. Steinle, F. Neubrech, U. Zschieschang, A. Steinmann, and H. Giessen,
   "Nearly diffraction limited FTIR mapping using an ultrastable broadband femtosecond laser tunable from 1.33 to 8 μm",
   Opt. Express 25, 32355 (2017).

Contents

1 Introduction

Many different techniques were established to allow the investigation of various molecular properties. Detection of protein conformational changes is of high importance in health and disease for understanding the structural determinants of protein function. The secondary structure of proteins might be revealed by circular dichroism (CD) spectroscopy [1–3], X-ray crystallography [4, 5], nuclear magnetic resonance (NMR) spectroscopy [6–8], and atomic force microscopy (AFM) [9, 10]. Nevertheless, the techniques mentioned above have drawbacks, unfortunately. A large amount of analyte is required for CD, NMR, and X-ray crystallography for conformational studies. AFM, which can handle smaller amounts, is, however, difficult to utilize for in-vitro measurements. Therefore, infrared (IR) vibrational spectroscopy is a very promising technique for the identification of molecules and, in the case of proteins, determining the structural conformation [11–13]. The molecular bonds result in a unique spectrum due to vibrational excitations at characteristic frequencies, which cause a so-called vibrational fingerprint. Thus, an unambiguous, nondestructive, and label-free detection of substances is possible, making infrared spectroscopy a powerful and indispensable tool. Particularly, Fourier-transform infrared (FTIR) spectroscopy is widely used in various fields of research, in industry, and other applications for fast and routine structural investigations of chemical compounds, monitoring of processes, and identification of substances. Furthermore, as the optical response gets modified if a particular molecular structure changes due to external factors [14–19], IR spectroscopy is applicable to monitor the structural changes of proteins during physiological processes, which is of high importance for biological and medical applications.

On the other hand, similarly to the techniques mentioned above, conventional IR spectroscopy requires large amounts of molecules to allow reliable detection. Resonant plasmonic nanoparticles can overcome this limitation and enable vibrational spectroscopy of molecular species at low concentrations. The so-called surface-enhanced infrared absorption (SEIRA) spectroscopy utilizes the strong near fields of the metallic nanostructures, which enhances the infrared vibrational modes of the molecules [20–22]. Furthermore, it is possible to reach much higher sensitivity with a resonant SEIRA, where the resonance frequency of the plasmonic mode matches the molecular vibration [22, 23], and thus detection of the molecules with attomolar concentration is achievable [20, 24].

In recent years, many pioneering approaches have been developed, which revealed detailed information about the near field distribution around the nanostructures and about interactions with vibrational resonances of the molecules [25–28]. Adapting this technique, it became possible to detect biomolecules on top of the plasmonic chip [29–32]. These experiments demonstrated the ability of SEIRA in the detection of biomolecules, which are complex species and thus reveal rich vibrational spectra. Additionaly, peptides and proteins are able to change their structure in an aqueous environment, which led to follow-up studies in liquid surroundings [33–39]. Thus, it turned out that SEIRA allows not only detection of proteins being immersed in liquid but also monitoring molecular structural changes under the external stimulus. In this dissertation, we demonstrate various ways, which further develop the application of SEIRA for detection of biomolecules and for monitoring their structural changes.

As a theoretical primer, chapter 2 presents some of the fundamental scientific concepts necessary to discuss the interaction of electromagnetic waves with metallic nanoparticles, which confines the electromagnetic radiation on the nanometer scale and enhances molecular optical response in the vicinity of the nanoparticle. Additionally, we show the analytical model, which describes the coupling between the nanoparticle and the molecule.

Also, we discuss the Babinet's principle, which brings the understanding to the design of inverse nanoantennas for SEIRA.

Chapter 3 briefly summarizes the methods necessary for the realization of the in-vitro protein studies at monolayer scale. A number of points are crucial here: the optimal design of nanostructures, adsorption of the molecules, measurement setup and geometry, as well as data analysis. All these aspects allow for ultrasensitive experiments discussed in the next chapters.

Thus, in chapter 4, we start with a combination of resonant mid-IR inverse nanoantennas (i.e., nanoslits) and a macromolecular model system, namely collagen-peptides. These molecules can, upon a trigger such as a temperature change or adding the chemical stimulus, reversibly change their confirmation. We demonstrate that infrared measurements of only a molecular monolayer of collagen-peptides in a resonant nanoslit sensor can reveal structural folding and unfolding of these macromolecules in-vitro.

In chapter 5, we realize a crucial step in sensing of large biomolecules by demonstrating in-vitro observation of folding and unfolding processes of the model system poly-L-lysine on a chip-scale sensor. Utilizing resonant plasmonic nanoantennas for surface-enhanced infrared spectroscopy, we monitored in-vitro the conformational change between α-helix and β-sheet states of poly-L-lysine, induced by controlled external chemical stimuli.

We push the limits of nanoantenna-based detection of polypeptides in chapter 6. Namely, we demonstrate a combination of a highly brilliant, pulsed laser source and an individual plasmonic nanoantenna as an ultra-sensitive platform for table-top protein studies at attomolar concentrations and attoliter volumes.

Finally, chapter 7 summarizes the main results of all studies discussed and provides a short outlook on how future optical nanosensors could be realized in order to reach the ultimate goal of monitoring the dynamics of a few or even a single protein.

2

Fundamentals

This chapter is an introduction to the surface plasmon theory and utilization of nanostructures for sensing applications. Therefore, the optical properties of materials are discussed, aiming for an intuitive understanding of the plasmon nature using simple oscillator models. As this dissertation is focused on nanostructures as a sensing platform, the chapter continues with the discussion of localized surface plasmons and nanoantenna resonances. Thus, we introduce individual, array, and inverse antennas which we utilize for molecular detection in the next chapters. The chapter ends with a brief introduction to the surface-enhanced sensing approach, where we discuss antenna near-fields and coupling to molecular vibrations leading to improved sensitivity.

2.1 Optical properties of the materials

To explain the working principle of the optical sensors presented in this dissertation, we should discuss the interaction of light with materials. Therefore, we start with a simple model and derive equations, which describe the optical properties of materials [40, 41].

2.1.1 *Lorentz oscillator equation*

One can assume that the nucleus of an atom is much more massive than an electron. Having this in mind, one could build a model where the electron-spring system is connected to an infinite mass (fig. 2.1), which is the nucleus and does not move [42]. Depending on the case, the electron mass may be substituted by the reduced or effective electron mass to account for deviations

from the assumption introduced above, but first we take the default value of $m_e = 9.11 \times 10^{-31}\, kg$.

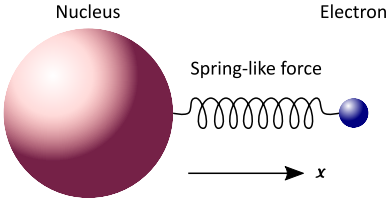

Figure 2.1: Schematic drawing of the Lorentz Oscillator

Furthermore, the assumption that the binding force behaves as a spring works well for any kind of binding if the displacement is small, meaning that only the constant and linear terms in the Taylor expansion are relevant. Also, one should take into account the damping term, which stands for internal collisions in the solid and radiation emitted by the electron.

Finally, to complete the Lorentz oscillator equation, the driving force needs to be determined. In the case of a solid placed in an electric field E varying in time with angular frequency ω, but independent of the displacement in the x direction, it looks as follows:

$$\vec{F}_{driving} = -q\vec{E} \tag{2.1}$$

where q is the absolute value of the charge of the electron ($q = 1.602 \times 10^{-19}\, C$).

As the system, which we consider here, has charges displaced one from another, we can consider it as a dipole. Thus, with an oscillation of the spring, displacement of charges will oscillate as well, leading to the change in polarization, which is:

$$\vec{P} = -qN\vec{x} \tag{2.2}$$

The polarization vector is the density (per volume) of dipole moments, which are defined as the product of the charge and the displacement vector. N stands for amount of the elementary changes.

Here, the polarization vector changes due to the driving force. Therefore we may start with a general harmonic oscillator:

$$m\frac{d^2\vec{x}}{dt^2} + m\gamma\frac{d\vec{x}}{dt} + m\omega_0^2 x = \vec{F}_{driving} \tag{2.3}$$

to which, from the above, we take $\tilde{x}(t) = \frac{-\tilde{P}(t)}{Nq}$ and $\vec{F}_{driving}$ from 2.1 which leads to:

$$-\frac{m}{Nq}\frac{d^2\vec{P}}{dt^2} - \frac{m\gamma}{Nq}\frac{d\vec{P}}{dt} - \frac{m\omega_0^2}{Nq}\vec{P} = \vec{F}_{driving}$$

$$\frac{d^2\vec{P}}{dt^2} + \gamma\frac{d\vec{P}}{dt} + \omega_0^2\vec{P} = -\frac{Nq}{m}\vec{F}_{driving}$$

$$\frac{d^2\vec{P}}{dt^2} + \gamma\frac{d\vec{P}}{dt} + \omega_0^2\vec{P} = \frac{Nq^2}{m}\vec{E} \tag{2.4}$$

The equation 2.4 is the so-called Lorentz oscillator equation for the polarization. Here, ω_0 is the resonant frequency, m is the mass of the electron, and γ is a damping due to the environment.

2.1.2 *The plasma frequency*

Next we introduce and discuss an important parameter, the so-called plasma frequency, which is the natural resonant frequency of a plasma oscillation. Simply stated, a plasma is an ionized, electrically conducting gas of charged particles, usually occurring under conditions of very high temperature and/or very low particle density. One of the most fundamental collective effects of a plasma is the oscillation of the changed particles. Instead of dealing with the individual motion of each electron and each nuclei, one can consider the center of mass of the nuclei and the center of mass of the electrons. In equilibrium, they coincide. When they shift with respect to each other, a Coulomb force arises trying to restore their position, which initiates an oscillatory behavior. The frequency at which these oscillations resonate is called the *plasma frequency* [43]:

$$\omega_p^2 = \frac{Nq^2}{m\epsilon_0}$$

which is equivalently:

$$\omega_p = \sqrt{\frac{Nq^2}{m\epsilon_0}} \tag{2.5}$$

where m is the mass of charged particle, N is the density of particles, q is the charge of particle, and ϵ_0 is the vacuum permittivity which is a constant and equals $8.854 \times 10^{-12}\, F\, m^{-1}$.

As we can see, the plasma frequency is proportional to the electron density and thus can be calculated for any material for which this density is known. The plasma frequency for, so-called, non-plasma materials stands for the natural collective oscillation frequency of the electrons in the bulk material, not of individual dipoles.

Interestingly, electromagnetic waves can only penetrate the material if their frequency is larger than ω_p, otherwise they are reflected [43].

2.1.3 *Permittivity*

At this point we can simplify equation 2.4 by substituting the definition of plasma frequency eq. 2.5 and continue with the solution of it. Here, one should mention that in general case the electric field is time dependent.

$$\frac{d^2\vec{P}(\omega,t)}{dt^2} + \gamma\frac{d\vec{P}(\omega,t)}{dt} + \omega_0^2\vec{P}(\omega,t) = \epsilon_0\omega_p^2\vec{E}(\omega,t) \tag{2.6}$$

As the direction of both polarization and electric field vectors is the same, we can omit the vector sign for simplicity. Next, as we assume a sinusoidally-varying electric field and polarization:

$$P(\omega,t) = P(\omega)cos(\omega t) = \mathfrak{Re}\left\{\tilde{P}(\omega)e^{j\omega t}\right\} \tag{2.7}$$

where the $\tilde{P}(\omega)$ is independent of time and is a complex quantity in order to account for any phase-lag between the driving electric field and the polarization.

Similar to the polarization, we substitute the electric field in the harmonic form and obtain:

$$\frac{d^2\left[\tilde{P}(\omega)e^{j\omega t}\right]}{dt^2}+\gamma\frac{d\left[\tilde{P}(\omega)e^{j\omega t}\right]}{dt}+\omega_0^2\tilde{P}(\omega)e^{j\omega t}=\epsilon_0\omega_p^2Ee^{j\omega t}$$

taking into account that $\tilde{P}(\omega)$ is independent of time, we continue with derivatives:

$$(j\omega)^2\,\tilde{P}(\omega)e^{j\omega t}+j\gamma\omega\tilde{P}(\omega)e^{j\omega t}+\omega_0^2\tilde{P}(\omega)e^{j\omega t}=\epsilon_0\omega_p^2Ee^{j\omega t}$$

Thus, for the complex polarization in the vector form we obtain:

$$\vec{\tilde{P}}(\omega)=\frac{\epsilon_0\omega_p^2}{(\omega_0^2-\omega_p^2)+j\gamma\omega}\vec{E} \tag{2.8}$$

From another side, the polarization of a material is related to the applied electric field and the electric susceptibility of the material:

$$\vec{P}=\epsilon_0\chi_e\vec{E}$$

which may be easily modified into the complex form:

$$\vec{\tilde{P}}=\epsilon_0\tilde{\chi_e}\vec{E}$$

If we now recall the concept of relative permittivity, also called the dielectric constant $\frac{\epsilon}{\epsilon_0}=1+\chi_e$, we obtain:

$$\vec{\tilde{P}}=\epsilon_0\left(\frac{\tilde{\epsilon}}{\epsilon_0}-1\right)\vec{E} \tag{2.9}$$

Combining this with our previous result, eq. 2.8, we get:

$$\frac{\tilde{\epsilon}}{\epsilon_0}=1+\frac{\omega_p^2}{(\omega_0^2-\omega^2)+j\gamma\omega} \tag{2.10}$$

The above equation shows that the permittivity depends on the frequency of the electric field, besides the plasma frequency and damping (which are properties of the medium). A medium displaying such behavior is called *dispersive*.

Since our electric permittivity is a complex quantity, we can break it down into a real and an imaginary part:

$$\frac{\tilde{\epsilon}}{\epsilon_0} = \epsilon_r - j\epsilon_i \tag{2.11}$$

From this definition, and remembering that these quantities are the functions of frequency of the driving electric field (eq. 2.10), we can obtain the magnitude and phase of the polarization with respect to the electric field, which is the amplitude and phase of the displacement of the oscillator. Thus, after removing the imaginary number from the denominator in equation 2.10:

$$\epsilon_r(\omega) - 1 = \frac{\omega_p^2\left(\omega_0^2 - \omega^2\right)}{\left(\omega_0^2 - \omega^2\right)^2 + \omega^2\gamma^2} \tag{2.12}$$

$$\epsilon_i(\omega) = \frac{\omega_p^2\gamma\omega}{\left(\omega_0^2 - \omega^2\right)^2 + \omega^2\gamma^2} \tag{2.13}$$

The real and imaginary parts are plotted in fig. 2.2:

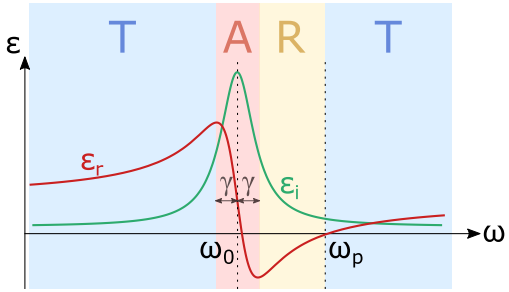

Figure 2.2: Real and imaginary parts of electric permittivity of dielectric material. Here, one can see three type of optical ranges, where the material can be mostly **T**ransparent, **Absorptive**, and **Reflective**

2.1.4 *Frequency analysis*

From fig. 2.2, we can see that there is a peak in ϵ_i around $\omega = \omega_0$, which is the resonance frequency of the material. This corresponds to the strong absorption of the electromagnetic radiation

by the material near that frequency. Such a frequency-dependent optical behavior of a material often is divided into regions of: **T**ransmission, **A**bsorption, and **R**eflection.

The absorption is largest around the resonant frequency, as was mentioned, and is about 2γ wide (marked with red). Before this region and after $\omega = \omega_p$ the material is mostly transparent (marked with blue). In the yellow region, the incident light is reflected mostly.

We can also try to get a more intuitive understanding of this frequency dependence. Thus, please note that the polarization vector and the electric field are related by the electric susceptibility, which is equal to $\tilde{\chi}_e = (\frac{\tilde{\epsilon}}{\epsilon_0} - 1) = (\epsilon_r - 1) - j\epsilon_i$ and therefore:

$$\vec{\tilde{P}}(\omega) = \epsilon_0 \tilde{\chi}_e \vec{E}$$

$$\tilde{\chi}_e(\omega) = |\chi_e(\omega)| \, e^{j\phi_{\chi_e}(\omega)}$$

Thus, the magnitude is given by:

$$|\chi_e(\omega)| = \sqrt{(\epsilon_r - 1)^2 + \epsilon_i^2} \tag{2.14}$$

As we assumed $\vec{E}$ being real, the phase difference between the polarization vector and the electric field will be equal to the phase of the complex susceptibility, which is given by:

$$\phi_P = \phi_{\chi_e}(\omega) = \arctan(\frac{\epsilon_i}{\epsilon_r - 1}) = \arctan(\frac{\omega\gamma}{\omega_0^2 - \omega^2}) \tag{2.15}$$

Let us have a look at extreme cases.

Low frequencies, $\omega \approx 0$**:**

$\epsilon_i(0) \approx 0$

$|\chi_e(0)| \approx |\epsilon_r - 1| \approx \frac{\omega_p^2}{\omega_0^2}$

$\phi_{\chi_e}(0) \approx \arctan(0) = 0$

Thus, the amplitude of the displacement is somewhere in between the peak and zero, whereas the displacement is in phase with the varying electric field.

Near the resonant frequency, $\omega \approx \omega_0$**:**

$$\epsilon_r(\omega_0) - 1 \approx 0$$
$$|\chi_e(\omega_0)| \approx |\epsilon_i| \approx \frac{\omega_p^2}{\gamma\omega_0}$$
$$\phi_{\chi_e}(\omega_0) \approx \arctan(\frac{\gamma\omega_0}{0}) \approx \arctan(\infty) = \frac{\pi}{2}$$

This demonstrates that the amplitude is much larger than the low frequency scenario (as we assume $\gamma \ll \omega_0$) and the displacement is 90°.

High frequencies, $\omega \to \infty$**:**

$$|\chi_e(\infty)| \approx 0$$
$$\phi_{\chi_e}(\infty) \approx \arctan(0) = 0 \text{ or } \pi$$

As ω shows up to the fourth power in the denominator of both ϵ_r and ϵ_i, which forces them to vanish. To figure out the phase, we refer to the eq. 2.15, where the denominator is $-\omega^2$, so the whole expression becomes a small negative number. Hence, the displacement is minimal and it is 180° out of phase with the electric field.

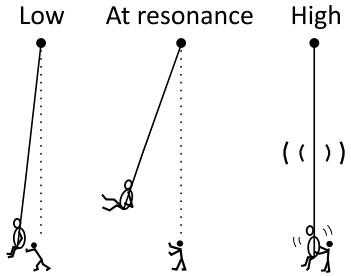

Figure 2.3: Drawing of an anology of each frequency regime

From intuitive side, an analogy can be made with pushing someone on a swing at each frequency regime (fig. 2.3).

To summarize, depending on the frequency, the dielectric material is:

- **T**ransmissive for $0 < \omega < \omega_0 - \gamma$
- **A**bsorptive for $\omega_0 - \gamma < \omega < \omega_0 + \gamma$

- **R**eflective for $\omega_0 + \gamma < \omega_p$
- **T**ransmissive for $\omega > \omega_p$

2.1.5 *Drude-Lorentz model*

The Drude model for electrical conduction is basically the extention of the Lorentz oscillaltor model, where the kinetic theory is applied to electrons in a solid. Metals have a good electrical conductivity as the electrons are not bound to the nuclei. The so-called delocalized electrons are known as free electrons and allow metals to conduct the electricity [44, 45].

Therefore, we can consider a particular change in our Lorentz oscillator model. Namely, if the electrons are not bound, then there is no restoring force of the "spring", $F_{spring} = 0$. That means that the equivalent spring constant associated with it is equal to 0, so $k = m\omega_0 = 0$ and thus $\omega_0 = 0$. However, the rest of terms remain, which gives us the solution of the Drude-Lorentz model:

$$\frac{\tilde{\epsilon}}{\epsilon_0} = 1 - \frac{\omega_p^2}{\omega^2 + j\gamma\omega} \tag{2.16}$$

$$\epsilon_r(\omega) = 1 - \frac{\omega_p^2}{\omega^2 + \gamma^2} \tag{2.17}$$

$$\epsilon_i(\omega) = \frac{\omega_p^2 \gamma}{\omega\left(\omega^2 + \gamma^2\right)} \tag{2.18}$$

Although more detailed models exist for metals, the Drude model is very useful to get reliable predictions regarding the optical behavior of metals.

As one can see from fig. 2.4, metals do not exhibit the first transmissive region. For the metals the absorption region starts directly at low frequencies up to $\omega = \gamma$, where γ usually is relatively small. Similarly to the dielectric materials, for $\gamma < \omega < \omega_p$ metals exhibit a reflective region and a transparent region for $\omega > \omega_p$. Thus, we can summarize these results, metals are:

- **A**bsorptive for $0 < \omega < \gamma$

- **R**eflective for $\gamma < \omega < \omega_p$
- **T**ransmissive for $\omega > \omega_p$

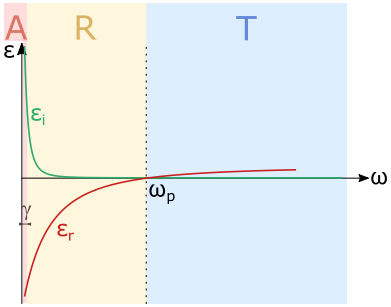

Figure 2.4: Real and imaginary parts of electric permittivity of metal

2.2 NANOANTENNA RESONANCE

2.2.1 *Plasmons in the bulk*

The Drude dielectric function, discussed in the previous section (eq. 2.17, eq. 2.18), vanishes at $\omega \approx \omega_p$, for $\gamma \approx 0$. This corresponds to an excitation of collective electron oscillations. This phenomenon is known as plasma oscillation and the excitation called plasmon [46].

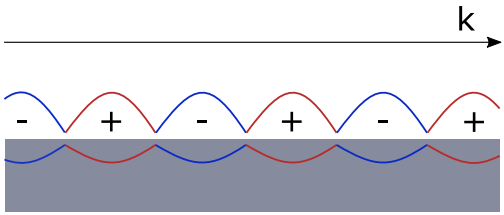

Figure 2.5: Surface plasmon polariton (SPP)

Plasmons, that travel along a metal–dielectric or metal–air interface, are named surface plasmon polariton (SPP), see fig. 2.5.

In fig. 2.5 the k-vector is a wavevector, which describes a propagation of the electromagnetic wave, its absolute value is given as:

$$k(\omega) = \frac{\omega}{c}\sqrt{\frac{\epsilon(\omega)}{\epsilon(\omega)+1}} \tag{2.19}$$

A surface plasmon polariton is the surface wave that involves both charge motion in the metal (surface plasmon, SP) and electromagnetic waves in the air or dielectric (polariton).

As one can see from eq. 2.19, depending on the frequency, light may cause different response at the metal-dielectric interface. As for metals, typically $\gamma \approx 0$, we can use eq. 2.16 for eq. 2.19 and obtain:

$$k(\omega) = \frac{\omega}{c}\sqrt{\frac{\omega^2 - \omega_p^2}{2\omega^2 - \omega_p^2}} \tag{2.20}$$

which is so-called dispersion relation of different types of plasmons (fig. 2.6). This dispersion relation allows us to investigate at which frequencies SPPs may be excited.

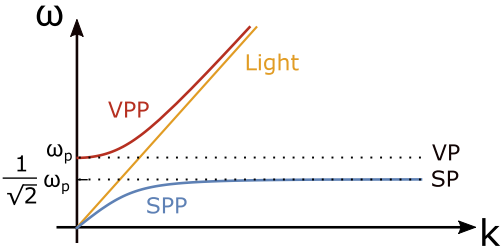

Figure 2.6: Dispersion curves of volume plasmons (red) and surface plasmons (blue). No plasmons can be excited in the frequency range indicated by the dashed lines

Thus, as depicted in fig. 2.6, for $\omega = \omega_p$ the wave vector vanishes, which means that wave propagates through the metal. This is so-called volume plasmon (VP), which is not possible to excite by light. However, for $\omega > \omega_p$ plasmon propagation inside the metal occurs known as volume plasmon-polariton (VPP).

Surface plasmons can be excited at the frequency $\omega = \frac{\omega_p}{\sqrt{2}}$, where the wave vector is approximated for large values. Below

this frequency the SPP is possible to excite. Thus, we can define the frequency of SP as:

$$\omega_{sp} = \frac{\omega_p}{\sqrt{2}} = \sqrt{\frac{1}{2}\frac{Nq^2}{m\epsilon_0}} \tag{2.21}$$

Between the SPs and VPs, a frequency band is located in which no plasmons can be excited.

Due to damping in the metal, SPs can only travel a limited distance along the surface. However, in particles with dimensions below wavelength (nanoparticles) the propagation distance is instead limited by the particle size. In this case, a localized surface plasmon polariton (LSPP) can directly be excited by light (fig. 2.7).

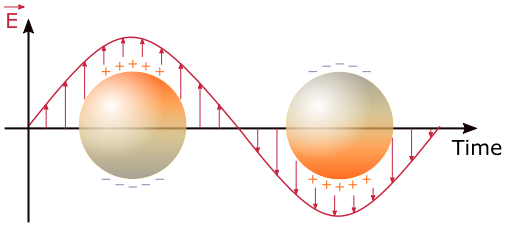

Figure 2.7: Localized surface plasmon polariton (LSPP)

Thus, to fulfill the conditions discussed above and achieve the oscillation of free electrons through all the surface length, the particle needs to be half wavelength long. If this is the case, for half of the period the wave drives the electrons towards one side of the particle and vice versa for the second half period (fig. 2.7).

2.2.2 *Nanoantenna*

Similarly to the nanoparticle shown in fig. 2.7, a classical radioantenna of smaller size can be produced, which will act as an antenna in the infrared or visible spectral range and thus the frequency LSPP can be tuned.

Assuming the nanoantenna to be a rod with length L, which is much greater than its radius R ($L \gg R$), light interacts with the

antenna and induces currents propagating directly at the surface. As the tip ends of the antenna constitute hard boundaries for these currents, one can conclude that resonances occur at [47]:

$$\lambda_{res} = \frac{2nL}{m}, \qquad \omega_{res} = \frac{\pi mc}{Ln} \tag{2.22}$$

where n is the refractive index of the surrounding medium (for air $n = 1$) and m is a positive integer giving the order of the excited mode. As illustrated in fig. 2.8, even modes consist of a symmetrical charge distribution and therefore exhibit no dipole moment. In the ideal case, they cannot be excited under normal illumination and are therefore referred to as "dark modes" [48, 49].

Figure 2.8: Charge density distribution for the first four modes in rod antennas

For real antennas however, dark modes are often visible. One reason for that are small defects in the antenna geometry, another reason comes from the fact that real antennas usually are not embedded in a homogeneous medium but are fabricated on a substrate which results in a break of symmetry [50].

As was mentioned above and from fig. 2.22, we can tune the resonance of an antenna by varing its length. Thus antenna lengths in the centimetre and millimetre range result in resonances in the micro- or radio-wave spectral range respectively, whereas micrometer and submicrometer sized antennas exhibit resonances in the spectral range of visible and infrared light. These antennas are called "nanoantennas".

In the visible spectral range, the Drude-Lorentz model does not fit the experimental observations due to the interband transitions. This means that the interaction with light depends here on the properties of the antenna material.

In this thesis, antennas of the length of a few micrometers were used to excite resonances with light in the MIR frequency range (fig. 2.9). Here, the transmittance of single nanoantennas is simulated with finite-difference time-domain (FDTD) method (for more details, see Methods). In this model, antennas are placed on top a CaF_2 substrate in an air environment. Important to mention that simulation assumes a $15 \times 15 \mu m^2$ area, which leads to a weaker modulation depth for shorter antennas and a better modulation for the longer ones due to a different extinction cross-section (for more details, see Simulations of the nanoantennas).

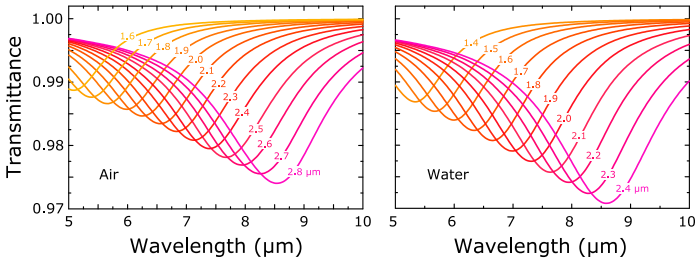

Figure 2.9: Simulated transmittance of antennas with different length in air as well as water surroundings on the CaF_2 substrate, and measurement area of $15 \times 15 \mu m^2$

As one can see, the spectral resonance position of an ideal nanoantenna only depends on the antenna geometry and the refractive index of the surrounding medium. Real nanoantennas however, exhibit a deviation from this ideal behaviour. One reason for this deviation is the finite conductivity of real metals in contrast to the assumption of a perfect conductor in the ideal antenna model. As a result, the electromagnetic field can penetrate the metal over a short distance, which is a so-called *skin depth* (δ_{skin}), causing the effective resistance of the conductor. For surface-plasmons the skin depth is given by [51]:

$$\delta_{skin} = \frac{1}{\sqrt{k^2 - \epsilon(\omega)\frac{\omega^2}{c^2}}} \tag{2.23}$$

or with eq. 2.19:

$$\delta_{skin} = \frac{c/\omega}{\sqrt{-\frac{\epsilon(\omega)^2}{\epsilon(\omega)+1}}} \tag{2.24}$$

We can simplify this expression if $|\epsilon_r| \gg 1$ and $|\epsilon_i| \to 0$, where ϵ_r is the real part of the dielectric function of the metal and ϵ_i an imaginary one. The skin depth then becomes:

$$\delta_{skin} = \frac{c/\omega}{\sqrt{-\epsilon_r(\omega)}} \tag{2.25}$$

For gold antenna in the MIR spectral region this penetration depth is approximately $\delta_{skin} \approx 22\,nm$. Unlike classical antenna theory, where macroscopic antennas are studied, these fields cannot be neglected as the skin depth is comparable to the dimension of typical nanoantenna sizes (both width and height $\sim$ 100 nm). As a result, the resonance position of a real antenna will also be influenced by the antenna aspect ratio [52].

2.2.3 *Nanoantenna array*

Application of individual nanoantennas is not so straightforward to do, due to the small absorption and scattering cross-sections of such a nanostructure. Therefore, for single nanoantenna measurements small areas should be probed by a light source with high brilliance (synchrotron, laser) [20, 53].

Due to this reason, experiments are usually performed on arrays consisting of many nanoantennas. As it was mentioned in the introduction, the experiments described within this thesis deal with both antenna arrays and single antennas. First, we start with biosensing based on antenna arrays as it is experimentally easier and thus is a necessary step for the validation of the concept before moving towards single nanoantenna applications.

However, there are interaction effects between antennas in periodically arranged arrays, which influence the spectral response of the system [30, 54].

A typical design of a nanoantenna array is depicted in fig. 2.10. In contrast to an individual structure, several parameters are to

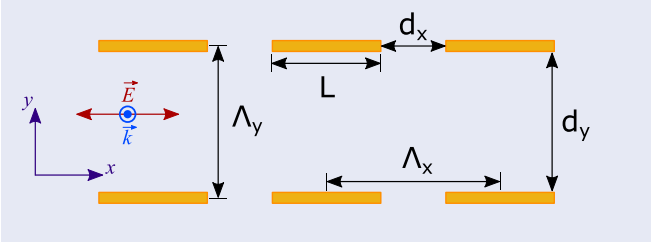

Figure 2.10: Design of a typical array of nanoantennas with length L. Indicated are the spacings d_x and d_y, as well as the grating constants Λ_x and Λ_y. Here, the x-axis is the parallel to the long antenna axis. Electric ($\vec{E}$) field vector perpendicular to the substrate with a polarization parallel to the long axis of the antennas.

be considered in this case. Namely, grating constants Λ_x and Λ_y as well as spacings d_x and d_y, where x-axis is towards the long antenna axis.

Due to the periodic arrangement, so-called Rayleigh-Wood anomalies occur [30, 54], which Wood has investigated observing the spectrum of a continuous light source utilizing an optical metallic diffraction grating [55]. According to Rayleigh's explanation of this phenomenon, an anomaly in a spectrum occurs at a wavelength corresponding to the passing-off spectrum of a higher order. This means that anomaly has the wavelength of a scattered wave, which propagates tangentially to the grating surface [56, 57]. Therefore, the angle of incidence at which anomalies are expected to occur are obtained from the equation:

$$\sin\theta_m = \sin\theta + m\frac{\lambda_i}{n_{subs}d} \tag{2.26}$$

where m is an order of mode and is an integer, λ_i is the wavelength of the light, d is the groove period, n_{subs} is the refractive index of the substrate on which the nanoantennas are produced, θ is the angle of incidence (measured anticlockwise from the normal to the grating), θ_m is the angle of diffraction (measured clockwise). The passing-off of the order m occurs when $\sin\theta_m = \pm 1$. Later, Fano achieved the first generic theoretical solution on Wood's anomalies [58].

For the nanoantenna array case, grating modes are damped due to the propagation along the substrate interface [30, 45]. This damping leads to a broadening of the far-field response and a drop of the plasmonic near-field intensity [59–62]. However, if one follows the design demonstrated in [30], one achieves a significant narrowing of the plasmonic far-field response and an increase of the near-field intensity. As authors have demonstrated, it is important to have evanescent instead of radiative grating modes and thus the antenna resonance does not suffer from damping.

2.2.4 *Babinet's Principle: Nanoslits*

So far, only metal rod nanoantennas are discussed. However, according to Babinet's principle, so-called inverse nano-structures, which consist of nanoapertures in a continuous metallic film, also have plasmonic resonances [25, 63–66].

If one compares the optical response of nanoslits with nanoantennas, one realizes that several quantities exchange their respective roles in the inverse system. Namely, reflectance and transmittance or perpendicular and parallel polarization of the incident light are swapped, which is a direct consequence of Babinet's principle and leads thus to a similar spectral response [67].

Therefore, a design of the sample with inverse nanostructures is similar to the one shown in fig. 2.10, but with a few important differences. Fig. 2.11 depicts a typical design of nanoslit arrays, which is inverse to the nanoantenna array discussed above in section 2.2.3.

As it is shown in fig. 2.11, the incident light needs to be perpendicularly polarized to the long axis of the slits in order to excite the plasmonic modes. To probe the optical response of such an inverse sample, measurements in reflection geometry need to be performed. Thus, utilization of the nanoslits requires the investigation of reflectance instead of transmittance, which is the case for nanoantennas [67]. Nanoslits also feature the grating modes,

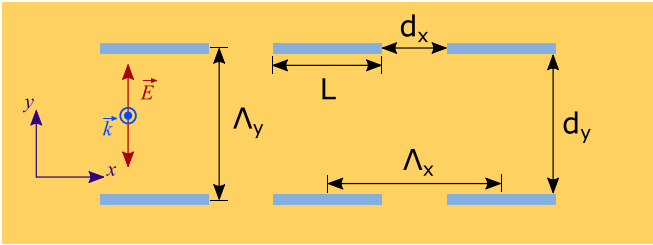

Figure 2.11: Design of a typical array of nanoslits with length L etched in the gold mirror. Similarly to the nanoantenna array, important parameters are: the spacings d_x and d_y, the grating constants Λ_x and Λ_y. Here, the x-axis is the parallel to the long antenna axis. Electric ($\vec{E}$) field vector perpendicular to the substrate with a polarization perpendicular to the long axis of the slits.

discussed in section 2.2.3, similarly to the nanoantennas with the same mathematical formalism.

2.3 SURFACE-ENHANCED MOLECULAR SENSING

2.3.1 *Nanoantenna's near-field*

Both reflectance and transmittance are the characteristics of the so-called far-field. However, a resonant nanoantenna features also a strong near-field due to the electrons oscillating in the metal (fig. 2.8). The near-field is the evanescent fluid in the vicinity of the antenna [68–72].

The boundary between the near- and far- fields is only vaguely defined, and it depends on the dominant wavelength emitted by the antenna and size of the antenna. As we consider the nanoantenna in the resonant regime, the near field of it is schematically shown in fig. 2.12. In this case, the near-field region is on the order of about the resonance wavelength.

For the electromagnetically long antennas, which are longer than half of the wavelength of the radiation they emit, in the first

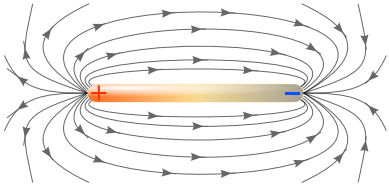

Figure 2.12: Illustration of the electric field surrounding the antenna in resonant regime, where a positive (red) and a negative (blue) charges are at the antenna ends.

order approximation the near-field region is defined in terms of the Fraunhofer distance [73]:

$$d_f = 2\frac{L^2}{\lambda} \tag{2.27}$$

where L is a length of an antenna and λ is a wavelength of emitted wave.

The near-field region features the strongest electromagnetic energy very close to the antenna surface up to $\frac{\lambda}{2\pi}$, which is the so-called reactive region. Here, the electric and magnetic fields are not necessarily in phase with each other and the angular field distribution is highly dependent upon the distance and direction from the antenna. Therefore, only numerical methods (see Methods) can determine the structure of the field, as not all this field radiates.

In this thesis, we explore a strong near-field of an antenna in order to enhance the optical response of the molecules and thus achieve a higher sensitivity. This means that molecules should be located in the vicinity of the nanoantenna, which is resonant at the frequency close to the vibration of molecule.

2.3.2 *Molecular vibrations*

Molecular vibration can be considered to be like the motion of particles connected by springs. As a molecule consists of atoms, which are connected by chemical bonds with no fixed length (the

distance between atoms), the molecular vibration is the oscillation of the particle due to spring-like bonding [74]. The frequency of the periodic motion is known as a vibration frequency. Typical frequencies of molecular vibrations are in the infrared range approximately from 300 cm^{-1} to 4000 cm^{-1}, which is the so-called fingerprint region.

In first order approximation, we assume that the motion in a normal vibration can be described as a kind of simple harmonic oscillator is correct. This provides an intuitive explanation of the fundamental frequency, whereas discussion of the overtones, for example, would require the introduction of the anharmonic oscillator model.

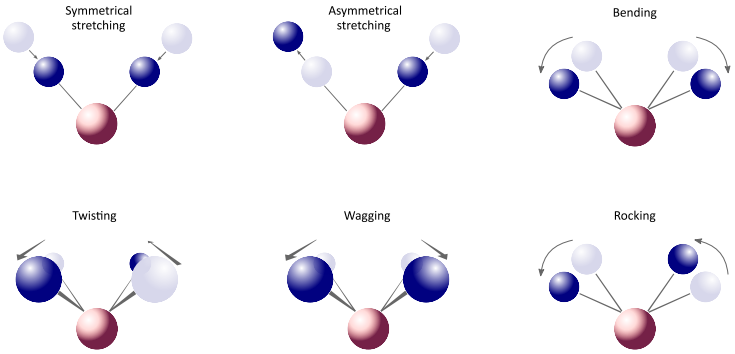

Figure 2.13: Sketches of the most common vibrations. Note that wagging and twisting are out of the plane, whereas the rest of the motions are in the plane.

There are several common types of vibration (fig. 2.13), which one may divide into two groups: in plane and out of plane. The most common vibrations, which are usually found in organic compounds, are:

- *stretching*, a change in the length of a bond which may be symmetrical and asymmetrical
- *bending*, a change in the angle between two bonds
- *rocking*, a change in angle between a group of atoms

- *wagging*, a change in angle between the plane of a group of atoms
- *twisting*, a change in the angle between the planes of two groups of atoms

Infrared (IR) spectroscopy exploits vibrational modes by probing the molecules with light. The infrared molecular spectrum is recorded by passing a beam through the sample. When the frequency of the IR is the same as the vibrational frequency, absorption occurs. Examination of the transmitted light reveals how much energy was absorbed at each frequency and thus allows to recognize the material investigated.

2.3.3 *Protein folding*

Proteins are complex molecules built from a set of amino acids (fig. 2.14). Amino acids typically consist of a carbon atom linked to the so-called amino group and carboxyl group, from one side, and a variable component called a side chain (fig. 2.14 **a**). Multiple amino acids are linked together by peptide bonds, which forms a long chain. This linear sequence of amino acids of the protein is considered the primary structure of the molecule [75–77].

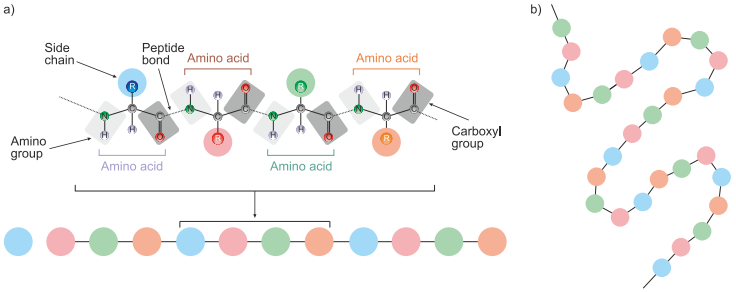

Figure 2.14: Schematic drawing of the protein structure. (**a**) Different chemical groups are linked together and thus form a the primary structure of the protein. (**b**) The amino acids chain folds to a particular energetically favorable form, which is the secondary structure.

The primary structure of a protein drives the folding and intramolecular binding of the linear amino acid chain, which consequently determines the protein's unique three-dimensional shape (fig. 2.14 **b**). Thus, the protein chain sometimes causes certain patterns of folding, which is the secondary structure of the protein. The final shape is typically the most energetically favorable one, which means that surrounding of the molecule strongly influences the final molecular form [76, 78, 79].

Despite the fact that proteins, as well as polypeptides, are considered macromolecules, they are still too small to observe directly [80]. Therefore, one must utilize indirect methods to investigate these molecules [81]. As the vibrations are also influenced by their respective surrounding, including peptide-bond angles and hydrogen-bonding patterns, these frequencies are also subject to changes during conformational transitions [14, 16]. Thus, a molecule in its different conformational states has distinct vibrational spectra despite an identical chemical formula. This also allows monitoring of the conformational changes of molecules during physiological processes [10–12, 19, 82–85]. This information is complementary to the mapped conformation as the transition from one state to another provides important information about the reaction pathways. This transition pathway, i.e., the exact intermediate states during folding and unfolding of the molecules, can offer insight into the working principle of the underlying processes.

2.3.4 *Fano-resonances*

Since molecular vibration and plasmon resonance may be assumed as harmonic oscillators, these oscillators may be coupled, if the molecule is located in the near-field of the nanoantenna. Therefore, modified functional forms of coupled harmonic oscillators [36] or Fano-resonances [86–89] are used to derive an intuitive understanding of the interaction between antenna and molecule [90, 91].

Fano-resonances turned out to be convenient for the fitting of the experimental data because it allows for extracting the individual properties of the molecular and the plasmonic excitation.

In contrast to Lorentzian-type symmetric line shapes, Fano-resonances feature an asymmetric profile (Fano-profile) [92]:

$$F(\omega) = \frac{(\sigma(\omega) + q)}{\sigma(\omega)^2 + 1}, \qquad \sigma(\omega) = \frac{\omega - \omega_0}{\gamma} \tag{2.28}$$

where ω_0 is the resonance frequency, γ is the width of the resonance, and q is the Fano-parameter describing the asymmetry of the molecular spectral feature (fig. 2.15).

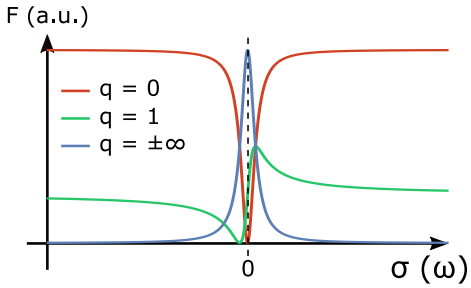

Figure 2.15: Dependance of the Fano-profile on the asymmetry parameter q

The asymmetry takes place due to the constructive and destructive interference of a broad spectral line (continuum) and a narrow spectral line (discrete resonance).

In our case, a broad continuum is the plasmon resonance and a narrow spectral line is the molecular vibration, because plasmon mode is spectrally much broader than the molecular oscillation. Depending how close they spectrally are, molecular signal may have symmetric or asymmetric shape (fig. 2.15).

What is most important, is that the spectral response of the molecule gets enhanced due to the coupling with an antenna near-field if the molecule is located in the vicinity of the nanoantenna [20].

2.3.5 *Enhancement*

As was discussed above, the molecule–plasmon coupling has a resonant nature. Therefore, the enhanced vibrational signal strengths strongly depend on the antenna resonance frequency [59, 72, 93, 94].

Due to this fact, a tailored design of antenna resonances for an optimized surface-enhanced sensing is of high importance. Therefore, this behavior was studied in order to determine the best antenna tuning [89, 95, 96]. One can define a tuning ratio as $\frac{\omega_{vib}}{\omega_{res}}$, where ω_{vib} is the vibrational frequency and ω_{res} is the resonant frequency of the antenna. It was found that the vibrational signal enhancement peaks at $\frac{\omega_{vib}}{\omega_{res}} = 0.95$ revealing a red shift of the maximum plasmonic near-field intensity with respect to the far-field antenna resonance [89].

The enhancement factor (EF) is calculated by normalizing the enhanced vibrational signal strength S to the respective non-enhanced signal and the number of molecules actively contributing to the signal. However, it is quite challenging to figure out how many molecules contribute to the signal measured. Therefore, there is another commonly used definition of EF, which relates the enhanced signal strengths to standard IR techniques (transmission, reflection) [20, 30, 72]:

$$EF = \frac{I_{SEIRA}}{I_0} \frac{A_0}{A_{SEIRA}} \tag{2.29}$$

where I_{SEIRA} is the enhanced signal, I_o is the unenhanced signal, A_{SEIRA} is the area filled with molecules in surface-enhanced IR absorption (SEIRA) measurements, and A_o denotes the area filled with non-enhanced molecules.

To investigate the areas of the largest enhancement, Dregely et al. investigated the relation between enhanced vibrational signal and plasmonic near-field intensity by evaluating the SEIRA enhancement of selectively positioned nanometer-sized molecular patches [26]. They found that the strongest vibrational signals for molecular probes are located at the antenna tips. Moving the molecular probe toward the center of the antenna or to the bare

substrate leads to the weaker signals. This observation was intuitively expected, as the strongest near-field of resonantly excited nanoantenna is at the antenna tips where the electric fields are confined (see fig. 2.12 and simulations in 3.1.1).

Following the definition of EF in eq. 2.29, an enhancement factor of about 500 000 is possible to achieve, compared to standard IR transmittance spectroscopy [20]. This corresponds to the detection of approximately 50 attograms of molecules. Depending on the antenna shape, material, and arrangement, enhancement factors may vary in the range between 1000 and 500 000.

3

Methods

This part comprises, the main steps required for the experiments discussed in the next chapters. As already shown, tuning of the plasmonic nanoantenna size, and thus resonance tuning, is crucial for the efficient enhancement of the molecular vibrations. Therefore, both nanoantennas and nanoslits utilized for the experiments were produced according to an optimized design obtained with the help of numerical simulations.

Here, simulations as well as nanostructuring are presented to provide insight into the system explored. Next, we explain the adsorption of collagen-peptides and poly-L-lysine (PLL) molecules, as they are model systems to characterize our concept of an ultrasensitive biosensor. Also, we discuss our approach of in-vitro measurements with the use of flowcells tailored for reflection and transmission measurements under IR illumination of different light sources. Finally, we discuss in detail the post-processing of the data measured.

3.1 Numerical simulations

Numerical studies of the investigated nanostructures are carried out using a commercial software package Lumerical FDTD Solutions [97] based on the finite-difference time-domain (FDTD) method [98]. As all the nanostructures are produced on CaF_2-substrates, we modeled it as a semi-infinite half space, which is the medium with properties taken from [99]. Also, we took the optical properties of gold from the same source and used them for all our simulations.

The detailed geometry of the samples is discussed below, as it may be split into two parts: the nanoantennas and the inverse ones. However, they all have a few points in common. Namely,

each of the simulations solves the problem of light propagation, where we utilize a model of a plane wave illumination with a given polarization [20, 89]. As we use the samples for in-vitro measurements, we assume the refractive index of the medium around the nanostructures to be $n = 1.33$, describing a water-based surrounding [100–102].

3.1.1 *Simulations of nanoantennas*

We fix the height and width of nanoantennas to 100 nm. As shown in fig. 2.9, it is important to take the extinction cross-section into account, where the extinction cross-section is the sum of the absorption and scattering cross-sections, which is typically much smaller than experimentally probed areas.

Nevertheless, as our simulations show in fig. 2.9, it is possible to measure the transmittance spectrum of a single nanoantenna probing a $15 \times 15 \mu m^2$ spot. One can measure smaller areas, however only up to $10 \times 10 \mu m^2$, due to the diffraction limits.

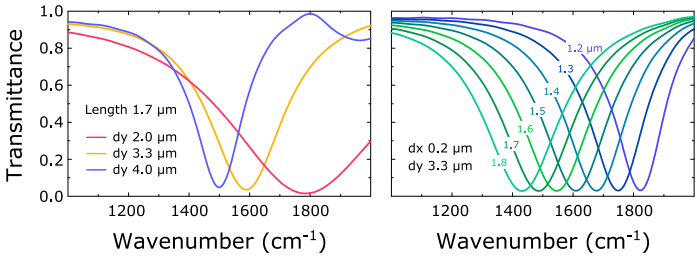

Figure 3.1: Simulated transmittance of nanoantenna array. Left panel depicts simulated transmittance of nanoantenna arrays with different grating distances, whereas the right panel shows dependency on antenna length.

Similar to single antennas, we perform simulations of the antennas in array arrangement. Here, the grating distances play an important role, as it was discussed in section 2.2.3. The left panel of the fig. 3.1 shows how transmittance of nanoantenna array depends on periodicity in y-direction, dy (fig. 2.10).

Simulations in fig. 3.1 demonstrate good agreement with theoretical discussions in sections 2.2.2 and 2.2.3. Therefore, it allows us to find optimal parameters for the samples, which we produce later and utilize as a sensing chip.

In addition to the optical response, Lumerical FDTD Solutions allows to obtain the near-field of the nanoantenna (fig. 3.2).

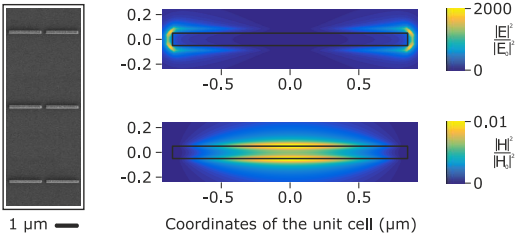

Figure 3.2: SEM image and FDTD simulation of the local E and H fields of the nanoantenna array with a length of 1.7 µm.

The antenna arrays we produced for our studies have a periodicity of antenna length plus 200 nm in x-direction, Λ_x (fig. 2.10). As it was demonstrated, a higher enhancement factor can be achieved with smaller dx [23]. However, small gaps are difficult to produce in a reliable way. Furthermore, to allow polypeptide molecules to be located at antenna tips, this gap of about 200 nm is introduced, as shown in fig. 3.2 by an image taken with scanning electron microscope (SEM).

3.1.2 *Simulations of nanoslits*

Lumerical FDTD Solutions also allow to simulate nanoslits, where we are interested in the reflectance of inverse nanostructures. Similarly to the nanoantennas discussed above, we perform simulations of the optical response for individual and array arrangements of slits (fig. 3.3). Taking into account the results of nanoslits optimization [67], we set width and height of the structures to be 50 nm for all samples we design.

The left panel of fig. 3.3 depicts simulated reflectance of the individual inverted anntenas with different length. The right panel shows simulations in the array arrangement with a constant lateral spacing of 3 µm in x-direction and 2.5 µm in y-direction (see fig. 2.11), which are different from the ones used for antennas.

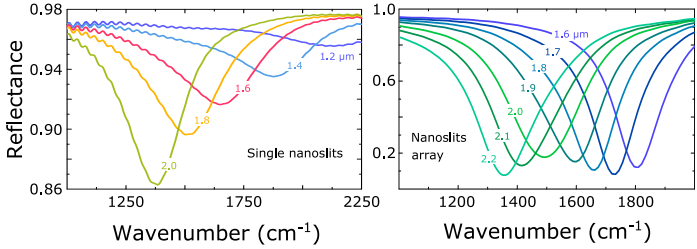

Figure 3.3: Simulated reflectance of individual nanoslits (left) and slits array (right) of different length. In both cases slits have width and height of 50 nm

.

Fig. 3.4 depits the SEM image of produced nanoslit array (left) and simulated near-field distribution (right). One can see that H-field distribution looks similar to the E-field of nanoantenna and vice versa, which is expected due to the Babinet's Principle.

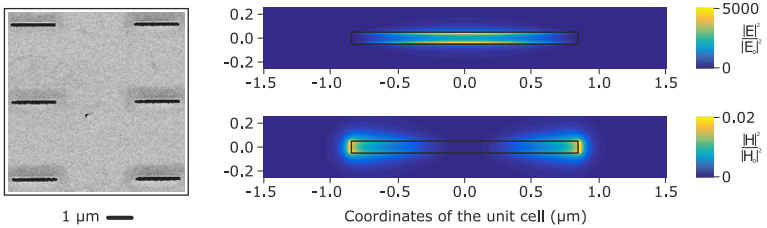

Figure 3.4: SEM image and FDTD simulation of the local E and H fields of the nanoslits array with a length of 1.7 µm.

3.2 NANOSTRUCTURING

There are many approaches to produce nanostructures [61, 67, 103]. The main technique we use for nanostructure fabrication

is a standard electron beam lithography (EBL). Here we use it to pattern a positive tone resist, poly(methyl methacrylate) (PMMA), layer acting as a mask. This method offers the possibility to tailor the geometry and properties of the structures nearly at will and allows to optimize their performance according to the needs of the experiment. However, the manufacturing flow for nanoantennas and nanoslits have some differences as discussed below.

3.2.1 *Manufacturing of the nanoantennas*

The fabrication process of nanostructured gold antennas starts with cleaning of the CaF_2 substrate. First, we immerse it in acetone for ten minutes at 50 °C and subsequently rinse it with isopropanol. Next, we clean the substrate in O_2 plasma and proceed with EBL (fig. 3.5).

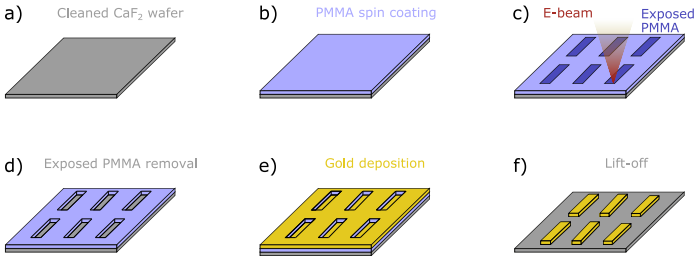

Figure 3.5: The manufacturing processes of nanoantennas. We start with a clean CaF_2 substrate (**a**) on top of which we spin coat a layer of PMMA resit (**b**). Next, we continue with photoresist patterning using E-beam (**c**). After PMMA is chemically developed (**d**), we deposit a gold layer on top (**e**). Finally, we immerse the sample into NEP solution to remove the non-exposed resist mask (**f**).

E-beam lithography begins with a double layer of the long-chain polymer PMMA, which we spin coat [104] on top of the CaF_2 wafer (fig. 3.5 **b**). We apply a 200 nm thick layer of low resolution (200K PMMA) and 50 nm (950K PMMA) of high resolution resist. After spin coating, we bake the photoresist film at 150 °C for 3 min in order to harden it.

Afterwards, the desired antenna structures are written into the PMMA with electron beam lithography (fig. 3.5 **c**). Here, electrons are accelerated and focused onto the resist layer, which leads to scission events due to inelastic collisions of electrons with the polymer chains. Thus, a long polymer-chain of the resist is cut into smaller chains. Since the bottom PMMA layer exhibits a lower resolution, an undercut structure is written into the resist which is important for the gold evaporation. By moving an electron beam, the spot of collisions is moved across the sample, which allows for arbitrary patterning of PMMA. It is important to adjust the exposure dose and exposure time in order to write rectangular shaped patterns with a width of 100 nm and lengths between 1.0 and 2.0 µm.

Next, we perform a development process to remove the exposed PMMA areas. Here, we utilize methyl isobutyl ketone (MIBK) solution in isopropanol (MIBK : Isopropanol = 1 : 2) into which the sample is immersed for 90 s. To stop the development, we subsequently put the sample into isopropanol solution for 60 s, which allows us to achieve the mask (fig. 3.5 **d**).

As exposed areas have been removed by development and bare substrate areas appear underneath, we can evaporate 100 nm thick gold layer on top via electron beam-physical vapour deposition [105] (fig. 3.5 **e**). However, a 3 nm chromium adhesion layer is evaporated before.

Finally, we remove the remaining PMMA on top of the substrate with the N-Ethylpyrrolidone (NEP) solvant. This lift-off process removes the resist mask between the gold and wafer and thus detaches gold (Au) except for the places where metal stuck to the calcium floride (CaF_2) directly.

3.2.2 *Nanoslit fabrication*

In contrast to the antenna fabrication, the manufacturing of inverse nanostructures starts with gold deposition onto the clean substrate (fig. 3.6). Here, 50 nm thick gold film is evaporated using electron beam-physical vapour deposition (fig. 3.6 **b**). Next,

130 nm PMMA (950 K) is spin-coated onto the evaporated gold layer, followed by backing at 150 °C for 3 min (fig. 3.6 **c**) on a hotplate.

Having the films prepared, we write the slit pattern using EBL similar to the antennas case (fig. 3.6 **d**). We develop the exposed photoresist using a conventional MIBK and isopropyl alcohol (IPA) solution with a mixture ratio of MIBK : IPA = 1 : 3 (fig. 3.6 **e**).

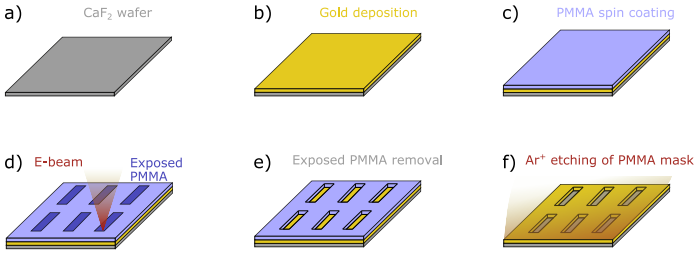

Figure 3.6: The manufacturing processes of nanoslits. We start with a clean CaF_2 substrate (**a**) on top of which we evaporate a gold layer (**b**) and spin coat a layer of PMMA resit (**c**). Next, we continue with photoresist patterning using E-beam (**d**). After PMMA is chemically removed (**e**), we apply argon ion etching to remove the non-exposed resist mask as well as gold areas where exposed PMMA was developed (**f**).

At the final step, the patterned PMMA layer was used as an etching mask to produce the nanoslit structures in the *Au* layer. The parts of the gold layer not covered with a photoresist were removed employing a physical argon etching technique (fig. 3.6 **f**). To ensure that none of PMMA was left, we clean the sample in acetone.

3.3 MOLECULAR COVER

In order to utilize the fabricated nanostructures as a sensing platform, one needs to place the molecular species into the hotspots of the near-field. A few points are of importance here, namely the geometry of the nanostructure, the size of molecules, and to chemically bind the molecules to the gold surface.

In order to accomplish mentioned tasks, these peptides require sulfur atoms, as they can directly bind to *Au*. Here, thiols are the compounds of choice, which we want to utilize as an anchor for the organic molecules. Because thiol is an organosulfur compound of the form $R-SH$, where R is any organic group, the biomolecule may be located on the radical side while S is bonded to *Au* on the other side.

3.3.1 *Adsorption of collagen-peptides*

The most convenient way of functionalization is to utilize synthesized molecules, which have a thiol group at the end. Therefore, we use specially synthesized by Felix Weiher capped collagen peptides with a thiol group (fig. 3.7), which are about 5 kDa in weight and can be used as a folding model for minicollagen proteins. In the unfolded state, the distinct single chains of the molecule exhibit only partial polyproline type secondary structures. A cooperative folding behavior leads to the collagen's typical triple-helical structure in the folded state.

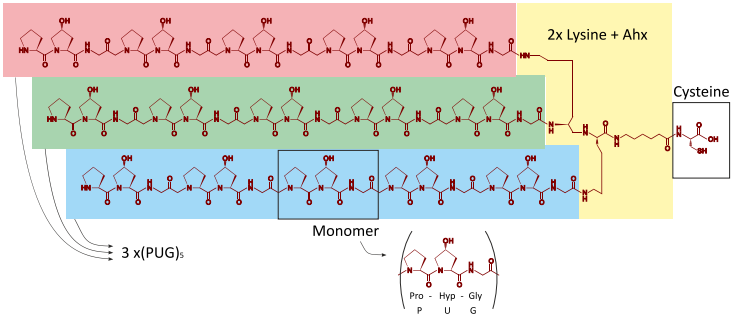

Figure 3.7: Structure of a synthesized minicollagen $3\times(\mathrm{PUG})_5$ with a thiol group at the end. Here, the monomer, which consists of the amino acid sequence of Proline (Pro, P), Hydroxyproline (Hyp, U), and Glycine (Gly, G), repeats five times in each chain.

The peptide consists of three chains each of five Pro-Hyp-Gly (Monomer, PUG) repetitions on the carboxyterminal cap (2× Lysine + Ahx + Cysteine). The molecule forms a collagen-typical

triple helix out of the three chains of $(PUG)_5$ repeats (marked with red, green, and blue in fig. 3.7). The $3\times(PUG)_5$ unfolds reversibly into the distinct single chains, which exhibit only partial polyproline type secondary structures. The carboxy-terminal capping that is at the beginning of the collagen-type triple-helix ends with cysteine, which has the thiol group ($-SH$). This is beneficial for functionalization of the gold surface, since thiol groups bond very strongly to gold. More details regarding the synthesis and its recipe can be found in [106].

To study the structural changes of the collagen-peptide monolayer, we cover the sample with synthesized molecules by immersing the nanostructures into 5 µmol D_2O-based solution of collagen peptides functionalized with thiol bonds for 24 h.

3.3.2 *Functionalization with poly-L-lysine*

For real-world applications, the synthesized molecules are, however, not an option. Furthermore, typically investigated biospecies are much larger in size and thus a close-packed molecular layer may prevent the folding activity due to steric hindrance.

Therefore, thiol-linker chemistry is an alternative way for the coverage of the nanostructures [107]. Here, we use two types of thiols, namely 11-mercaptoundecanoic acid (MUA) and 11-mercaptoundecanol (MUoL) for the antenna functionalization. These bind to the gold antennas and provide the required larger surface-polypeptide-distance as well as the lateral spacing between the molecules, because MUoL is not able to bind peptides but binds to gold (fig. 3.8). Thus, an optimal ratio of MUA/MUoL coverage allows poly-peptides to be anchored but still have folding/unfolding abilities.

Among the many polypeptides, poly-L-lysine is a suitable model system for our experiments, as it has the α-helical conformation in the folded state and β-sheet in unfolded. In other cases, it may have a random coil conformation or exhibit a mixture of the mentioned secondary structures.

All chemicals necessary for the functionalization were purchased from Sigma Aldrich: ethanol, NaOH, HCl, deionized water, trisodiumphosphate Na_3PO_4 (96%, CAS number 7601-54-9), sodium chloride NaCl, 2-(N-Morpholino)-ethanesulfonic acid (MES, 99.5%, CAS number 145224-94-8), 11-mercaptoundecanoic acid (MUA, 98%, CAS number 71310-21-9), 11-mercaptoundecanol (MUoL, 97%, CAS number 73768-94-2), N-Hydroxysulfosuccinimide sodium salt (NHSS, 98%, CAS number 106627-54-7), N-(3-Dimethylaminopropyl)-N′-ethylcarbodiimide hydrochloride (EDC, 99%, CAS number 25952-53-8), and poly-L-lysine (15 – 30 kDa, CAS number 26124-78-7).

The functionalization of the gold surfaces with MUA/ MUoL and PLL follows the protocol described by Fallah et al. [108]. For our experiments, we varied only the immersion times and the ratio of MUA/MUoL.

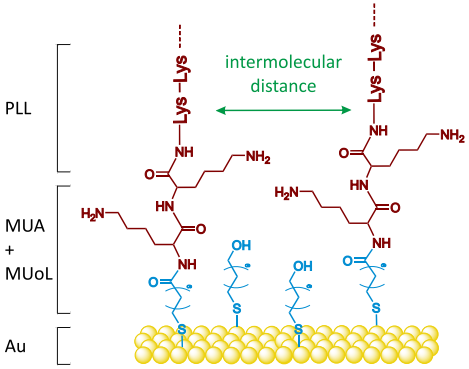

Figure 3.8: Functionalization scheme. PLL molecules are immobilized on a gold surface using a mixed monolayer of MUA and MUoL. The intermolecular distance between PLL molecules, which can be adjusted by the composition of MUA/MUoL, and their distance to the gold surface are crucial for conformational changes.

Prior to the functionalization, we cleaned the gold nanoantennas in an O_2 plasma (0.4 mbar, 250 W, 5 min). We then immersed the sample in a 1 µmol solution of MUA/MUoL in ethanol for 48 h. The ratio between MUA/MUoL in solution was 1:99. Afterwards, we rinsed it with ethanol and carefully dried it with

nitrogen. Next, to predispose the carboxyl group of MUA for the binding to the PLL, we immersed the sample into a mixed NHSS/EDC solution (concentrations 15 mmol/75 mmol) in MES buffer for two hours. Afterwards, the sample was rinsed with D_2O and directly transferred to a 1 mg/mL PLL-solution in phosphate-buffered saline (PBS) buffer. After 60 h in PLL solution, the sample was rinsed with water and directly mounted into the fluidic cell filled with D_2O. All solutions were directly prepared before the usage.

The advantage of this functionalization scheme is hidden in the thiol-linker approach, as it allows for binding the different molecules of different sizes to the gold surface by varying the MUA/MUoL concentrations.

3.4 FOURIER-TRANSFORM INFRARED SPECTROSCOPY

Most of results discussed in this dissertation are obtained via Fourier-transform infrared (FTIR) spectroscopy. This section describes the basics of FTIR and provides insights into the measurement geometries used. Also, we discuss the role of a light source and light source applied in our measurements.

3.4.1 *Working principle of FTIR spectroscopy*

The scheme of the FTIR is depicted in fig. 3.9. Light may be emitted by a built-in light source or it may be incoupled from an external source. Next, the beam is split by a 50:50 beam-splitter. After beams are reflected by the mirrors, they are superimposed again at the beamsplitter and interfere constructively or destructively depending on the relative phase. The key component here is a movable mirror, at each position of which the intensity of the radiation is recorded. Plotting the intensity of the light versus the respective mirror position x gives a so-called *interferogram*, shown in the inset.

Optionally, the light is then guided to the microscope, where it illuminates the sample. Here, two illumination geometries are

possible (fig. 3.9). If the bottom movable mirror is moved aside the beam path, light propagates through the transmission channel. Here, the sample located on the stage is hit by light from the bottom side. However, if bottom movable mirror is placed to reflect the light, it takes a reflection channel. In this case, the sample is illuminated from the upper side and reflected light is measured. Both transmitted and reflected optical signals are then collected by the lens and recorded by a detector.

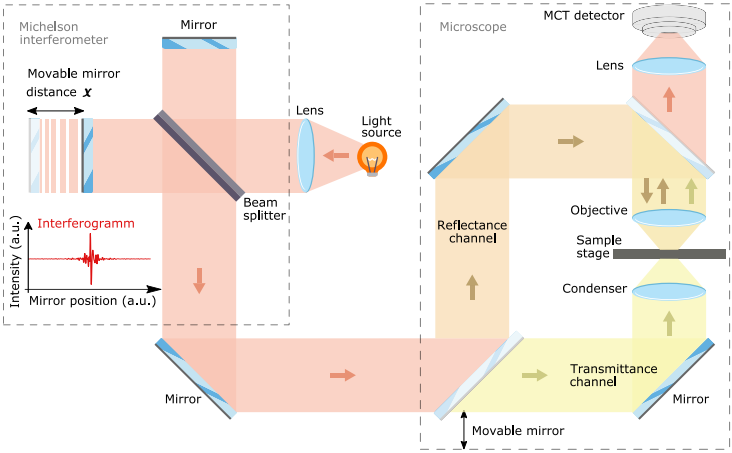

Figure 3.9: Scheme of the Fourier-transform infrared (FTIR) experimental setup. Here, the beam from a light source is coupled to the Michelson interferometer. Next, the light is coupled to the microscope, where both reflection and transmission measurements are carried out.

The spectral signal, taken with a detector, holds the spectral information not only of the light source but also of optical elements, atmospheric gases as well as other influences of the surrounding. Therefore, we eliminate these features by taking a reference measurement, as it is shown in fig. 3.10. The key idea is to acquire the reference spectrum of the bare substrate. Depending on the measurement geometry, this can be done either by the measurement next to the antennas (transmittance) or recording the optical response from the metal mirror (reflectance), which is made of the same material as the nanostructure. After normalizing sig-

nal spectrum to a reference one, we obtain the optical response of the sample only. Hence, the final spectrum is either relative transmittance or relative reflectance, which we analyze after the measurements are carried out.

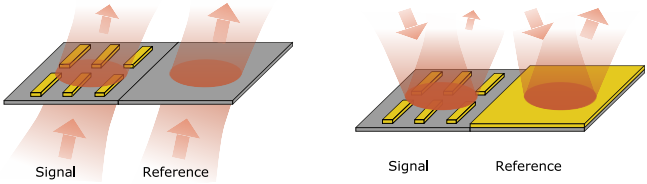

Figure 3.10: Scheme of the Fourier-transform infrared (FTIR) experimental geometries. Here, the light either passes through or reflects from the sample. Depending on the measurement geometry, reference is taken either at the bare substrate (transmittance) or at the metal mirror (reflectance).

In our lab, all infrared spectra are measured using a Bruker Hyperion 2000 IR microscope coupled to a Bruker Vertex 80 spectrometer with an optical path purged with nitrogen. The polarisation of the incident light can be set with an IR wire grid polariser. For the measurements of nanostructure array an aperture size of $50 \times 50\,\mu m^2$ and 15-fold magnification is used, whereas individual nanostructure was measured with 36-fold magnification and $10 \times 10\,\mu m^2$ aperture size. Thus, we apply the apperture to define the area which we measure. All spectra were acquired with a liquid-nitrogen-cooled mercury-cadmium-telluride (MCT) detector.

As proteins and polypeptides are able to undergo the desired structural transitions being immersed into the aqueous surrounding, we designed tailored fluidic cells to carry out the in-vitro measurements.

3.4.2 *Fluidic cells*

To perform measurements in inverse reflection geometry, we designed a so-called reflection flow cell (fig. 3.11). Here, function-

alized antennas are immersed in an aqueous environment and a CaF_2 substrate is used as a window to optically probe the sample.

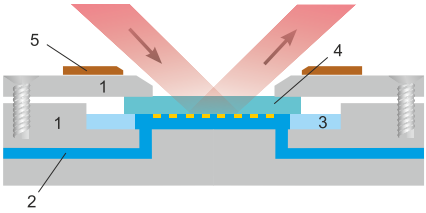

Figure 3.11: Schematic drawing of the reflection flow cell

The cell consists of several parts: 1 – Sample holder made out of TECAPEEK, 2 – Flow channel for different solutions, 3 – polydimethylsiloxane (PDMS) mask for sealing the cell, 4 – flipped CaF_2 wafer on which nanostructures are produced, 5 – the heater. TECAPEEK was chosen due to its chemical and thermal properties, as polypeptides folding was induced by temperature change or chemical impurities of the aqueous surrounding. For these reasons, the fluidic channel and heater are important components of the cell.

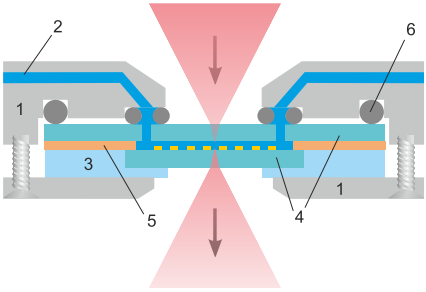

Figure 3.12: Schematic drawing of the transmittance flow cell

Transmission fluidic cell has to be transparent for IR light from both sides (fig. 3.12). To accomplish this requirement, we utilized two CaF_2 wafers, where the upper one has drilled channels as well as the spacer to supply liquids, and the lower one has the nanostructures manufactured. The cell consists of a metallic

holder (1) with drilled flow channels (2), PDMS sealing at the bottom (3), already discussed wafers (4), photoresist (7µm thin) or SiO_2 (1µm thin) flat spacer (5) etched in the middle, and O-Ring sealing (6). The sealing inside the cell is achieved by the chemical bonding of CaF_2 with SiO_2 [109] and PDMS mask outside [110] the SiO_2/CaF_2 interface.

The materials chosen for both transmittance and reflection flow cells are chemically stable, meaning that solutions in the channel do not react with the cells. Also, the sample is mechanically fixed and thus spectra are taken from the same spot always. In the case of the reflection flow cell, TECAPEEK exhibits a weak thermal expansion making the measurement stable at different temperatures.

3.4.3 *Light sources*

As well as many other aspects, the light source plays an important role in the FTIR measurements. A typical light source used in most of FTIR studies is a Globar (fig. 3.13), which is spectrally broad and thus allows for investigations of various molecular species.

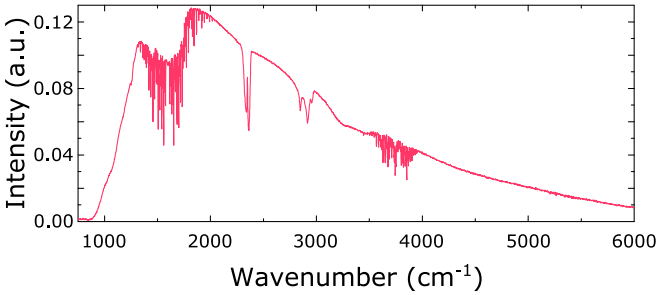

Figure 3.13: Globar spectrum measured through the a CaF_2 window

However, signal-to-noise ratio (SNR) of a Globar may become an issue for the studies of thin molecular layers, as root mean square (RMS) of a light source needs to be lower than the signals measured [111]. In other words, to reach a higher sensitivity one

may utilize a light source with a higher brilliance [112], where the brilliance is defined as:

$$\text{brilliance} = \frac{\text{photons}}{(\text{s})(\text{mm}^2)(\text{sr})(0.1\%\text{BW})} \tag{3.1}$$

Globars reach a brilliance of $10^{15}(\text{ph/s/mm}^2\text{/sr/0.1\%BW})$, which is typical for thermal light sources.

A synchrotron light sources [113] are one of the possible alternatives providing a higher brilliance, which is several orders of magnitude larger and reaches 10^{18} ph/s/mm^2/sr/0.1%BW [114]. The drawback is that synchrotron radiation requires large central facilities. However, it provides spectrally broadband light, similarly to a Globar, but with better SNR (fig. 3.14).

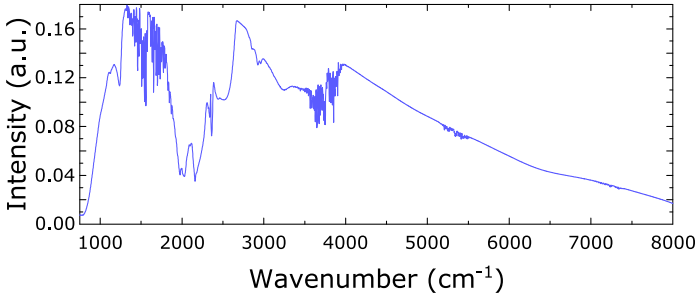

Figure 3.14: Synchrotron spectrum measured at SLS, Paul Scherrer Institute

We have performed measurements at several synchrotron facilities, such as SOLEIL [114], ANKA [115], and Swiss Light Source (SLS) [116]. The results presented and discussed in this thesis are obtained at SLS, located in Paul Scherrer Institute (PSI), Switzerland.

As already discussed, it would be ideal to have a broadband tabletop light source with high brilliance and low RMS. A tunable laser light source is able to fulfill these requirements, which allows to adjust the central wavelength of emitted light and thus cover the spectral range of interest [117, 118]. Furthermore, if the laser spectrum has a spectrally broad enough width, the measurements of molecular vibrations are possible without wave-

length tuning [119]. In general, many laser light sources are suitable, but a fiber-feedback optical parametric oscillator (OPO) was the one we utilized for the studies discussed in this dissertation [111, 112]. Beam path of such laser setup scheme is taken from [111] and adopted in fig. 3.15. Here, the IR light is generated in a 2-mm long $AgGeSe_2$ crystal by mixing signal and idler beams of a post-amplified fiber-feedback optical parametric oscillator (ffOPO) system.

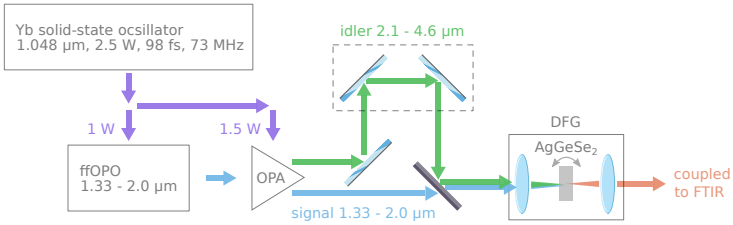

Figure 3.15: The system is pumped with Ytterbium (Yb) solid-state oscillator, the light of which pumps fiber-feedback optical parametric oscillator and optical parametric amplifier (OPA). $AgGeSe_2$ crystal performs difference frequency generation (DFG), which provides the IR light required for the FTIR measurements. Taken and adopted from [111].

This laser system was installed in our lab and coupled with FTIR setup. Fig. 3.16 depicts its spectrum tuned to the wavelength of amide-I vibration (around 1650 cm^{-1}).

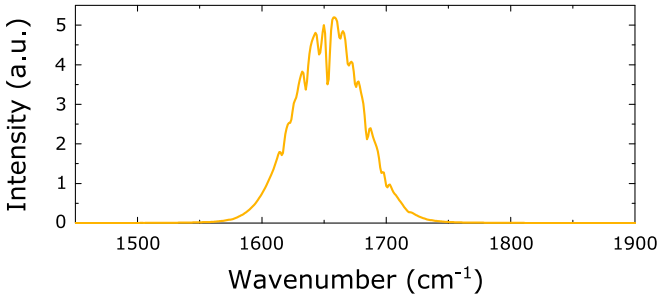

Figure 3.16: Spectrum of the optical parametric oscillator (OPO) tuned to cover the amide-I spectral region

3.5 DATA ANALYSIS

As discussed in chapter 3.13, the measured spectrum of a functionalized, resonantly tuned nanoantenna holds spectral features of both molecules and plasmon, where vibrational feature has an asymmetric shape (Fano-profile). To extract the signal of interest or visualize it in a more clear way, we apply a different methods for data post-processing.

3.5.1 *First derivative*

Calculating the first derivative is one way to examine the spectrum for very weak vibrational features. In general, this means that we plot $\frac{dR}{d\tilde{\nu}}$ versus $\tilde{\nu}$, where R is a reflectance spectrum and $\tilde{\nu}$ is a wavenumber.

However, taking the first derivative without pre- and post-smooth of the spectrum leads to noisy spectra. Therefore, we perform a smoothing of the spectra measured in order to fix the parameters for all data obtained (fig. 3.17).

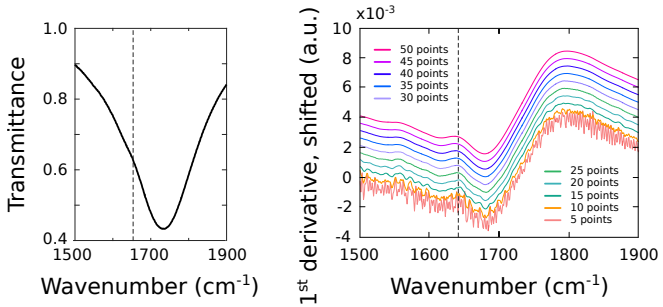

Figure 3.17: First derivative analysis with different number of smoothing points. Spectral resolution is 2 cm^{-1}.

The left panel of the fig. 3.17 shows the spectrum measured, which exhibits a plasmonic resonance and a weak vibrational feature marked by the dashed line. The right panel depicts derivatives taken with different pre- and post-smooth. Here, we perform a Savitzky-Golay smoothing [120] before and after taking

derivatives applying smooth windows of a varying number of points. As seen at the right panel, if we apply a narrow smoothing window, a high noise hampers the visibility of spectral features. Too strong smoothing, however, leads to loss of the features. Therefore, we fix the smoothing window to be 12 cm^{-1} wide, as this is optimal for the visualization of vibrational features in our experiments.

3.5.2 *Baseline-correction*

Another approach to reveal the vibration feature from the spectra measured is a so-called baseline-correction. This method is based on the perfect smoother developed by Eilers [121]. Here, we reconstruct the broad asymmetric plasmon resonance (fig. 3.18). Next, we normalize measured spectrum (blue) by a baseline reconstructed (orange), which gives a so-called baseline-corrected spectrum (red). After normalization, the vibrational features, marked by dashed lines, are clearly visible.

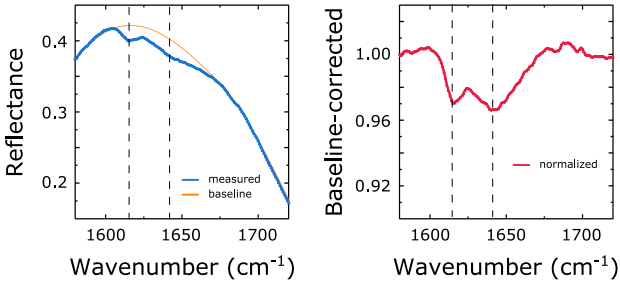

Figure 3.18: Baseline-correction of measured spectra

Baseline-correction allows for obtaining the profile of the enhanced vibrational feature. It can thus be compared to a non-enhanced molecular response measured by conventional infrared spectroscopy. Consequently, molecular Fano-profiles and enhancement factors were investigated in great detail [20, 122] with the help of this analysis method.

3.5.3 *Principal component analysis*

However, baseline-correction might not be the best choice to analyze a dynamic system, where transitions are represented by changes in vibrational features. The limiting factor is the baseline reconstruction, which we perform for each spectrum and thus imperfections of the baseline also cause differences in normalized spectra. This might lead to artifacts if the changes in the system are weak.

Analysis of the first derivative does not have this drawback. However, due to a smoothing procedure (fig. 3.17), this method might appear not sensitive enough.

Therefore, we also analyze experimental data utilizing a method focused on a variance of the system, namely principal component analysis (PCA). PCA is a standard method known from multivariate statistics, which extracts the correlation in the data set by applying a principal axis transformation such as that the variance of the data is largest [123]. In other words, PCA is one of the methods for identifying patterns and similarities in the data set, which is also often applied in machine learning and data mining.

Technically speaking, this is a problem of finding the eigenvectors and eigenvalues. Meaning that common patterns, which are present in all data sets, are represented as eigenvectors. The stronger a particular pattern is pronounced, the larger eigenvalue it has. Thus, the overall data set is considered as linear combination of a limited set of eigenvectors [124, 125]:

$$\mathrm{Spectrum}_i = A + \sum_{j=1}^{N} \mathrm{SC}_{i,j} \cdot \mathrm{PC}_i \tag{3.2}$$

where A is the average of all measured spectra, N is the amount of measured spectra, SC is the spectrum-specific eigenvalues named score, PC is an eigenvector called principal component. As eq. 3.2 describes, we substract the average from each spectrum measured and then decompose the data set into an orthogonal and uncorrelated set of eigenfunctions (PCs) and eigenvalues (SCs).

As scores are spectrum-specific, the detailed analysis of them allows for clustering the data based on system variances. For more detailed discussion of the application of PCA in our studies please refer to chapter 5 and [124, 125].

4

Nanoslits for collagen-peptide dynamics observation

This chapter is based on the following publication [126]:

R. Semenyshyn, M. Hentschel, C. Huck, J. Vogt, F. Weiher, H. Giessen, and F. Neubrech, *"Resonant plasmonic nanoslits enable in-vitro observation of single monolayer collagen-peptide dynamics"*, ACS Sensors 4, 1966 (2019).

Nanoantenna arrays have been successfully utilized for biosensing in air and water surroundings [8, 29–32, 34, 37–39, 127]. All these studies have demonstrated the reliable detection of monolayers of proteins. Proteins, the misfolding of which is associated with diseases [128–130], are in fact commonly composed of several individual monomers and thus complex entities. Collagens, for instance, are a good example, as they are so-called trimers. In other words, they consist of a triple helix of peptides with polyproline helical structure. Such collagens are in fact structural building blocks in many complex proteins. Therefore, they are an ideal model system for more complex and biologically relevant systems.

In this chapter, we demonstrate in-vitro monitoring of structural changes of collagen-like molecules utilizing resonant plasmonic nanoslits as a sensing platform based on surface-enhanced infrared absorption (SEIRA) spectroscopy. While this is an important step on the quest for improved molecular recognition for biologically relevant entities, it further requires higher sensitivity, as the used synthesized collagens are in fact small molecules exhibiting comparably small vibrational signal strengths. These expected small signals require a detailed analysis of the coupling between the plasmonic resonance and the molecular vibration in

order to extract the conformational change from the spectral response.

As mentioned, we report the use of plasmonic nanoslits as a SEIRA platform, which feature plasmonic resonances according to Babinet's principle (see chapter 2.2.4) and provide a higher average SEIRA signal inside the slit [67]. Furthermore, nanoslits exhibit a smaller resonance shift for a changing effective refractive index of the surrounding due to smaller amount of solution per unit cell. This is an advantage for the folding studies induced by temperature changes.

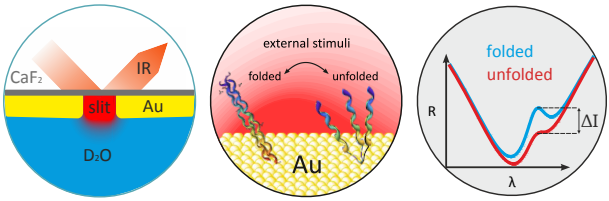

Figure 4.1: We measure the reflectance (R) of the nanoslit array with peptides in inverse reflection geometry (left). A monolayer of collagen-peptides is adsorped on the gold surface of the nanoslits (middle). We apply an external stimulus to induce changes of molecular secodary structure, resulting in different intensities (I) of the amide I vibration (right).

The basic idea of our experimental study is shown in fig. 4.1. We perform a standard Fourier-transform infrared (FTIR) spectroscopy to probe the optical response of resonant plasmonic nanoslits in inverse reflection geometry (left). In order to perform in-vitro measurements, we cover the nanostructures by a monolayer of capped collagen peptides (middle) and immerse them into an aqueous surrounding (D_2O). We analyze optical responses of collagen-peptides in different surroundings and reveal changes in vibrational signal (right).

The synthesized collagen-peptides are about 5 kDa in weight and can be used as a folding model for minicollagen proteins [106]. In the unfolded state, the distinct single chains of the molecule exhibit only partial polyproline type secondary structures. A cooperative folding behavior leads to the collagen's typical triple-helical structure in the folded state. To observe folding

of triple helices, monitoring the intrahelical vibrations is required [131] and thus, high SEIRA signal is necessary.

In this experiment, the conformational changes of collagen peptides are induced by two different external stimuli, namely, a surfactant as well as temperature change. The goal is to detect the secondary structure of the molecules and its dependence on the surrounding properties by monitoring the amide I vibration, which is characteristic for different conformational states.

4.1 NANOSLITS FUNCTIONALIZATION

To start in-vitro measurements, we utilize a tailored reflection flow cell (fig. 3.11) which allows to measure the nanostructures in an aqueous environment in inverse reflection geometry. The were fabricated using a standard electron beam lithography (EBL) process and subsequent argon-ion milling, more details can found in chapter 3.2.2.

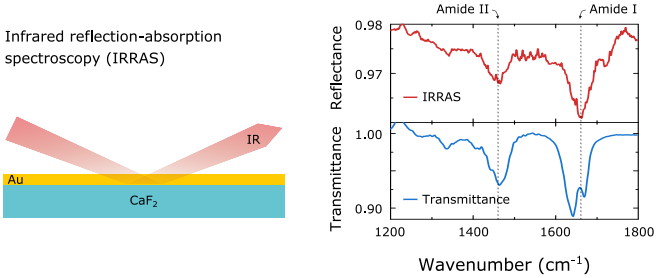

Figure 4.2: Using infrared reflection-absorption spectroscopy (IRRAS) measurements (left), we acquired the optical response of a collagen-peptide monolayer self-assembled on a gold mirror. Using IRRAS and transmittance measurements (right) show a good agreement.

To perform SEIRA spectroscopy, we need to place the molecules into the so-called "hot spot" of the nanostructures. As we utilize nanoslits, the collagen-peptides should be located inside the slits [67]. The most straightforward approach is to bind the peptides to the gold surface itself with standard gold–thiol chemistry

(chapter 3.3). Parts of the peptides will therefore also be present inside the slits, as they can cover the side walls.

In order to check the self-assembly of molecules on the gold surface, we immerse a gold mirror into D_2O-based solution of collagen-peptides (24 h in 5 µmol solution) and acquire infrared reflection-absorption spectrum. For comparison, we utilized a tailored microfluidic cell (fig. 3.12) and measured relative transmittance of about 10 µm thick solution of collagen-peptides with 10 µmol concentration. Both optical signals demonstrate a good agreement (fig. 4.2), which proves the binding ability of the synthesized molecules.

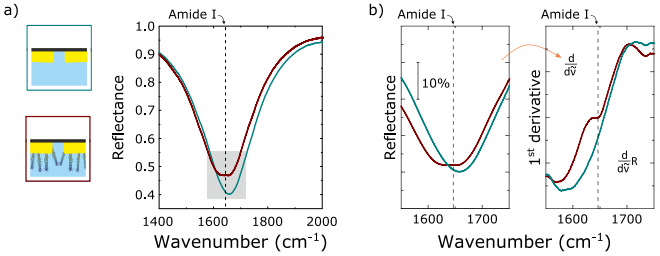

Figure 4.3: Measured reflectance spectra before (dark green) and after (dark red) functionalization (**a**). Zooming into the grey-shaded reflection spectrum inset (**b**) reveals that the vibrational feature is difficult to see (left panel) and thus we analyse the first derivative of the optical response (right panel).

Having the functionalization procedure defined, we cover the sample with collagen-peptides. Figure 4.3 depicts the reflectance of 1.7 µm long nanoslits being immersed in D_2O before (dark green) and after (dark red) functionalization. One should mention that a red shift of the plasmon resonance frequency is observed after molecules covered the nanostructures (fig. 4.3 **a**). This observation is expected, because collagens adsorbed on the gold surface slightly increase the effective refractive index [132].

The spectral region of the amide I vibration is marked by dashed lines. Obviously, the vibrational feature is imprinted onto the reflectance spectrum of functionalized slits (left panel). Although the signal appears small, it is not observed for the bare sample. Such a weak signal is expected, as the molecules are small in

size (minicollagens) and thus have a low number of vibrations contributing to the amide I feature.

For a detailed analysis of the spectra, we plot the first derivative of the reflection spectra (right panel) according to the procedure discussed in chapter 3.5.1. Obviously, the amide I vibration is clearly visible. Thus, we are able to detect a monolayer of collagen-peptide. Under these conditions we can track the changes of amide signals, which means we can observe the conformational changes.

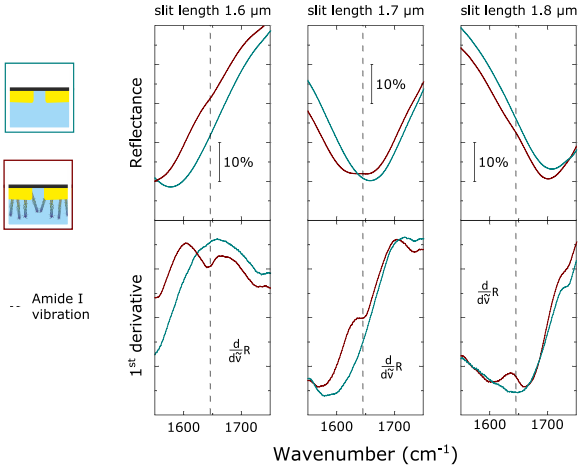

Figure 4.4: Measured reflectance of three slit arrays of different length immersed into D_2O before and after collagen-peptide functionalization. The upper panel depicts reflectance spectra, whereas the lower shows the first derivative of the reflectance. After functionalization of the bare slits (dark green), the amide I vibration (spectral position marked by dashed line) is imprinted onto the plasmonic resonance (dark red).

In addition to nanoslit lengths (see chapter 2.3), the intensity of molecular features depend also on slight deviations in molecular coverage as well as a possibly varying quality factor of the array. In order to optimize the SEIRA performance, we varied the antenna length. For all lengths, qualitatively, the same results were obtained (fig. 4.4). The amide I vibration is most pronounced when its energetic position is slightly detuned from the plasmon

resonance. Thus we chose a slit array with a length of 1.7 µm as the most promising one. Nevertheless, we performed all the measurements with other arrays as a verification of the main results.

As we have nanoslits covered with collagen-peptides, we continue with unfolding experiments of the prepared monolayer. Similar to many proteins, the folding behavior of collagen peptides is determined by the external environment. This allows us to switch the conformation of the molecule by changing the aqueous surroundings.

4.2 DENATURATION INDUCED BY CHEMICAL STIMULI

It has been shown that sodium dodecyl sulfate (SDS) leads to a change in secondary structure of proteins [3, 133]. At higher concentrations of SDS solution, the surfactant binds on the protein hydrophobic sites, which causes unfolding of the triple helical [133]. The neutral surrounding removes SDS from the molecule so that a triple helical structure reforms back. In other words, SDS causes a reversible denaturation of the biomolecules.

On the other hand, heating of collagen-peptides leads to structural transitions as well [106, 134]. In contrast to folding dynamics induced by SDS, heating allows for tracking of intermediate states during secondary changes. However, one needs to account for the spectral shifts due to the refractive index changes [135], which are larger in case of heating than addition of SDS impurity.

To examine if our nanosensor is able to detect a structural difference of the collagen-peptide monolayer, we induce the conformational changes with an SDS solution, which allows a direct transition from natural to denaturated states, as shown in fig. 4.5 for two different length.

The upper panel of fig. 4.5 **a** depicts the measured reflectance spectra, where the first derivative of the optical response is shown on the lower panel. The array of nanoslits being immersed in D_2O-based solution has the plasmonic resonance frequency close to the amide I vibration. As seen in the lower panels, it is con-

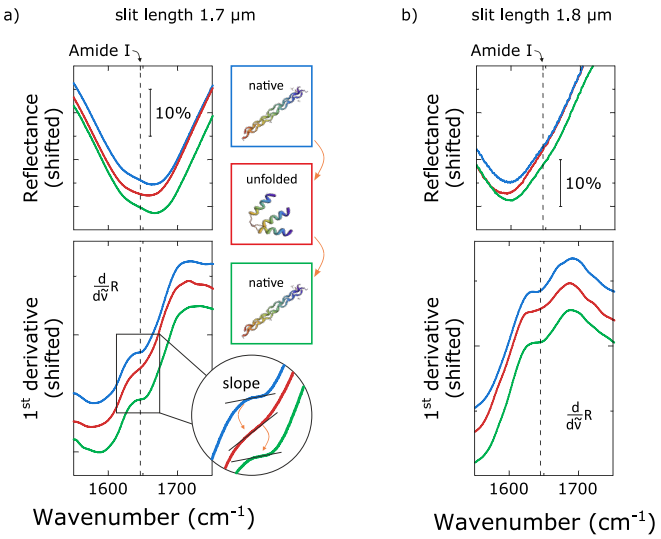

Figure 4.5: Changes in secondary structure are induced by external chemical stimuli. The upper panel of both (**a**) and (**b**) depicts reflectance spectra measured, whereas the lower one shows the first derivative of the optical response. The position of the characteristic vibrational feature of collagen-peptide is shown as a dashed line. Utilizing a specially tailored flow cell, we immersed the sample into different surroundings in the following sequence: D_2O (blue), SDS solution (red), D_2O (green). Monitoring the slope change of the amide I spectral feature, we detect reversible structural changes of collagen peptides: from triple-helix to unfolded and back. The results are shown for two slit arrays: 1.7 µm(**a**) and 1.8 µm(**b**).

venient to monitor the change of the slope at the frequency of amide vibration in order to track the changes of the secondary structure.

Similar to fig. 4.3 **a**, the characteristic vibrational feature of the molecules (dashed line) is visible. The three different measurements are color-coded here. We fill the flow cell with D_2O right after functionalization, which is now the initial state (blue curve).

Next, we exchange the solution in the fluidic cell and add SDS to the surrounding (red curve). The slope represents a weaker amide I vibration. As mentioned above, such behavior was expected, because SDS causes denaturation of peptides. For colla-

gen peptides, this starts by breaking the bonding between helices of the triple helix structure. Therefore, there are less vibrations at the characteristic frequency, leading to a weaker spectral feature. The recipe of SDS solution we used was introduced previously in the literature [136].

As the last step, we remove the SDS solution D_2O (green curve). Consequently, it is clear that the triple-helical structure of collagen peptides reforms and leads to a more pronounced spectral response, as observed.

The same results are obtained for measurements performed for the slit arrays of different length (fig. 4.3 **b**), which proves the reliability of our sensor.

4.3 THERMALLY INDUCED CONFORMATIONAL CHANGES

The conformational transition from folded to unfolded states is crucial for understanding folding dynamics. Our previous results show that our nanosensor is capable of such experiments. Thus, to track the step-by-step transition of the collagen-peptide ensemble from the folded to the unfolded state, we utilize a thermal stimulus to trigger structural changes.

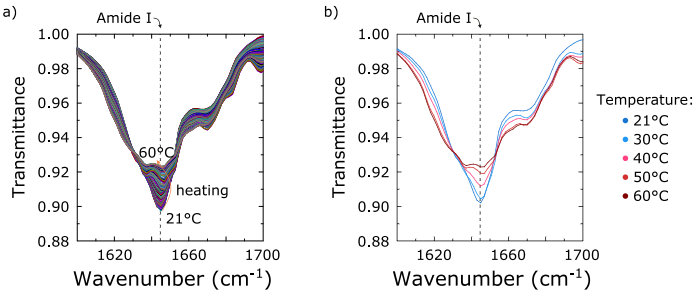

Figure 4.6: Reference measurement of collagen-peptide induced thermally folding. (**a**) The collagen solution with a concentration of 10 µmol and thickness of about 10 µm measured continuously during the heating from 21 °C to 60 °C, which are 250 spectra in total. (**b**) To draw a clearer picture, each 50^{th} spectrum is depicted.

First, we perform a reference measurement. We heated a 10 µmol solution of collagen-peptides filled in a the transmittance flowcell (fig. 3.12). We execute constant heating from room temperature up to 60 °C and acquire spectra continuously (fig. 4.6), which was in total 250 spectra. A decrease in amide I vibrations with increasing temperature is observed.

To further analyze the data, we applied principal component analysis [137] to the spectra (fig. 4.7).

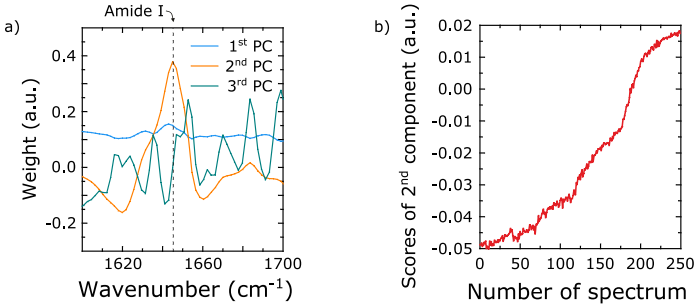

Figure 4.7: The principal component analysis (PCA) of the reference measurement. (**a**) Three PCs with finite score values have been found, where the second PC represents changes of amide I vibration due to heating. As 250 spectra were accumulated during heating from 21 °C to 60 °C, we investigated each score of the 2^{nd} PC (**b**) to depict the variance of amide I during temperature change.

As discussed in chapter 3.5.3, PCA does not require any input parameters or any knowledge about the physical processes involved. Nevertheless, a physical interpretation of the PCs can be assigned if there is a certain pre-knowledge on the system. In our case, spectra of heated collagen-peptide solution have spectral feature of amide I vibration at about 1644 cm^{-1}. As the 2^{nd} PC has a spectral feature at the frequency of this vibration (fig. 4.7 **a**), we can conclude that the 2^{nd} PC holds the information about collagen-peptides dynamics. Therefore, we plot the scores of the 2^{nd} PC versus the number of spectra measured (fig. 4.7 **b**). For more details regarding score and principal components, please refer to chapter 3.5.3.

The fig. 4.7 **b** shows that scores of the 2nd PC increase with number of spectra. This indirectly indicates the way of the amide I intensity changes. Taking into account the fact that each spectrum may be represented as the linear combination of the PCs and that peak of the 2nd PC is facing upwards, the larger the score of PC spectrum is, the less pronounced is amide I feature.

Thus, PCA of the reference measurement reveals that heating of collagen-peptides solution leads to unfolding of the molecules. We perform also a circular dichroism (CD) measurements at 224.2 nanometer using 1 mm cuvette (fig. 4.8). Here, we prepare a 60 mmol solution of collagen-peptides and heat it from 5 °C up to 95 °C. Furthermore, similarly to heating, we measured CD spectra during cooling of the system. The signal change with temperature indicates unfolding-folding dynamics, which agrees well with literature [134].

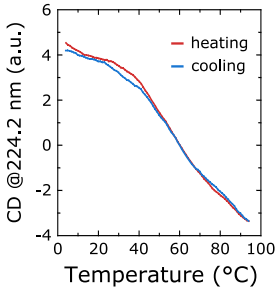

Figure 4.8: Circular dichroism CD measurements of a 60 mmol solution of collagen-peptides heated from 5 °C up to 95 °C and cooled back to initial temperature while acquiring CD spectra. The signal change with temperature indicates unfolding-folding behavior.

Next, we proceed with temperature-induced studies of the collagen-peptide monolayer adsorbed on the nanoslits (fig. 4.9). In the following studies, we start our experiments at the temperature of 27 °C. Next, we heat the solution with the help of a proportional integral derivative (PID) controller up to 70 °C in steps of 10 °C. We perform reflection measurement at each temperature step. Similar to heating, we acquire the optical response in distinct temperature steps during the cooling of the system.

We plot the spectra in a way that the measurement of the first temperature point is on top and the last at the bottom (fig. 4.9).

As seen from the reflectance spectra (fig. 4.9, color-coded solid curves), the resonance frequency of the nanoslit array shifts with temperature, as the heating of the D_2O-based solution results in slight changes of the refractive index [135]. Similar to experiments of SDS-induced denaturation, the first derivative of the measured spectra provides a more convenient way for monitoring folding of collagen peptides. As known from literature and our reference measurements, the intensity of collagen-peptide amide I vibration decreases with increasing temperature and has reversible behavior. Furthermore, the strength of this molecular signal reveals the fraction of collagen folded [134]. Therefore, we extract the vibrational signal of molecules from our experimental data at each temperature step.

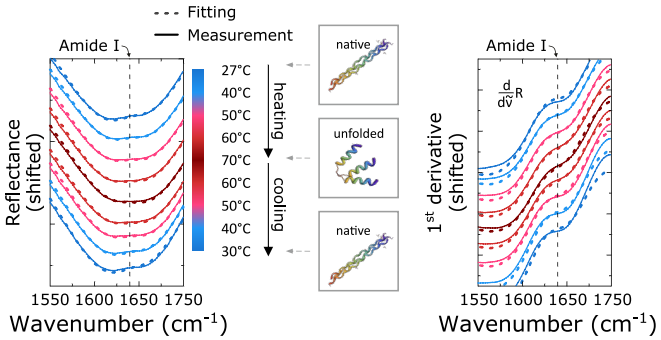

Figure 4.9: Monitoring thermally induced conformational changes of collagen peptides. The frequency of amide vibration is marked by a vertical dashed line; the temperature steps are color-coded. Solid lines depict the optical response at each temperature step. Reflectance spectra (left panel) exhibit a spectral shift due to the temperature variation. However, the first derivative of the optical response (right panel) reveals the change of the spectral feature at the frequency of amide vibration. Dashed curves show the results of fitting the experimental data by an analytical model, which shows excellent agreement with the measured optical response.

To describe the optical response analytically, we utilize a harmonic oscillator model (chapter 2.3.4). We assume that a plas-

monic resonance around the resonance frequency is symmetric and has a Lorentzian profile. Also, because of the coupling of the molecules to the nanostructure, the vibrational feature of collagen peptide has a Fano profile [86]. However, due to the mismatch of the dipole moment between the molecular vibrations and plasmonic resonance of the nanoslits, the coupling is weak despite the good match of the resonant frequencies. Hence, the spectrum measured is the sum of both:

$$\mathrm{Spectrum}(\omega) = L(\omega) + F(\omega) \tag{4.1}$$

with

$$L(\omega) = 1 - \frac{A}{\left(\frac{\omega-\omega_{res}}{\Gamma_{res}}\right) + 1} \tag{4.2}$$

and

$$F(\omega) = \left[1 - \frac{\left(\frac{\omega-\omega_{vib}}{\Gamma_{vib}} + q\right)^2}{\left(\frac{\omega-\omega_{vib}}{\Gamma_{vib}}\right)^2 + 1}\right] \cdot I \tag{4.3}$$

A is the modulation depth of plasmonic resonance, Γ_{res} is the full width at half-maximum of the plasmonic resonance, ω_{res} is the resonance frequency of nanostructure, ω_{vib} is the frequency of amide vibration, Γ_{vib} is the full width at half-maximum of amide vibration, and q is the asymmetry factor, which depends on the tuning ratio $\omega_{vib}/\omega_{res}$.

First, we obtain the resonance frequency of the nanoslits using the spectral centroid method for each temperature [138]. In general, one would assume the asymmetry factor to be temperature-dependent, as the plasmon resonance is tempe- rature-dependent due to a change of the effective refractive index with temperature [86, 91, 127, 139]. However, this shift is very small, which allows us to assume the asymmetry parameter of the Fano profile q to be constant.

The validity of assumptions described above needs to be tested by assuming strongly varying asymmetry factors. Therefore we start with a centroid fit of the spectrum measured at the room temperature, before heating, and obtain $\omega_{res} = 1631.3\ \mathrm{cm}^{-1}$.

From the reference measurements depicted in fig. 4.2, we obtained $\omega_{vib} = 1644\ cm^{-1}$ and $\Gamma_{vib} = 35\ cm^{-1}$. A Lorentzian fit of the measured spectrum at room temperature provided parameters $A = 0.5$ and $\Gamma_{res} = 118\ cm^{-1}$. Thus, we perform fitting of the measured spectra at room temperature having fixed all obtained parameters, which allow us to find initial values $q = 0.30$ and $I = 0.46$.

It is crucial to check whether slight changes of the asymmetry factor q or ω_{res} result in changes of spectra similar to variation of I. Therefore, we tune the parameters around the values obtained and plot the first derivative of analytical results (fig. 4.10). We performed a centroid fit of the spectra for all temperature steps and obtained ω_{res} between $1631.3\ cm^{-1}$ and $1638.5\ cm^{-1}$. Thus, we plot results of the analytical model for values around this range (fig. 4.10 **a**). The red shift of ω_{res} does not explain our experimental findings.

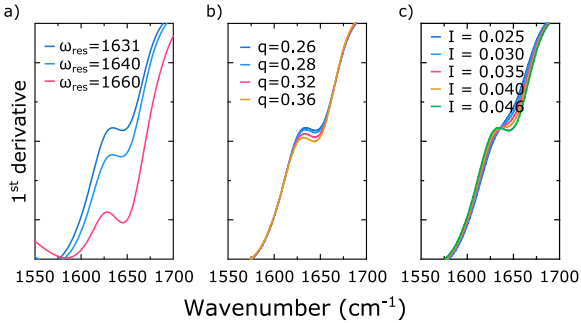

Figure 4.10: Influence of parameter variation on the results of our analytical model. Derivative of analytical reflectance spectra obtained for different (**a**) plasmon resonance frequency, (**b**) Fano asymmetry factor, (**c**) Fano amplitude. The ranges for ω_{res} and q variation are taken from the experimentally observed red shift of plasmon resonance due to heating. The variation of the Fano amplitude is the only parameter which allows our model to fit the measurements.

Therefore, we try to explain the experimental observation by changing the q parameter. We vary it around value of 0.30, as shown in fig. 4.10 **b**. Here, the model also has no agreement with the measured spectra.

In contrast, the variation of the Fano amplitude I can explain the measurements (fig. 4.10 **c**), whereas variation of q and ω_{res} could not. Thus, the introduced analytical model can be used for the data analysis.

Thus, we have obtained the q parameter from the fit of the first spectrum. Also, the rest of the parameters mentioned are obtained and fixed, because they are the same for all spectra. Finally, there is one parameter left, namely, I, which is related to the intensity of molecular vibration. Therefore, we perform fitting of each experimental spectrum with a single open parameter in the vicinity of the nanoslit resonance (fig. 4.9, color-coded dash curves).

As we introduced this model in order to extract the molecular vibrations, we normalize the analytically obtained amide vibration to the antenna profile and plot the resulting signal versus temperature (fig. 4.11, light green). This delivers a scalar value that describes the strength of the vibrational signal. This result demonstrates a reversible conformational change of the collagen-peptide monolayer under external stimuli. Similar to the bulk solutions, heating the D_2O surroundings of the molecules adsorbed on the gold surface induces structural changes in expected fashion.

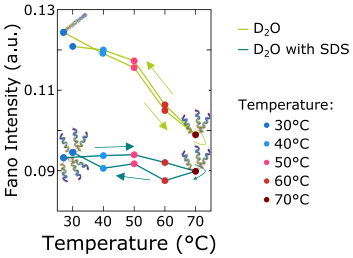

Figure 4.11: We extracted the intensity of molecular vibration by fitting a Fano profile to the measured spectra. After a temperature increase of the D_2O environment, the vibrational feature decreases in a sigmoidal manner (light green curve). However, in the control experiment, the SDS surrounding prevents this behavior (dark green curve), which is expected as molecules were denaturated at room temperature already.

As a control experiment, we performed the same temperature-induced measurements and data analysis for SDS-based surroundings (fig. 4.12). Here, we expected the molecules to be denaturated from the beginning, and thus, additional heating should have no effect (fig. 4.11, dark green). As expected, the SDS environment denaturates the peptides and additional heating causes no structural changes.

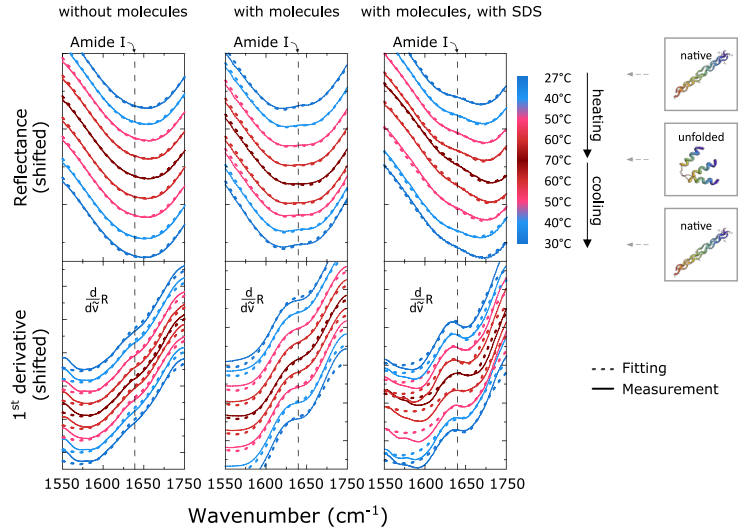

Figure 4.12: Heating the array of 1.7 µm long slits in aqueous environment. First, the nanostructures are without a monolayer of collagen-peptide. Afterwards, we perform heating of the covered sample in D_2O solution and continue with heating in an SDS environment. The measured spectra and their first derivative (solid curves) were fitted by the analytical model introduced above (dashed curves).

Our measurements and analytical analysis clearly validate our approach of in-vitro monitoring of structural changes of collagen molecules at low concentrations utilizing resonant surface-enhanced infrared spectroscopy with plasmonic nanoslits. Our concept allows for the observation of conformational changes under different stimuli, including temperature change. A detailed analytical analysis reveals the conformational transition from one secondary structure to another.

To further check the reliability of our concept, we performed similar measurements using different slit length, e.g. 1.8 µm long (fig. 4.13 **a**). Here, a similar behavior was detected even though the overall signal strength is weaker (fig. 4.13 **b**), as we discussed above.

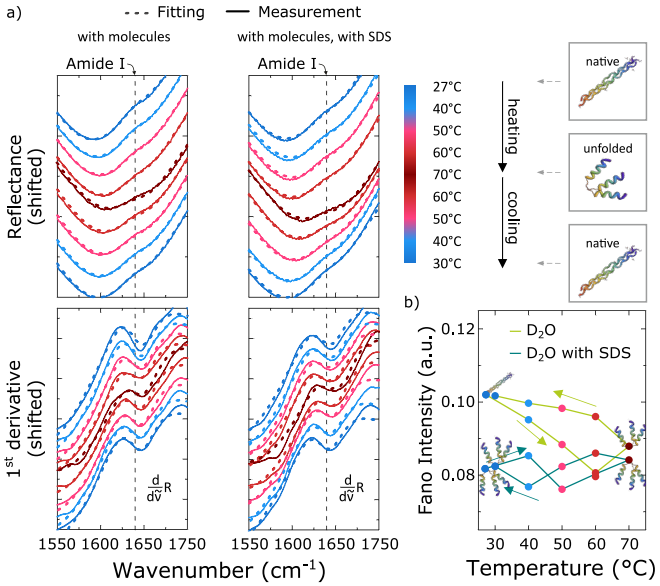

Figure 4.13: Heating of 1.8 µm long slits in aqueous surrounding. We perform the heating cycle of a sample being immersed in D_2O surrounding first (**a**, left) and after SDS environment (**a**, right). We use the analytical model introduced above to fit the experimental data (**b**). Here the molecular signal strength is lower due to the less perfect overlap of molecular and plasmonic excitation.

To summarize, we experimentally demonstrated the unique capabilities for ultrasensitive in-vitro detection of the triple-helical structure of collagen-like molecules at the monolayer scale utilizing mid-IR resonant plasmonic nanoslits as a sensing platform. As a result of the larger average SEIRA signal of inverse nanostructures, nanoslits are well suited to detect the structure of mini-collagens as well as other proteins. Our biosensor enables reliable tracking of collagen conformational changes under various exter-

nal stimuli via monitoring the amide I vibration. The analysis of our experimental data with a simple analytical model also reveals the expected folding behavior.

5

Monitoring folding of polypeptide monolayer

This chapter is based on the following publication [124]:

R. Semenyshyn, M. Hentschel, C. Stanglmair, T. Teutsch, C. Tarin, C. Pacholski, H. Giessen, and F. Neubrech, *"In-vitro monitoring conformational changes of polypeptide monolayers using infrared plasmonic nanoantennas"*,
Nano Letters 19, 1 (2018).

In the previous chapter we demonstrated a SEIRA-based concept for monitoring the secondary structures of collagen-peptides. This ultra-sensitive approach has significant limitations, namely, molecules should be not larger than slit width, in order to match the size of the "hot spots" of the nanostructure. Another weak point is the functionalization of the gold surface. Synthesized molecules with a thiol group are perfect for the concept validation, but one would need a chemical recipe which allows for binding of any biomolecules in order to bring this approach to real-world applications.

In this chapter, we report the application of resonant surface enhanced infrared absorption spectroscopy for in-vitro monitoring of structural changes of a molecular monolayer of polypeptides, here poly-L-lysine (PLL) [140]. PLL has been chosen for two reasons: On the one hand, it is a widely used polypeptide in biological applications, such as the functionalization of surfaces or sensors. On the other hand, poly-l-lysine can be well controlled and functionalized, which are crucial prerequisites in our experimental scheme.

Figure 5.1 illustrates the basic idea. Standard Fourier-transform (FT)-IR spectroscopy is used to probe the optical response of reso-

nant plasmonic nanoantennas in inverse reflection geometry. The antennas are immersed in an aqueous environment with the help of reflection fluidic cell (fig. 3.11), similar to the approach utilized in the previous chapter.

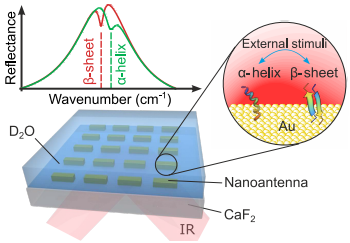

Figure 5.1: Chip-level based SEIRA for in vitro monitoring of conformational changes of polypeptides. A monolayer of poly-L-lysine (PLL) as a model system for polypeptides is immobilized in the plasmonic hotspots of gold (Au) nanoantennas. The amide vibration of PLL is enhanced if the plasmon is resonantly matched to the molecular vibration. By adding external stimuli, the secondary structure can be reversibly changed from the α to the β state resulting in different substructures of the amide vibration. The experiments are performed in aqueous solution.

As already mentioned in chapter 4, rod antenna arrays were already successfully used for monitoring protein dynamics in air as well as liquids. These experiments gave detailed information about the near-field distribution of light fields around the nanoantennas and their interaction with the vibrational resonances of the molecules [20, 22, 26].

Although nanoantennas provide less near-field enhancement compared to nanoslits [67], they allow to investigate larger molecules. Therefore, we optimize the nanoantenna design, as discussed later, in order to achieve the maximum of SEIRA enhancement.

Here we aim to in-vitro monitoring of reversible conformational changes, namely, the cyclic transition from one conformation to another and back, of a single molecular monolayer.

Functionalization chemistry is used to cover the gold surface with PLL molecules. The parameters may be potentially adjusted to dress nanoantennas with theoretically any protein. The used

PLL is 15-30 kDa in weight (CAS number 26124-78-7, Sigma Aldrich GmbH).

In these studies, chemical stimuli are used to switch the secondary structures of polypeptides (α-helix or β-sheet state) and thus leave the system in a defined state. During the transition, the defined and known states are then optically probed, allowing us to monitor the induced conformational changes. The recorded optical spectra will thus display the characteristic vibrational features of the two specific conformations (i.e., the substructure of the amide vibrations), allowing us to determine the secondary structure from the optical response alone.

5.1 REFERENCE MEASUREMENT AND SETUP

Poly-L-lysine is a water-soluble polypeptide composed of naturally occurring L-lysine, which contains amine groups on the side chains. PLL can be found in three distinct conformations, α-helix, β-sheet, and random coil (as well as mixtures) [141]. The secondary structure is determined by the external environment (e.g., solvents and temperatures) and can thus be switched at will, an important prerequisite for our experiments. It has been shown that conformational transitions can be induced by various external stimuli, including heat [17], pH [108, 142–144], alcohol [143], solvents [145], and surfactants [136, 146].

In contrast to previous studies, we strive to observe the folding and unfolding of PLL, ideally the cyclic transition between α-helix and β-sheet states. Consequently, not all of the aforementioned stimuli are suitable as in some cases the stimulation causes permanent denaturation. Therefore, we focus on folding-unfolding of PLL induced by surfactants, namely sodium dodecyl sulfate (SDS) as well as by variation of the external basicity level. The recipe of SDS solution we used was introduced previously in the literature [136].

As mentioned above, molecules exhibit characteristic vibrational spectra in the IR spectral range. In our case, the amide I band resulting from backbone vibrations [83], will be monitored

to assign the secondary structures to poly-L-lysine. In the α-helical conformation the amide vibration peaks at 1644 cm^{-1} and at 1618 cm^{-1} in the β-sheet state [16]. As H_2O exhibits vibrational fingerprints in the amide I spectral range, we utilized D_2O featuring vibrational features at lower energies as a solvent in order to circumvent this parasitic H_2O absorption. We are therefore not tuning the pH level but rather the pD levels. To reduce the D_2O absorption in our experiments, a specially designed transmittance flow cell (fig. 3.12) and an inverse reflection setup (fig. 3.11) probing µL volumes of solution were used. All IR spectra were taken in transmission (bulk solution) or inverse reflection geometry (SEIRA measurements) with a standard FTIR microscope on specifically designed resonant plasmonic nanoantenna arrays (see the chapter 3.4).

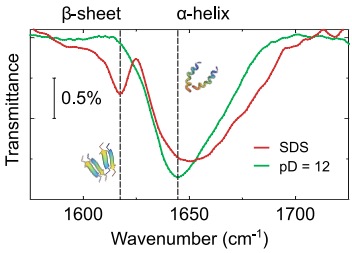

Figure 5.2: IR optical properties of the poly-L-lysine model system. Relative transmittance spectra of poly-L-lysine in bulk solution (D_2O). The amide I vibration reveals the secondary structure of PLL. Depending on external stimuli (SDS or basicity) the polypeptide is either in the α-helical state (1644 cm^{-1}) or the β-sheet state 1618 cm^{-1}.

As a first step, we characterized the utilized poly-L-lysine and its properties (fig. 5.2), by measuring transmittance spectra of highly concentrated aqueous solutions of PLL. The green curve shows the response of 5 mmol PLL in D_2O at a pD level of 12, whereas the red curve shows PLL at the same concentration in an SDS-D_2O solution at $pD = 7$. As expected, the spectra reveal the secondary structure of the polypeptide. At high basicity the vibrational signal of the α-helical state at around 1644 cm^{-1} is observed while no signal near 1618 cm^{-1} can be identified, indi-

cating a near-unity α-helical state of the polypeptides. In contrast, the polypeptides in an SDS solution show a distinct and strong response at 1618 cm^{-1} indicative of the β-sheet conformation. These solution-based measurements show that we are able to set the conformational state of our model system poly-L-lysine.

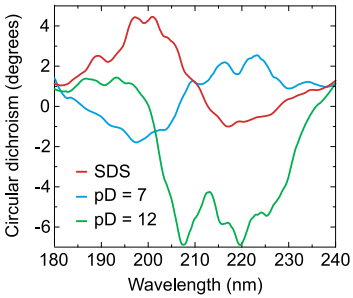

Figure 5.3: Circular dichroism (CD) of PLL in different chemical surroundings. A random mixture of α-helix to β-sheet in D_2O with a pD value of 7 (blue curve) is found. Changing the pD value to pD 12 forces the transition to the α-helical state (green curve). If SDS is added, the polypeptides change to the β-sheet state (red curve). The PLL concentration was 0.25 mg mL^{-1} and the optical path for CD measurements was 0.2 mm.

Also, we perform another reference measurement. Here, we utilized the solution of PLL performing CD measurements (fig. 5.3). We diluted 0.25 mg L^{-1} and filled 0.2 mm thick cuvette with this solution. The CD spectra are in good agreement with the literature [147] and reveal that our used PLL molecules undergo structural transitions.

5.2 ANTENNA FUNCTIONALIZATION

As we are going to enhance the vibrational signal utilizing resonant plasmonic nanoantennas we need to controllably place the polypeptides inside the local electric field around the nanostructures. This task is accomplished by a functionalization scheme, which is sketched in fig. 5.4. Two points are of great importance: On the one hand, the polypeptides need to be attached to the antennas close enough to the surface as to interact with the local

electric field [30, 93]. On the other hand, the polypeptides need to be at distance from the surface as well as from their neighboring polypeptides large enough to be able to undergo the desired structural transitions [108].

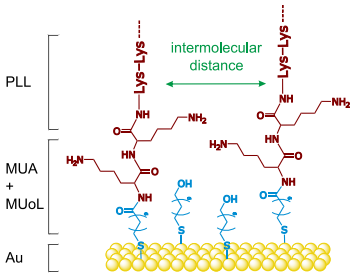

Figure 5.4: Functionalization scheme. PLL molecules are immobilized on a gold surface using a mixed monolayer of MUA and MUoL. The intermolecular distance between PLL molecules, which can be adjusted by the composition of MUA/MUoL, and their distance to the gold surface are crucial for conformational changes.

We use two types of thiols, 11-mercaptoundecanoic acid (MUA) and 11-mercaptoundecanol (MUoL) for the antenna functionalization. These bind to the gold antennas and not the surrounding CaF_2 and provide the required larger surface-polypeptide-distance as well as the lateral spacing. To predispose the carboxyl group of MUA for the binding to the poly-L-lysine an EDC/NHSS solution in MES buffer is used. For further details, please refer to the chapter 3.3.2 and ref [108], where the recipe is introduced and the role of MUoL is discussed as well.

The gold nanoantenna arrays (100 $\mu m \times 100\ \mu m$) were produced by standard electron beam lithography in a positive tone resist (PMMA) via lift-off. Such top-down techniques offer the possibility to tailor the geometry and properties of the antennas nearly at will and as such optimize their performance according to the needs of our experiment (more detailes are in chapter 3.2.1). A number of issues are important here, namely, the strength of the local field enhancement and the Rayleigh anomalies [30], as well as the geometrical access of the polypeptides to the nanoan-

tennas, i.e., the spacing and gap size between adjacent nanostructures [148]. Taking into account these points, we varied the length of the nanoantennas between 1350 and 1750 nm with a lateral spacing constant of 200 nm in the x-direction (along the long antenna axis) and a period of 3300 nm in the y-direction (along the short antenna axis). The antennas width and height are fixed at 100 nm. Titanium was used as an adhesion layer on the IR transparent CaF_2 substrates due to its chemical stability at large pD levels.

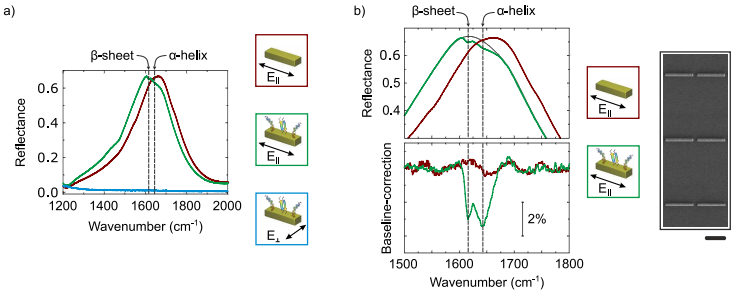

Figure 5.5: Functionalization of nanoantennas. Reflectance spectra (averaged 50 spectra) of resonant nanoantenna arrays in D_2O are taken before (red) and after (green) functionalization with MUA/MUoL and poly-L-lysine (see illustrations). (**a**) The resonance frequency is shifted due to the accumulation of polypeptides on the antenna surface. Depending on the polarization a strong plasmonic response is observed (see illustrations). (**b**) A close-up view shows the amide I vibration enhanced by the plasmonic nearfields (upper panel). A baseline correction delivers the vibrational signatures of PLL in the α-helical and β-sheet state (lower panel). No vibrational modes are found prior to functionalization (red) and for illumination with perpendicular polarized light (light blue). The SEM image depicts an exemplary antenna array; the scale bar is 1 µm.

Figure 5.5 depicts the measured spectra of one exemplary nanoantenna array with an antenna length of 1500 nm acquired in an inverse reflection geometry. The red curve shows the response of the unfunctionalized antenna array inside the flow cell filled with D_2O. A pronounced plasmonic resonance can be observed for light polarized along the antenna axis at about 1650 cm^{-1}, nearly perfectly match-ed to the energies of the vibrational modes which are expected at 1644 cm^{-1} and 1618 cm^{-1}.

As one can see, after the functionalization with MUA/ MUoL and poly-L-lysine, the sample was rinsed and placed in the flow cell filled with D_2O. It is important to note that during this process the sample is always in aqueous environment. We observe two distinct differences: The plasmonic resonance undergoes a spectral red-shift which is caused by the larger effective refractive index of the surrounding [132] due to the deposition of the functionalization layer and poly-L-lysine (fig. 5.5 **a**). In order to extract the enhanced vibrational signal strength, which is a measure of the number of polypeptides in a certain conformation, we need to perform a baseline correction (fig. 5.5 **b**). The baseline characterizes the plasmonic response in the absence of the vibrational modes and is calculated from the coupled system using an adapted version of the asymmetric least-squares smoothing algorithm proposed by Eilers [121] and is shown in black. Normalization of this baseline to the measured spectra delivers the so-called baseline-corrected vibrational spectra.

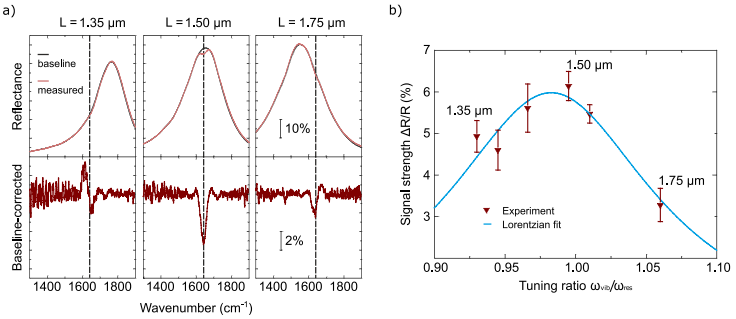

Figure 5.6: Optimization of the SEIRA enhancement. (**a**) Reflectance spectra of nanoantennas covered with PLL in the α-helical state (upper panels). Depending on the antenna length L, the ratio between the plasmonic resonance ω_{res} and the amide vibration ($\omega_{vib} = 1644\ cm^{-1}$, indicated by dashed lines) changes. This results in vibrational signals of different strengths and line shapes (Fano-profile) as seen in the baseline-corrected spectra (lower panels). (**b**) Enhanced vibrational signal versus tuning ratio. The SEIRA enhancement is maximum if the plasmonic excitation is resonantly roughly matched to the molecular vibration ($\omega_{res}/\omega_{vib} \approx 1$). As a guide to the eye, a Lorentzian was fitted to the measured data (blue curve). The corresponding antenna length ($L = 1.5\ \mu m$) is selected for the in-vitro monitoring experiments.

In fact, the array with 1500 nm long antennas is selected after an optimization procedure. We measured all functionalized antenna arrays, which were produced on the substrate (fig. 5.6). Figure 5.6 **a** depicts reflection spectra (three upper panels) of three nanoantenna arrays: the shortest, the optimal, and the longest ones. The lower panel shows the baseline-corrected spectra in order to illustrate different signal enhancement. Figure 5.6 **b** presents a comparison of SEIRA enhancement for all the arrays measured. As a result of this optimization, we select the array of 1500 nm long nanoantennas as the most promising one. However, to verify our main results, we perform all the measurements with other arrays as well.

5.3 MONITORING PLL CONFORMATIONAL CHANGES

Figure 5.7 depicts our main findings and shows the cyclic folding and unfolding of a single monolayer of poly-L-lysine under external chemical stimuli. The upper row shows a sketch of the nanoantenna as well as the conformation of the polypeptides. Again, it is important to stress that we are able to reliably and controllably set the conformation of the polypeptides by an external stimulus. This information serves as a benchmark for the vibrational fingerprints we are retrieving from our measurements. The baseline-corrected vibrational features, which are imprinted on the spectrum of the functionalized antennas, are displayed in the bottom row.

Panel (**a**) of fig. 5.7 shows the response right after functionalization. As discussed earlier, the polypeptides are now in a random distribution of α-helical and β-sheet states. The measured spectra reflect this known behavior. The baseline-corrected spectrum exhibits the vibrational signatures of the of α-helical and β-sheet states at 1644 and 1618 cm^{-1}, respectively. We now perform a pD-jump from 7 to 12 which is known to force the polypeptides into the α-helical state [17], shown in panel (**b**). As expected, the signature of the β-sheet state vanishes from the vibrational spectrum, clearly showing a near-unity α-helical state distribu-

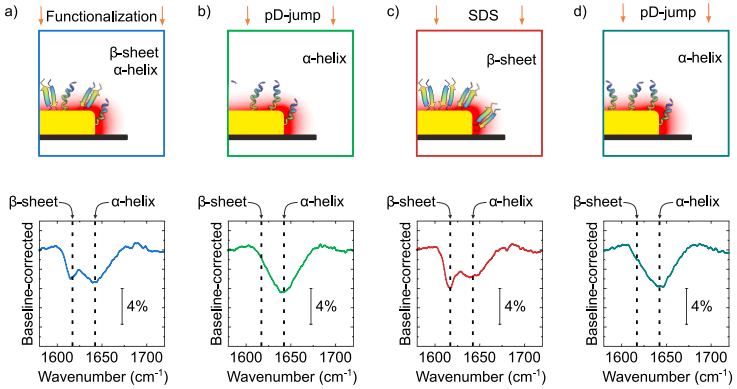

Figure 5.7: In-vitro monitoring of PLL conformational changes. Baseline-corrected SEIRA signals (bottom) of nanoantennas functionalized with PLL under different external stimuli. (**a**) After functionalization, PLL molecules are in a random mixture of α-helix to β-sheet as evidenced by the vibrational substructure of the amide band. (**b**) If the basicity is increased to a pD-value of 12, the vibrational signature of the β-sheet state ($1618\ cm^{-1}$) vanishes, and only the α-helix ($1644\ cm^{-1}$) signature remains. (**c**) SDS forces a transition of the polypeptides back to the β-sheet state. (**d**) A second increase in basicity (pD of 12) switches the vast majority of molecules back to the α-helix state. The vertical dashed lines indicate amide vibration of α-helix and β-sheet states.

tion. We now exchange the solution in our flow cell with an SDS solution which switches the poly-L-lysine to the β-sheet conformational state, depicted in panel (**c**). In the vibrational spectrum we observe the reappearance of the β-sheet vibrational feature at $1618\ cm^{-1}$. However, the fingerprint at $1644\ cm^{-1}$ associated with the α-helical state remains, yet significantly weaker.

This result indicates that only part of the polypeptides folds back into the β-sheet state, while some remain in the α-helical conformation, as seen in ensemble measurements (fig. 5.2). A further and final pD-jump should again force all polypeptides in the β-sheet state back to the α-helical one. The vibrational spectrum shown in panel (**d**) now indeed exhibits the mode solely at $1644\ cm^{-1}$ indicating again a near-unity α-helical state distribution.

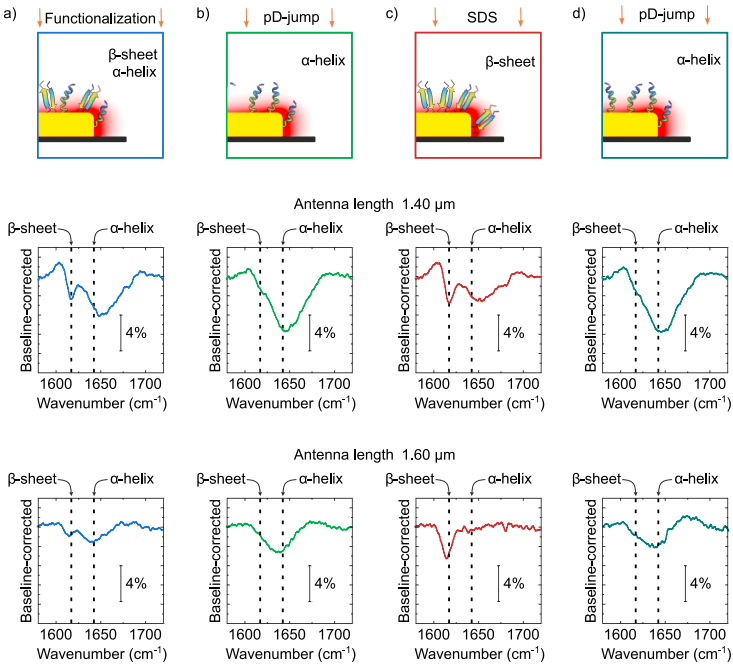

Figure 5.8: Monitoring structural changes of PLL utilizing different antenna arrays. Baseline-corrected SEIRA signals of nanoantennas with different lengths (middle – 1.4 µm, bottom – 1.6 µm). Structures were functionalized with PLL measured under different external stimuli, similar to fig. 5.7: (**a**) After functionalization. (**b**) The basicity is increased to a pD value of 12. (**c**) SDS forces a transition of the polypeptides back to the β-sheet state. (**d**) A second increase in basicity (pD of 12) switches the vast majority of molecules back to the α-helix state. The vertical dashed lines indicate the amide I vibration of PLL in the α-helix and β-sheet states.

As mentioned above, we perform the same measurements for the antenna arrays with different length, which proves the reliability of our sensor (fig. 5.8).

To quantify the performance of our approach, we estimated the number of molecules contributing to the enhanced fingerprints, which are located in the area of the nanoantenna tip ends [72]. Based on this and on the assumption of a spherical PLL molecule with a diameter of roughly (close packing) 4 nm [80, 140], we

estimate the number to be about 1600 PLL molecules per antenna which contribute to the enhanced signal.

5.4 PCA OF PLL CONFORMATIONAL CHANGES

In order to further analyze the data and to support our interpretation without performing a baseline correction, we applied principal component analysis (PCA) on the raw data, which contain 200 individual spectra in total (50 for each external stimulus). PCA is a common method in multivariate statistics, which extracts the correlation of data points by applying a principal axis transformation such that the variance of the data sets becomes maximum [123]. Appropriate calibration measurements even allow extracting concentration ratios [149].

Applying PCA to our data (see chapter 3.5.3), we can express each spectrum i ($i \in [1, 200]$):

$$\mathrm{Spectrum}_i = A + \sum_{j=1}^{200} \left(k_{i,j} \cdot \mathrm{PC}_j\right)$$

where A is the average taken over all 200 spectra. The principal components PC_j are therefore so-called correction spectra to the average experimental spectrum. The principal components are the same for all 200 experimental spectra, whereas the weighting coefficients $k_{i,j}$, also called scores of principal component j, are related to the spectrum i.

PCA can be understood in an intuitive way: We are looking for a basis set of fundamental functions such that all 200 spectra can be expressed as linear combinations of these fundamental functions, the so-called principal components. As a basis set, the principal components are unique for the entire set and are spectra in our particular case. If there were no correlation between the 200 spectra, the PCA analysis would require 200 unique and independent principal components in order to describe all experimental spectra. Likewise, for large correlations only very few principal components are needed to express all measured spectra.

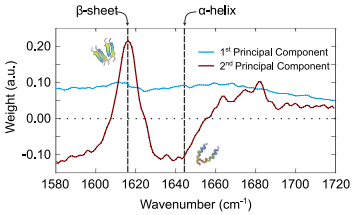

Figure 5.9: Principal component analysis (PCA) of PLL structural changes, the first and second principal components. The first PC resembles intensity changes of the resonantly scattered light. The second PC represents the changes of molecular vibration under the external chemical stimuli. Thus, most of the variability of each spectrum can be accounted for by a linear combination of the first and second principal components with scores.

For PCA, the assumption of strong correlations is best justified if the sum given in the equation above terminates after only a few corrections or principal components. One can calculate the impact of each principal component by the overall accuracy of the representation of the measured spectrum by the PCA basis set after the corresponding order. In our case, the 1^{st} principal component has an impact of 82.3 %, the 2^{nd} principal component 6.4 %, the 3^{rd} 0.6 %, the 4^{th} 0.5 %, and the 5^{th} 0.5 %. This means that the 1^{st} and 2^{nd} principal components (fig. 5.9) hold the main information about the differences in the dataset (between 200 individual spectra). It also implies that our assumption of strong correlations between the measured spectra is well satisfied.

Figure 5.9 depicts the first and the second principal components. The first principal component, interestingly, exhibits hardly any spectral features but is nearly flat over the entire spectral range. When inspecting the different measured spectra we observe a clear intensity drift in the magnitude of the plasmon resonance (see fig. 5.10). This drift is linked to experimental challenges in stabilizing the setup over hours of data acquisition. We thus conclude that the first principal component captures this drift and only shifts the absolute value of the spectra. Therefore, it does not contain any information about the protein folding dynamics.

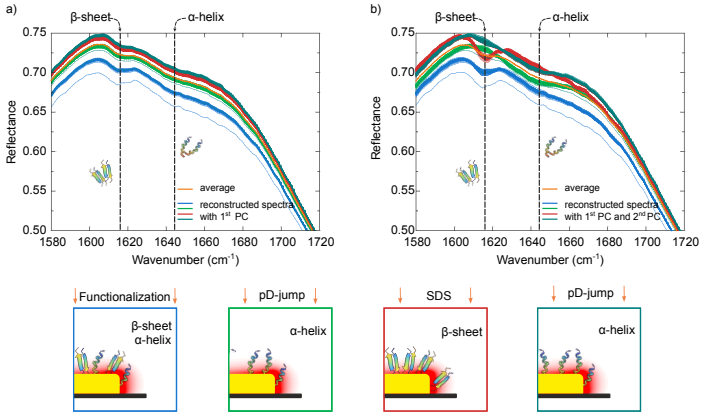

Figure 5.10: Reconstruction of spectra using principal components. (**a**) Spectra reconstructed using the 1^{st} principal component (PC) only. No information on the folding is obtained. Only a drift of the spectra caused by experimental instabilities is seen. (**b**) Reconstructed spectra using 1^{st} and 2^{nd} principal components provide information on protein folding. No higher principal components are needed.

The second PC on the other hand exhibits pronounced spectral features, most notably at the vibrational frequencies of the α-helix and β-sheet states at 1644 cm^{-1} and 1618 cm^{-1}, respectively. On first sight, it is counterintuitive that both features are present in this component. However, one has to keep in mind that this component is a correction term to the shifted average experimental spectrum and is the same for all experimental spectra; only the scores will be different. As the average spectrum has both features for the α-helical and β-sheet states, the scores of PC_2 for each spectrum correct the average according to the secondary structure of the PLL for the corresponding measurement step. The fact that PC_2 has two features of opposite sign underlines this interpretation. For example, to reconstruct the spectrum of the α-helical state the average needs to be corrected by PC_2 with positive score and with negative score for a predominantly β-sheet state. We thus conclude that the second PC and its scores contain the information about the secondary structure

of the molecules. Therefore, the scores of PC_2 can be used to cluster the data to different conformational states.

In order to depict the results of all 200 experimentally obtained spectra, we plot the scores of PC_1 and PC_2 in fig. 5.11 against one another. The data points are color-coded according to the four distinct data sets of 50 spectra each. The four measurement sets can be clearly distinguished in the plot as they form strongly correlated and non-overlapping clusters.

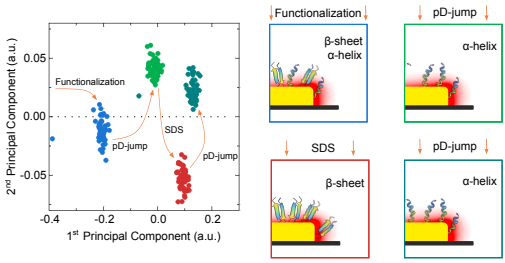

Figure 5.11: Principal component analysis (PCA) of PLL structural changes, the scores of first and second principal components in two-dimensional space. This presentation depicts the clustering of the data set and thus represents the different conformational states of PLL. Particularly, the clusters 2 and 4 (light and dark green) are the one group attributed to α-helix, whereas the third cluster is the group attributed to the β-sheet state, and first – a mixture of both α-helix and β-sheet.

Directly after functionalization, the spectra are characterized by scores of PC_2 around zero, indicating that both conformational states of the molecules are present. After the first pD-jump the scores of PC_2 are strongly positive, which indicates that the polypeptides have undergone a structural change to a near unity α-helix state distribution. Addition of SDS leads to spectra which are characterized by strongly negative scores of PC_2. This behavior implies that a clear structural transition from the α-helix to the β-sheet state occurred. After the final pD-jump the spectra are again characterized by positive scores of PC_2, indicative of predominantly α-helix state distribution. The α-helix and β-sheet state distributions are very well separated and can

be clearly distinguished. The two α-helix state distributions are very similar, yet not identical with respect to their score values. As mentioned above, we ascribe these differences to incomplete structural transitions between the different states which lead to different distributions.

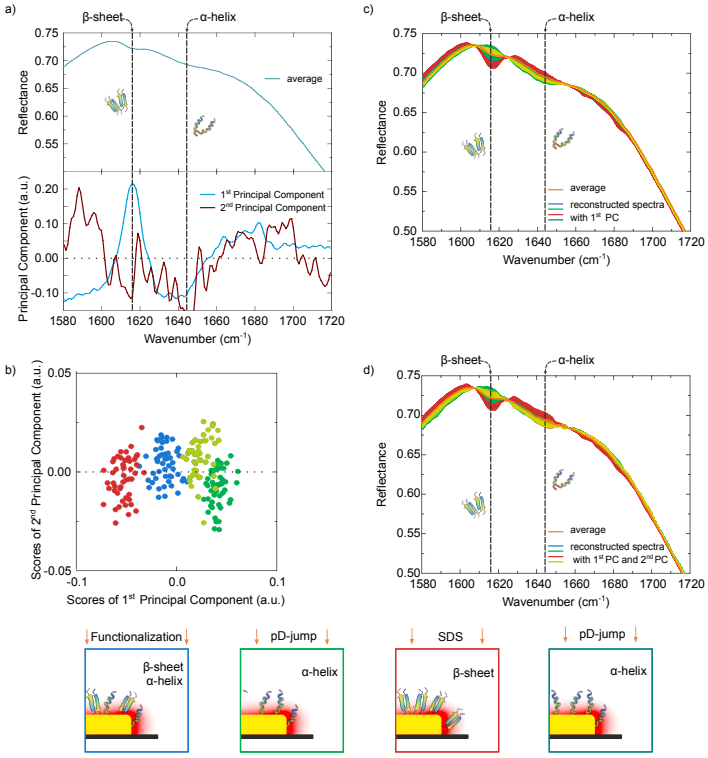

Figure 5.12: Reconstruction of preprocessed spectra using principal components. Similar to the fig. 5.10, we performed PCA on the dataset. However, the spectra were preprocessed this time in order to remove the intensity drift from the spectra. (**a**) We find that now the 1^{st} PC holds the vibrational information. (**b**) Consequently, the scores of both 1^{st} and 2^{nd} PCs look different. (**c**) Using only the 1^{st} principal component, one can reconstruct the spectra. (**d**) Adding the 2^{nd} PCs does not add additional physical information, as expected. Thus, it is clear the score in (**b**) are nicely clusterized by the 1^{st} component.

As discussed earlier, the scores of PC_1 do most likely not contain information about the folding dynamics. However, even when disregarding this value, the data points still form distinct clusters well separated along the respective $k_{i,2}$ value distribution.

To verify the statement that PC_1 does not contain information about polypeptide dynamics, one could perform preprocessing of the dataset in order to suppress the drifts of the antenna array resonance. This means that we shift spectra such that from 1680 cm^{-1} up to 1720 cm^{-1} all resonance profiles match. Thus, one would expect the new 1^{st} PC to represent the secondary structure changes. In order to check this, we preprocessed each spectrum so that antenna profile was as close as possible to the average spectra. This precorrected data was used for PCA (fig. 5.12).

The measurements shown in fig. 5.7 and principal component analysis depicted in fig. 5.11 thus very clearly validate our concept of in-vitro monitoring of the conformational changes of polypeptide monolayers using resonant surface enhanced infrared spectroscopy with plasmonic nanoantennas. We can reliably track the conformational changes of a monolayer of poly-L-lysine bound to the surface of resonant nanoantennas. Our results of PCA also reveal that the expected full conversion between the two conformational states does not take place and part of the molecules remain in the α-helical state, while others are pushed into the β-sheet conformation, which is in fact a testament to our analysis technique.

Thus, we have demonstrated in-vitro observation and tracking of conformational changes of a PLL monolayer with the help of resonant surface-enhanced infrared absorption spectroscopy and principal component analysis.

6

Pushing the detection limit: single nanoantenna

This chapter is based on the following publication [150]:

R. Semenyshyn, F. Mörz, M. Ubl, M. Hentschel, F. Neubrech, and H. Giessen, *"Pushing down the limit : In-vitro detection of a polypeptide monolayer on a single infrared resonant nanoantenna"*, ACS Photonics, submitted (2019).

Previous experiments have demonstrated that resonant plasmonic nanoslits and nanoantennas are reliable sensing platforms to monitor protein dynamics. To follow up this approach, a single nanoantenna may be explored for in-vitro investigation of the protein conformation with minimal sample concentrations and volumes.

Reaching the single-molecule level by exploiting plasmonic enhancement has been demonstrated in Raman spectroscopy [24], but has not been achieved in FTIR spectroscopy yet. Recent publications as well as our results demonstrate the high potential of this approach. Despite a significant increase of measurement sensitivity, the amount of detected molecules on the plasmonic nanoarrays is still on the order of hundreds of thousands.

The sensitivity can be further improved by using synchrotron light sources, which exhibit orders of magnitude higher brilliance [114, 151, 152], but at the expense of limited availability, accessibility, and high costs.

In contrast to these far-field techniques, one can use atomic force (AFM) [9] or scanning near-field optical (SNOM) [10, 153, 154] microscopy to detect vibrations on the level of a few proteins. However, these approaches impede in-vitro measurements.

The key element to further enhance the measurement sensitivity is the application of a mid-IR light source, which exhibits a brilliance that exceeds that of synchrotrons and which has good beam quality as well as a high coherence to enable efficient sample illumination. Furthermore, a single source is required, whose bandwidth is sufficiently broad to detect all the desired molecular vibrations at once, avoiding the necessity for spectral sweeping. Light sources that can match these requirements are mid-IR lasers with ultrashort and hence broadband pulses [117, 155, 156].

Therefore, we combined a highly brilliant, pulsed laser source and an individual plasmonic nanoantenna as an ultra-sensitive platform for tabletop protein studies at attomolar concentrations and attoliter volumes [20, 157].

6.1 REFERENCE MEASUREMENTS

Our light source is based on tunable parametric frequency conversion, which covers a broad spectral tuning range from 1.33 to 8 µm (7500 - 1250 cm^{-1}). The laser pulses exhibit a bandwidth of about 125 cm^{-1} ($1/e^2$-width), which is sufficient to cover molecular amide I vibrations without frequency tuning. A detailed discussion can be found in [111, 112, 158, 159].

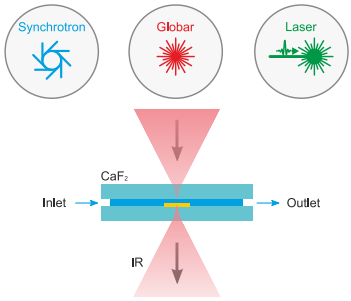

Figure 6.1: Schematic drawing of the experimental procedure and our setup. The conformation of a polypeptide monolayer on a single gold nanoantenna is investigated in-vitro, employing SEIRA and FTIR spectroscopy. To reach such a high sensitivity, we utilize a synchrotron light source for reference measurements and a tunable mid-IR laser in combination with a Globar for tabletop experiments.

We investigate in-vitro the conformation of polypeptide monolayers on single gold nanoantennas, exploiting the plasmonic signal enhancement of SEIRA. As control experiments, we additionally use a synchrotron and a Globar as light sources, which are also commonly used in FTIR spectroscopy. Figure 6.1 depicts the experimental procedure and our setup. For in-vitro measurements a microfluidic cell is used (see fig. 3.12), allowing transmission measurements and control of the liquid environment.

The measurement setup consists of a Bruker Vertex 80 FTIR spectrometer, which is attached to a Bruker Hyperion 2000 microscope (see chapter 3.4.1). During all experiments, we use a 36x condenser and objective for illuminating the measured sample area, which is limited to about $10 \times 10\ \mu m^2$ via the microscope aperture. Our FTIR setup includes a Globar and offers an external light source input, which we use for laser incoupling. We flush the setup with nitrogen to minimize atmospheric absorptions to a negligible extent. The measurements applying a synchrotron light source were conducted at the Swiss Light Source (SLS) at a similar Bruker FTIR microscope setup [116].

In contrast to the studies discussed in previous chapters, here we utilize a transmittance fluidic cell only (fig. 3.12) to perform in-vitro measurements. However, we still perform the PLL detection in D_2O-based surroundings.

The utilized gold nanoantennas differ in length to ensure the plasmonic resonance matches the polypeptide resonance for efficient near-field enhancement [89]. The antennas are about 100 nm in height and width, and between 1.7 and 1.9 µm long and placed on a CaF_2 substrate. The antenna length might vary between the presented measurements, due to the different samples.

As was performed in previous experiments, we utilize the same model system for the secondary structure analysis, namely poly-L-lysine (PLL) [108, 140, 160, 161]. As discussed in chapter 5, it exhibits different conformations and by analyzing the amide I vibrations, structural changes can be detected. Spectral features shift in frequency and differ in spectral shape as the conforma-

tion changes, due to the rearrangement of intramolecular bindings.

We again focus on the detection of the so-called α-helical and β-sheet PLL conformations, which exhibit resonance peaks at around 1648 cm^{-1} and 1618 cm^{-1} [108, 124], respectively. The molecules are functionalized using the same recipe as in the previous chapter [108]. The estimated number of molecules contributing to a plasmonically enhanced signal is 1600 for a single antenna [124], assuming that only molecules in the vicinity of the tip ends, where the near-field is highest, contribute to the polypeptide signal [72].

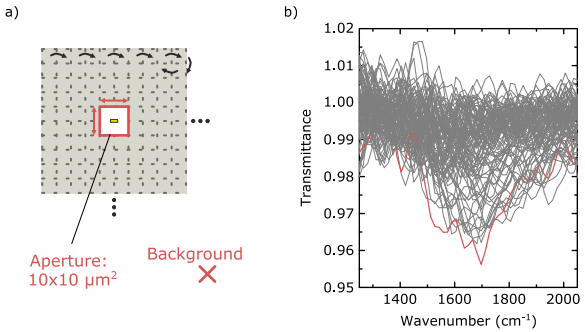

Figure 6.2: Mapping procedure of single nanoantennas. (**a**) Alignment of the sample in the microscope. An area of $20 \times 20\ \mu m^2$ is mapped in steps of 2 µm around the coarse antenna position. On each position an IR spectrum is measured. (**b**) The position at which the antenna signal is strongest, is defined as the measurement position. For all measurements, the background position is located on the bare CaF_2 substrate.

In order to measure a single nanoantenna, the sample needs to be carefully aligned in the microscope $10 \times 10\ \mu m^2$ (fig. 6.2). For coarse sample alignment, markers on the sample are used, but fine tuning is carried out by mapping the sample in order to find the maximum plasmonic antenna signal. The mapping is done by measuring a $20 \times 20\ \mu m^2$ area in steps of 2 µm at a resolution of 32 cm^{-1} using the Globar light source (fig. 6.2 **a**). 50 spectra are averaged per pixel. By evaluating the spectra, the position of maximum signal amplitude is found (fig. 6.2 **b**). This position

is defined as the measurement position for the presented Globar spectra. This procedure is carried out in a similar fashion for the laser and for the synchrotron light source.

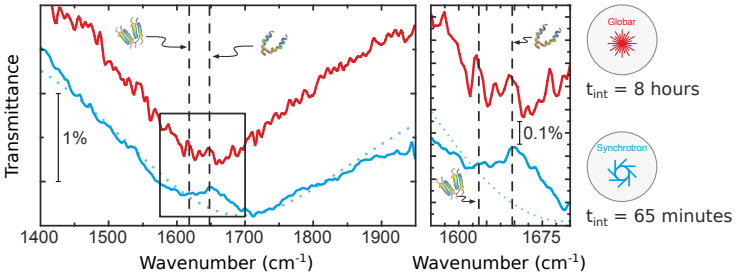

Figure 6.3: Comparison between synchrotron and Globar spectra of the polypeptide covered single antenna. A 1.80 µm long antenna is used for the synchrotron measurement, whereas a 1.75 µm long antenna is used for the Globar. The spectra are shifted in transmittance for better comparability and the bare profile of a 1.80 µm long antenna measured with the synchrotron is indicated with a short-dotted line. The inset (magnified at the right panel) gives a more detailed view on the region of interest. A distinct signal is observed with the synchrotron matching the α-helical resonance peak. The Globar noise is significantly higher due to its lower brilliance, and exceeds the expected signal. No β-sheet signal is observed in either case. The α-helical and β-sheet polypeptide resonances are indicated by vertical long-dashed lines at around 1648 and 1618 cm^{-1}.

To validate our sensing concept, we first perform broadband measurements using synchrotron and Globar light sources, which fully cover the plasmonic resonance of the functionalized antenna. Figure 6.3 depicts the recorded spectra of a 1.8 µm long antenna, covered with molecules (synchrotron measurement) and a slightly shorter antenna of 1.75 µm length (Globar measurement), exhibiting broad plasmonic resonances with center frequencies of about 1700 and 1650 cm^{-1}, respectively. A detailed view on the spectral region of interest is given next to the full spectra. The spectrum measured with the Globar clearly exhibits high noise, which exceeds any expected PLL signal. In contrast, the signal-to-noise ratio (SNR) of the synchrotron spectrum is significantly higher and a distinct resonance is found, despite half the measurement time of the Globar. For a better visibility of this feature, we indicate the bare antenna resonance with a short-dotted line. This

bare antenna profile is obtained by a Lorentzian fitting method (see eq. 4.2). As one can see, no signal is detected at the spectral position of β-sheet vibration and thus we conclude the PLL monolayer to be predominantly in the α-helical conformation.

6.2 TABLETOP MEASUREMENTS

To make this concept feasible for tabletop applications, we continue our studies utilizing a broadband laser light source. For further experiments, the laser is tuned to a center frequency of $1634\,\mathrm{cm}^{-1}$, which is in between the α-helical and β-sheet resonances. Figure 6.4 depicts a typical spectral intensity distribution, shown in grey, as an inset in the main figure. The semitransparent areas mark the spectral range which is not covered by the laser light. In this range the remaining laser intensity is too low to be detected and the FTIR spectra are dominated by noise. Only minor atmospheric absorptions are visible in consequence of nitrogen purging. Following fig. 6.3, we compare the measurement obtained with the laser to the synchrotron spectrum. We employ a 1.75 µm long antenna for the laser measurement, as we did using the Globar. The antenna profiles are fitted using a Lorentzian fit (see eq. 4.2) and are indicated as short-dotted lines.

Comparing the slopes of the synchrotron and laser spectra, the latter appears steeper, as well as blue-shifted. This is related to the slightly shorter antenna length and the different illumination geometries. Considering the different beam shapes and qualities of the light sources, a higher light intensity at the sample position, as well as a higher optical throughput is achieved with the laser, compared to synchrotron and Globar. This results in a significantly higher intensity reaching the detector, leading to a better SNR. It needs to be considered, that the plasmonic resonance can slightly shift, depending on the illumination of the antenna, i.e., plane wave or angled illumination [162].

On the right panel of fig. 6.4, a detailed view on the region of interest ($1/e^2$ laser bandwidth) is given. Here, the laser spectrum exhibits a distinct vibrational signal on top of the antenna profile,

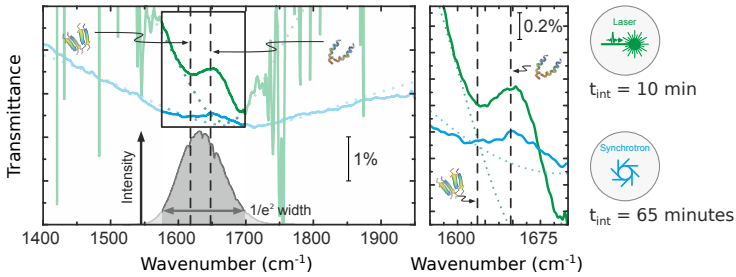

Figure 6.4: SEIRA using the synchrotron and laser. A typical laser intensity distribution is depicted in grey, measured in transmission through the bare CaF_2 substrate (background measurement). The $1/e^2$-bandwidth reaches $125\,cm^{-1}$, allowing both polypeptide conformations to be detected equally well. Note that the spectra are shifted in y-direction for better comparability. For a better visibility of the polypeptide resonances overlaying the antenna profiles, the bare antenna profiles are indicated as short-dotted lines. The right panel, which is the magnified inset from the left panel depicts a zoom-in view. Both spectra exhibit a distinct and similar resonance at $1648\,cm^{-1}$ on top of the antenna profile, which matches the α-helical amide I vibration. The laser exhibits a significantly higher signal strength after much smaller measurement time. The α-helical and β-sheet polypeptide resonances are indicated by vertical long-dashed lines at around 1648 and $1618\,cm^{-1}$.

which agrees well with the synchrotron measurement, however, with much better SNR. The signal fits the resonance of the α-helical amide I vibration well, whereas no signal at the expected β-sheet signal is observed. This indicates an α-helical conformation of the PLL monolayer.

Besides the better SNR compared to the synchrotron, the laser allows measurements within a much shorter measurement time. Here, spectra are accumulated for 10 min, although 2.5 min are sufficient to achieve a SNR comparable to the synchrotron spectrum, as shown in fig. 6.5 for two different individual antennas. We believe that fast measurements are of high importance and a tabletop setup is required to conduct research on a daily basis at moderate cost and effort, which is enabled with the presented laser approach.

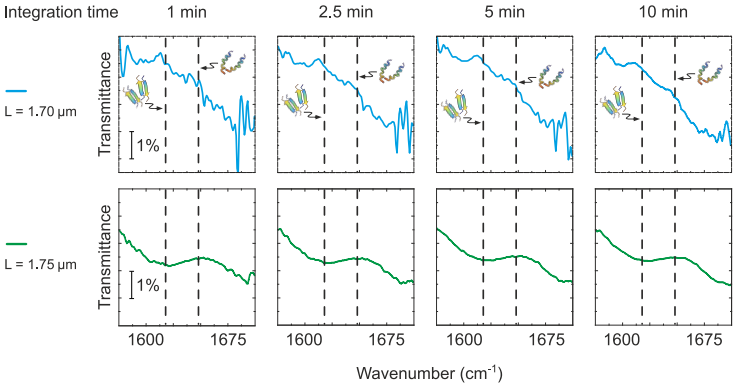

Figure 6.5: Antenna spectra measured with the laser at two different antennas for a different integration times. Already after 1 min measurement time vibrational features become visible. The SNR 1.75 µm long antenna is maximum, as the antenna resonance and laser frequency are minimally detuned. The 1.70 µm long antenna spectrum exhibits slightly higher noise. This can be attributed to the detuning between laser frequency (around 1634 cm^{-1}) and antenna resonance (around 1750 cm^{-1}).

6.3 DETECTING MOLECULAR CONFORMATION

So far, we conclude that the PLL monolayer on the investigated antennas is predominantly in the α-helical conformation. In a next step, we prepare a sample in the β-sheet state by adding SDS to the D_2O solution in order to examine the distinguishability of the individual conformations. Initially, the sample is investigated employing the Globar and spectra are accumulated for about 8 h. Figure 6.6 depicts the measured spectrum (light green) in the left panel. In the D_2O-SDS environment, we utilized a 1.8 µm long antenna. For better comparison to the previous measurements, the Globar spectrum (dark green) of the 1.75 µm long antenna measured in D_2O, is plotted in green. The 1.8 µm long antenna spectrum exhibits a higher noise level, in consequence of the added SDS to the D_2O environment, which exhibits *OH* vibrations in the considered frequency range, adding noise to the spectrum. Please note, that no vibrational modes can be identified in the spectra taken with the Globar, as expected.

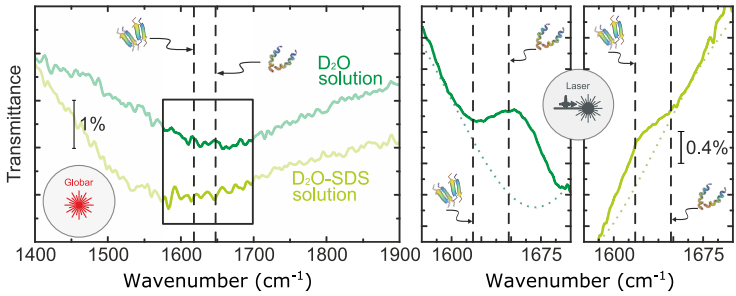

Figure 6.6: Comparison of measurements conducted in D_2O (dark green) D_2O-SDS (light green) solutions. Whereas both PLL conformations can be present in the first case, the polypeptides are mainly in the β-sheet state in the latter case. Antenna spectra that are recorded with the Globar in order to characterize the antenna resonances in the different liquid environments are depicted in the left panel. The right two panels depict the inset region of the left panel, when investigated with the laser source, including Lorentzian fits of the bare antenna background as short-dotted lines. In contrast to the measurement in D_2O solution (dark green), which only exhibits a strong α-helical signal, a broad peak in the vicinity of the β-sheet resonance is visible in D_2O-SDS solution (light green) and no α-helical signal is detected in D_2O-SDS, as expected.

Next, the sample is investigated employing the laser light source and the spectra are depicted in the right two panels of fig. 6.6, including Lorentzian fits of the bare antenna resonances to visualize the polypeptide signals. The measurement in D_2O solution is plotted in dark green. It is the same measurement, as previously shown fig. 6.4. The measurement conducted in D_2O-SDS is depicted in light green line color. Here, a broad feature close to the expected β-sheet vibration is visible on top of the antenna resonance, whereas the previously observed strong α-helical signal vanished. This indicates that the polypeptide monolayer mostly folded from the α-helical into the β-sheet conformation. But most importantly, both conformational vibrations can be detected and distinguished with the laser source, without applying any changes.

Several antennas have been investigated in D_2O-SDS solution, but no strong α-helical signal has been observed any more, whereas features at the β-sheet resonance became more prominent.

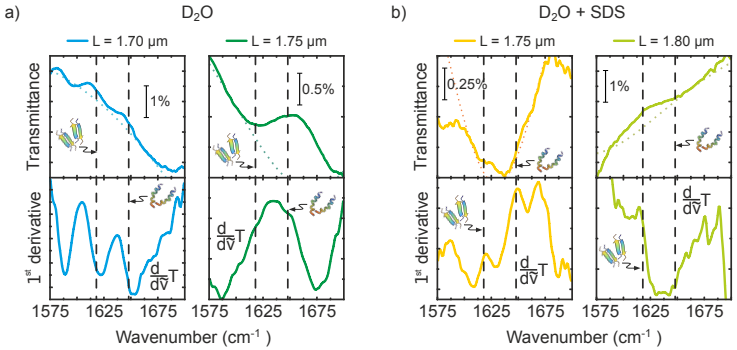

Figure 6.7: Antenna spectra and calculated 1^{st} derivatives of the laser measurements using different antenna lengths. The bare antenna spectra are indicated by Lorentzian fits as short-dotted lines to visualize the vibrational resonances on top of the antenna profiles. (**a**) Measured antennas in D_2O environment. Using a 1.7 µm long antenna, the spectrum exhibits peaks at both the α-helical and β-sheet resonances. The 1^{st} derivative also exhibits these peaks. On a 1.75 µm long antenna only a strong α-helical signal is visible, as discussed in the manuscript. This strong peak is also clearly visible on the 1^{st} derivative. (**b**) Measured antennas in D_2O-SDS environment. Here, a 1.75 µm and a 1.8 µm long antenna are investigated. Both antennas exhibit signals at the β-sheet resonance, but at a relatively low amplitude. One reason is the higher noise level caused by the D_2O-SDS environment. The β-sheet signals are also visible in the 1^{st} derivatives. The 1.75 µm long antenna might also exhibit a weak α-helical signal, as indicated by both the spectrum and the 1^{st} derivative.

We also investigated other nanoantennas in both surroundings. In fact, α-helical and β-sheet conformations can be seen in D_2O solution, as expected (fig. 6.7 **a**). We observe a similar behaviour for the D_2O-SDS evironment, but regarding the β-sheet conformation. One can see that PLL denaturates either to a near-unity β-sheet state distribution or a combination of both states (fig. 6.7 **b**).

Thus, we investigated in-vitro polypeptide monolayers on single gold nanoantennas exploiting resonant surface enhanced infrared absorption spectroscopy. We employed a tunable parametric light source based on a solid-state laser, which additionally brought significant improvements in terms of an increased signal-to-noise ratio and decreased measurement times compared to

Globar or synchrotron light sources. We successfully detected resonances attributed to both the α-helical and β-sheet conformation within minutes, without frequency tuning of the light source.

7

Summary & Outlook

In conclusion, we have demonstrated in-vitro observation and tracking of polypeptide conformational changes at the monolayer level utilizing surface-enhanced infrared absorption (SEIRA) spectroscopy. We further extended the concept of plasmonic nanosensors to vibrational detection and investigation of small biomolecules, such as minicollages, as well as polypeptides of larger size making use of their unique infrared spectral fingerprints.

On the route to single molecule vibrational detection of biological entities and of their conformational state many intermediate steps have to be considered and optimized to achieve this ambitious goal. These are in detail the nanostructure design, the functionalization scheme, the experimental setup, and the data analysis.

As the first milestone, we optimized the design of the utilized nanostructures with the help of finite-difference time-domain simulations. One important goal is to maximize the near-field enhancement, which is critical for the sensitivity of the nanosensors. We utilized two different concepts which are solid metallic nanoantennas and nanoslits in metallic films, so-called inverse antennas. While we could demonstrate outstanding sensing performance with these structures, we envision that further optimization for example, a fan-shaped or bowtie-design, can further improve the sensitivity as these structures can localize the near-field more efficiently [28, 109, 163–165] and thus allow to address smaller volumes and thus fewer molecules. Furthermore, metasurfaces made of non-standard plasmonic materials such as graphene [32] or dielectrics [166, 167], allow for additional tuning and optimization. These approaches allow the investigated molecules to be located at the "hot spots" of smaller size, meaning that one could probe even fewer molecular items.

The second important ingredient is the functionalization scheme, that is, the strategy for binding the molecular entities to the plasmonic nanosensor. We explored in depth the different functionalization schemes [108] and were thus able to bring this concept closer to real-world applications. We applied specifically designed thiol-linkers which bind well to gold surfaces and allow for tethering our molecular entities of interest to the nanoantennas and into the near-field. Apart from this ansatz, we also extended the tool box with more sophisticated functionalization schemes which allow one to bind virtually any collagen, polypeptide, or protein molecule, not only artificially synthesized ones. This opens up the pathway for using this approach in medical applications.

To monitor protein folding dynamics, we designed specialized fluidic cells for our measurements. As the proteins only undergo structural changes in an in-vitro, that is, aqueous surrounding, great care must be taken in the design of the sample cell. The cells need to allow optical access to the sample in reflection or transmission while allowing one to exchange the aqueous solutions in the cell, heating and cooling the solutions, as well as minimizing the optical path length in the highly IR absorbing water environment.

Our studies demonstrated that the investigation of proteins in minor amounts requires not only sophisticated experimental solutions but also detailed data analysis. In addition to the standard baseline-correction, we widely applied principal component analysis (PCA) to reveal the smallest dynamics of the system probed. Recently, an adaptive baseline-correction method demonstrated the ability to estimate solution concentrations [168]. Combination of these approaches is a powerful tool for the data post-processing, which allows for obtaining more insights and compensates for experimental imperfections.

Via our comprehensive study, it was shown that all the mentioned aspects are of high importance for ultrasensitive molecular detection. Therefore, our biosensor enables reliable tracking of conformational changes under various external stimuli

via monitoring the amide I vibration. By binding polypeptide molecules to gold nanoantennas, we certify that secondary structure changes of one protein monolayer can take place reversibly.

We believe that with further advances it will be possible to scale the process to a few or single proteins and observe the conformational behavior of individual entities. As the first step in this direction, we investigated in-vitro polypeptide monolayers on a single gold nanoantenna exploiting resonant vibrational surface enhanced infrared absorption spectroscopy. These experiments face an additional limiting factor, namely, the use of standard light sources due to their limited brilliance. To make our concept feasible for tabletop applications, we utilized the laser light source, which allowed us to study species at attomolar concentrations in attoliter volumes on a daily basis.

Going beyond the approaches demonstrated and ideas discussed, the versatility of SEIRA, functionalization scheme, and the laser light source will lead to a multitude of new optical sensor designs and applications. In the future, integrated chip-level technology for biological and even medical applications and for point-of-care testing of biosamples in minor amounts may tremendously benefit neurodegenerative patients, as protein misfolding is believed to be at the root of these diseases [128, 169, 170].

Acronyms

Au gold

CaF_2 calcium floride

CD circular dichroism

NMR nuclear magnetic resonance

AFM atomic force microscopy

IR infrared

FT Fourier-transform

FTIR Fourier-transform infrared

SEIRA surface-enhanced infrared absorption

EF enhancement factor

PLL poly-L-lysine

FDTD finite-difference time-domain

EBL electron beam lithography

PMMA poly(methyl methacrylate)

E-beam electron beam

MIBK methyl isobutyl ketone

NEP N-Ethylpyrrolidone

IPA isopropyl alcohol

MUA 11-mercaptoundecanoic acid

MUoL 11-mercaptoundecanol

NHSS N-Hydroxysulfosuccinimide sodium salt

EDC N-(3-Dimethylaminopropyl)-N′-ethylcarbodiimide hydrochloride

MES 2-(N-Morpholino)ethanesulfonic acid

PBS phosphate-buffered saline

MCT mercury-cadmium-telluride

PDMS polydimethylsiloxane

Globar glowbar

SNR signal-to-noise ratio

RMS root mean square

SLS Swiss Light Source

PSI Paul Scherrer Institute

OPO optical parametric oscillator

ffOPO fiber-feedback optical parametric oscillator

Yb Ytterbium

OPA optical parametric amplifier

DFG difference frequency generation

PCA principal component analysis

PC principal component

IRRAS infrared reflection-absorption spectroscopy

SDS sodium dodecyl sulfate

PID proportional integral derivative

SEM scanning electron microscopy

SNOM scanning near-field optical microscope

List of Figures

Bibliography

[1] S. M. Kelly, T. J. Jess, and N. C. Price, "How to study proteins by circular dichroism," Biochimica et Biophysica Acta - Proteins and Proteomics **1751,** 119–139 (2005).

[2] N. J. Greenfield, "Using circular dichroism spectra to estimate protein secondary structure.," Nature protocols **1,** 2876–2890 (2006).

[3] R. Gopal, J. S. Park, C. H. Seo, and Y. Park, "Applications of circular dichroism for structural analysis of gelatin and antimicrobial peptides," International Journal of Molecular Sciences **13,** 3229–3244 (2012).

[4] S. Boutet *et al.*, "High-Resolution Protein Structure Determination by Serial Femtosecond Crystallography," Science (New York, N.Y.) **337,** 362–364 (2012).

[5] F. Schotte, M. Lim, T. A. Jackson, A. V. Smirnov, J. Soman, J. S. Olson, G. N. J. Phillips, M. Wulff, and P. A. Anfinrud, "Watching a protein as it functions with 150-ps time-resolved x-ray crystallography," Science (New York, N.Y.) **300,** 1944–1947 (2003).

[6] G. M. Clore and A. M. Gronenborn, "Structures of larger proteins in solution: three- and four-dimensional heteronuclear NMR spectroscopy," Science (New York, N.Y.) **252,** 1390–1399 (1991).

[7] K. Wüthrich, "Protein structure determination in solution by NMR spectroscopy," Journal of Biological Chemistry **265,** 22059–22062 (1990).

[8] N. Aslam, M. Pfender, P. Neumann, R. Reuter, A. Zappe, F. F. D. Oliveira, A. Denisenko, S. Onoda, J. Isoya, and J.

Wrachtrup, "Nanoscale nuclear magnetic resonance with chemical resolution," Science (New York, N.Y.) **357,** 67–71 (2017).

[9] F. S. Ruggeri, J. Adamcik, J. S. Jeong, H. A. Lashuel, R. Mezzenga, and G. Dietler, "Influence of the β-sheet content on the mechanical properties of aggregates during amyloid fibrillization," Angewandte Chemie - International Edition **54,** 2462–2466 (2015).

[10] I. Amenabar *et al.*, "Structural analysis and mapping of individual protein complexes by infrared nanospectroscopy," Nature Communications **4,** 2890 (2013).

[11] A. Barth, "Infrared spectroscopy of proteins," Biochimica et Biophysica Acta - Bioenergetics **1767,** 1073–1101 (2007).

[12] J. L. Lippert, D. Tyminski, and P. J. Desmeules, "Determination of the secondary structure of proteins by laser Raman spectroscopy.," Journal of the American Chemical Society **98,** 7075–7080 (1976).

[13] A. Barth and P. I. Haris, *Biological and biomedical infrared spectroscopy.* (IOS Press, Amsterdam, 2009).

[14] F. Dousseau and M. Pézolet, "Determination of the secondary structure content of proteins in aqueous solutions from their amide I and amide II infrared bands. Comparison between classical and partial least-squares methods.," Biochemistry **29,** 8771–8779 (1990).

[15] D. C. Lee, $. Parvez, I. Hark, D. Chapman, and R. C. Mitchellt, "Determination of Protein Secondary Structure Using Factor Analysis of Infrared Spectra+," Biochemistry **29,** 9185–9193 (1990).

[16] S. Y. Venyaminov and N. N. Kalnin, "Quantitative IR spectrophotometry of peptide compounds in water (H2O) solutions. II. Amide absorption bands of polypeptides and

fibrous proteins in α-, β-, and random coil conformations," Biopolymers **30,** 1259–1271 (1990).

[17] W. Dzwolak and V. Smirnovas, "A conformational α-helix to β-sheet transition accompanies racemic self-assembly of polylysine: An FT-IR spectroscopic study," Biophysical Chemistry **115,** 49–54 (2005).

[18] W. Dzwolak, T. Muraki, M. Kato, and Y. Taniguchi, "Chain-length dependence of α-helix to β-sheet transition in polylysine: Model of protein aggregation studied by temperature-tuned FTIR spectroscopy," Biopolymers **73,** 463–469 (2004).

[19] L. P. Deflores, Z. Ganim, R. A. Nicodemus, and A. Tokmakoff, "Amide I-II 2D IR spectroscopy provides enhanced protein secondary structural sensitivity," Journal of the American Chemical Society **131,** 3385–3391 (2009).

[20] F. Neubrech, A. Pucci, T. W. Cornelius, S. Karim, A. García-Etxarri, and J. Aizpurua, "Resonant plasmonic and vibrational coupling in a tailored nanoantenna for infrared detection," Physical Review Letters **101,** 157403 (2008).

[21] L. Kühner, M. Hentschel, U. Zschieschang, H. Klauk, J. Vogt, C. Huck, H. Giessen, and F. Neubrech, "Nanoantenna-Enhanced Infrared Spectroscopic Chemical Imaging," ACS Sens **2,** 655–662 (2017).

[22] F. Neubrech, C. Huck, K. Weber, A. Pucci, and H. Giessen, "Surface-Enhanced Infrared Spectroscopy Using Resonant Nanoantennas," Chemical Reviews **117,** 5110–5145 (2017).

[23] C. Huck, F. Neubrech, J. Vogt, A. Toma, D. Gerbert, J. Katzmann, T. Härtling, and A. Pucci, "Surface-enhanced infrared spectroscopy using nanometer-sized gaps," ACS Nano **8,** 4908–4914 (2014).

[24] Y. Zhang, Y.-R. Zhen, O. Neumann, J. K. Day, P. Nordlander, and N. J. Halas, "Coherent anti-Stokes Raman scattering with single-molecule sensitivity using a plasmonic Fano resonance," Nature Communications **5,** 1–7 (2014).

[25] T. Zentgraf, T. P. Meyrath, A. Seidel, S. Kaiser, H. Giessen, C. Rockstuhl, and F. Lederer, "Babinet's principle for optical frequency metamaterials and nanoantennas," Physical Review B - Condensed Matter and Materials Physics **76,** 4–7 (2007).

[26] D. Dregely, F. Neubrech, H. Duan, R. Vogelgesang, and H. Giessen, "Vibrational near-field mapping of planar and buried three-dimensional plasmonic nanostructures," Nature Communications **4,** 2237 (2013).

[27] C. Huck, J. Vogt, M. Sendner, D. Hengstler, F. Neubrech, and A. Pucci, "SI Plasmonic Enhancement of Infrared Vibrational Signals: Nanoslits versus Nanorods," ACS Photonics **2,** 1489–1497 (2015).

[28] L. Dong, X. Yang, C. Zhang, B. Cerjan, L. Zhou, M. L. Tseng, Y. Zhang, A. Alabastri, P. Nordlander, and N. J. Halas, "Nanogapped Au Antennas for Ultrasensitive Surface-Enhanced Infrared Absorption Spectroscopy," Nano Letters **17,** 5768−5774 (2017).

[29] J. N. Anker, W. P. Hall, O. Lyandres, N. C. Shah, J. Zhao, and R. P. V. Duyne, "Biosensing with plasmonic nanostructure," Nature Materials **7,** 442–453 (2008).

[30] R. Adato, A. A. Yanik, J. J. Amsden, D. L. Kaplan, F. G. Omenetto, M. K. Hong, S. Erramilli, and H. Altug, "Ultra-sensitive vibrational spectroscopy of protein monolayers with plasmonic nanoantenna arrays.," Proceedings of the National Academy of Sciences of the United States of America **106,** 19227–19232 (2009).

[31] I. Ament, J. Prasad, A. Henkel, S. Schmachtel, and C. Sönnichsen, "Single unlabeled protein detection on individual plasmonic nanoparticles," Nano Letters **12,** 1092–1095 (2012).

[32] D. Rodrigo, O. Limaj, D. Janner, D. Etezadi, F. Javier García De Abajo, V. Pruneri, and H. Altug, "Mid-Infrared Plasmonic Biosensing with Graphene," Science (New York, N.Y.) **349,** 165–168 (2015).

[33] D. Zhang, O. Neumann, H. Wang, V. M. Yuwono, A. Barhoumi, M. Perham, J. D. Hartgerink, P. Wittung-Stafshede, and N. J. Halas, "Gold nanoparticles can induce the formation of protein-based aggregates at physiological pH," Nano Letters **9,** 666–671 (2009).

[34] R. Adato and H. Altug, "In-situ ultra-sensitive infrared absorption spectroscopy of biomolecule interactions in real time with plasmonic nanoantennas," Nature Communications **4,** 2154 (2013).

[35] K. Boratay Alici and I. F. Gallardo, "Detecting secondary structure and surface orientation of helical peptide monolayers from resonant hybridization signals," Scientific Reports **3,** 2956 (2013).

[36] R. Adato, S. Aksu, and H. Altug, "Engineering mid-infrared nanoantennas for surface enhanced infrared absorption spectroscopy," Materials Today **18,** 436–446 (2015).

[37] O. Limaj, D. Etezadi, N. J. Wittenberg, D. Rodrigo, D. Yoo, S. H. Oh, and H. Altug, "Infrared Plasmonic Biosensor for Real-Time and Label-Free Monitoring of Lipid Membranes," Nano Letters **16,** 1502–1508 (2016).

[38] D. Etezadi, J. B. Warner, F. S. Ruggeri, G. Dietler, H. A. Lashuel, and H. Altug, "Nanoplasmonic mid-infrared biosensor for in vitro protein secondary structure detection," Light: Science & Applications **6,** e17029 (2017).

[39] D. Etezadi, J. B. Warner, H. A. Lashuel, and H. Altug, "Real-Time In Situ Secondary Structure Analysis of Protein Monolayer with Mid-Infrared Plasmonic Nanoantennas," ACS Sensors **3,** 1109–1117 (2018).

[40] I. F. Almog, M. S. Bradley, and V. Bulovi, "The Lorentz Oscillator and its Applications," MIT OpenCourseWare pp. 1–34 (2011).

[41] M. A. Ordal, R. J. Bell, R. W. Alexander, L. L. Long, and M. R. Querry, "Optical properties of fourteen metals in the infrared and far infrared: Al, Co, Cu, Au, Fe, Pb, Mo, Ni, Pd, Pt, Ag, Ti, V, and W," Applied Optics **24,** 4493 (1985).

[42] H. A. Lorentz, *The theory of electrons and its applications to the phenomena of light and radiant heat* (G. E. Stechert & Co., New York, 1916).

[43] F. Forstmann and R. R. Gerhardts, *Metal Optics Near the Plasma Frequency*, *Springer Tracts in Modern Physics* (Springer Berlin Heidelberg, 2006).

[44] K. P. Chen, V. P. Drachev, J. D. Borneman, A. V. Kildishev, and V. M. Shalaev, "Drude relaxation rate in grained gold nanoantennas," Nano Letters **10,** 916–922 (2010).

[45] L. Du, X. Zhang, T. Mei, and X. Yuan, "Localized surface plasmons, surface plasmon polaritons, and their coupling in 2d metallic array for sers," Opt. Express **18,** 1959 (2010).

[46] K. M. McPeak, S. V. Jayanti, S. J. P. Kress, S. Meyer, S. Iotti, A. Rossinelli, and D. J. Norris, "Plasmonic Films Can Easily Be Better: Rules and Recipes," ACS Photonics (2015).

[47] T. Sandu, "Near-field and extinction spectra of rod-shaped nanoantenna dimers," Proceedings of the Romanian Academy Series A - Mathematics Physics Technical Sciences Information Science **15,** 338–345 (2014).

[48] J. Aizpurua, G. W. Bryant, L. J. Richter, F. J. García De Abajo, B. K. Kelley, and T. Mallouk, "Optical properties of coupled metallic nanorods for field-enhanced spectroscopy," Physical Review B - Condensed Matter and Materials Physics **71,** 1–13 (2005).

[49] N. Verellen, F. López-Tejeira, R. Paniagua-Domínguez, D. Vercruysse, D. Denkova, L. Lagae, P. Van Dorpe, V. V. Moshchalkov, and J. A. Sánchez-Gil, "Mode parity-controlled fano- and lorentz-like line shapes arising in plasmonic nanorods," Nano Letters **14,** 2322–2329 (2014).

[50] F. Neubrech, A. Garcia-Etxarri, D. Weber, J. Bochterle, H. Shen, M. Lamy De La Chapelle, G. W. Bryant, J. Aizpurua, and A. Pucci, "Defect-induced activation of symmetry forbidden infrared resonances in individual metallic nanorods," Applied Physics Letters **96,** 2008–2011 (2010).

[51] M. Staffaroni, J. Conway, S. Vedantam, J. Tang, and E. Yablonovitch, "Circuit analysis in metal-optics," Photonics and Nanostructures - Fundamentals and Applications **10,** 166–176 (2012).

[52] L. Novotny, "Effective wavelength scaling for optical antennas," Physical Review Letters (2007).

[53] T. Steinle, F. Neubrech, A. Steinmann, X. Yin, and H. Giessen, "Mid-infrared Fourier-transform spectroscopy with a high-brilliance tunable laser source: investigating sample areas down to 5 μm diameter," Optics Express **23,** 11105 (2015).

[54] A. A. Maradudin, I. Simonsen, J. Polanco, and R. M. Fitzgerald, "Phase resonances in compound metallic gratings Rayleigh and Wood anomalies in the diffraction of light from a perfectly conducting reflection grating," Journal of Optics 18 (2016).

[55] R. Wood, "On a Remarkable Case of Uneven Distribution of Light in a Diffraction Grating Spectrum," Proceedings of the Physical Society of London **18,** 269 (1902).

[56] L. Rayleigh, "III. Note on the remarkable case of diffraction spectra described by Prof. Wood," Philos. Mag. **14,** 60–65 (1907).

[57] L. Rayleigh, "On the Dynamical Theory of Gratings Source : Proceedings of the Royal Society of London . Series A , Containing Papers of a Published by : The Royal Society Stable URL :," Proc. R. Soc. Lond **79,** 399–416 (1907).

[58] U. Fano, "The Theory of Anomalous Diffraction Gratings and of Quasi-Stationary Waves on Metallic Surfaces (Sommerfeld's Waves)," Journal of the Optical Society of America **31,** 213 (1941).

[59] D. Weber, P. Albella, P. Alonso-González, F. Neubrech, H. Gui, T. Nagao, R. Hillenbrand, J. Aizpurua, and A. Pucci, "Longitudinal and transverse coupling in infrared gold nanoantenna arrays: long range versus short range interaction regimes,", 2011.

[60] J. B. Khurgin, "How to deal with the loss in plasmonics and metamaterials," NATURE NANOTECHNOLOGY www.nature.com/naturenanotechnology 10 (2015).

[61] S. Bagheri, K. Weber, T. Gissibl, T. Weiss, F. Neubrech, and H. Giessen, "Fabrication of Square-Centimeter Plasmonic Nanoantenna Arrays by Femtosecond Direct Laser Writing Lithography/ Effects of Collective Excitations on SEIRA Enhancement," ACS Photonics **2,** 779–786 (2015).

[62] A. De Marcellis, E. Palange, M. Janneh, C. Rizza, A. Ciattoni, and S. Mengali, "Design Optimisation of Plasmonic Metasurfaces for Mid-Infrared High-Sensitivity Chemical Sensing," Plasmonics **12,** 293–298 (2017).

[63] N. Liu, T. Weiss, M. Mesch, L. Langguth, U. Eigenthaler, M. Hirscher, C. Sönnichsen, and H. Giessen, "Planar metamaterial analogue of electromagnetically induced transparency for plasmonic sensing," Nano Letters **10,** 1103–1107 (2010).

[64] B. Ögüt, R. Vogelgesang, W. Sigle, N. Talebi, C. T. Koch, and P. A. Van Aken, "Hybridized metal slit eigenmodes as an illustration of Babinet's principle," ACS Nano **5,** 6701–6706 (2011).

[65] M. Hentschel, T. Weiss, S. Bagheri, and H. Giessen, "Babinet to the Half: Coupling of Solid and Inverse Plasmonic Structures," Nano Letters **13,** 4428–4433 (2013).

[66] H. U. Yang, R. L. Olmon, K. S. Deryckx, X. G. Xu, H. A. Bechtel, Y. Xu, B. A. Lail, and M. B. Raschke, "Accessing the Optical Magnetic Near-Field through Babinet's Principle," ACS Photonics **1,** 894–899 (2014).

[67] C. Huck, J. Vogt, M. Sendner, D. Hengstler, F. Neubrech, and A. Pucci, "Plasmonic Enhancement of Infrared Vibrational Signals: Nanoslits versus Nanorods," ACS Photonics **2,** 1489–1497 (2015).

[68] P. Mühlschlegel, H.-J. Eisler, O. J. F. Martin, B. Hecht, and D. W. Pohl, "Resonant Optical Antennas," Science **308,** 1607–1610 (2005).

[69] B. Gallinet, O. J. F. Martin, S. Zhang, L.-H. Zhang, Q.-Q. Li, Z.-H. Hao, and Q.-Q. Wang, "Relation between near–field and far–field properties of plasmonic Fano resonances," Appl. Phys. A, Mater. Sci. Process. ACS Nano Z.-J. Yang, Z.- (C) OPTICS EXPRESS **100,** 333–339 (2010).

[70] A. Pucci, F. Neubrech, D. Weber, S. Hong, T. Toury, and M. Lamy de la Chapelle, "Surface enhanced infrared spectroscopy using gold nanoantennas," Physica Status Solidi (B) Basic Research **247,** 2071–2074 (2010).

[71] T. Neuman, C. Huck, J. Vogt, F. Neubrech, R. Hillenbrand, J. Aizpurua, and A. Pucci, "Importance of Plasmonic Scattering for an Optimal Enhancement of Vibrational Absorption in SEIRA with Linear Metallic Antennas," The Journal of Physical Chemistry C **119,** 26652–26662 (2015).

[72] C. D'Andrea *et al.*, "Optical Nanoantennas for Multiband Spectroscopy," ACS Nano **7,** 3522–3531 (2013).

[73] R. C. Hansen and L. L. Bailin, "A New Method of Near Field Analysis," IRE Trans. Antennas Propag. **7,** S458 (1959).

[74] D. E. Freeman, "Vibrational Spectroscopy in Optics and Spectroscopy," J. Opt. Soc. Am **52,** 103–110 (1962).

[75] F. Sanger, "The Arrangement of Amino Acids in Proteins," Advances in Protein Chemistry **7,** 1–67 (1952).

[76] C. B. Anfinsen, "The formation and stabilization of protein structure," Biochemical Journal **128,** 737–749 (1972).

[77] K. Wüthrich, M. Billeter, and W. Braun, "Pseudo-structures for the 20 common amino acids for use in studies of protein conformations by measurements of intramolecular proton-proton distance constraints with nuclear magnetic resonance," Journal of Molecular Biology **169,** 949–961 (1983).

[78] J. Kubelka, J. Hofrichter, and W. A. Eaton, "The protein folding 'speed limit'," Current Opinion in Structural Biology **14,** 76–88 (2004).

[79] S. Govindarajan, R. Recabarren, and R. A. Goldstein, "Estimating the total number of protein folds," Proteins: Structure, Function and Genetics **35,** 408–414 (1999).

[80] H. P. Erickson, "Size and shape of protein molecules at the nanometer level determined by sedimentation, gel filtration, and electron microscopy," Biological Procedures Online **11,** 32–51 (2009).

[81] J. T. Pelton and L. R. McLean, "Spectroscopic methods for analysis of protein secondary structure.," Analytical biochemistry (2000).

[82] L. A. Forato, R. Bernardes-Filho, and L. A. Colnago, "Protein structure in KBr pellets by infrared spectroscopy.," Analytical biochemistry (1998).

[83] A. Barth and C. Zscherp, "What vibrations tell about proteins," Quarterly Reviews of Biophysics **35,** 369–430 (2002).

[84] C. Kötting and K. Gerwert, "Proteins in action monitored by time-resolved FTIR spectroscopy," ChemPhysChem **6,** 881–888 (2005).

[85] M. Rozenberg and G. Shoham, "FTIR spectra of solid poly-l-lysine in the stretching NH mode range," Biophysical Chemistry (2007).

[86] V. Giannini, Y. Francescato, H. Amrania, C. C. Phillips, and S. A. Maier, "Fano resonances in nanoscale plasmonic systems: A parameter-free modeling approach," Nano Letters **11,** 2835–2840 (2011).

[87] V. Giannini, Y. Francescato, H. Amrania, C. C. Phillips, and S. A. Maier, "Fano resonances in nanoscale plasmonic systems: A parameter-free modeling approach," Nano Letters **11,** 2835–2840 (2011).

[88] E. J. Osley, C. G. Biris, P. G. Thompson, R. R. Jahromi, P. A. Warburton, and N. C. Panoiu, "Fano resonance resulting from a tunable interaction between molecular vibrational modes and a double continuum of a plasmonic metamolecule," Physical Review Letters **110,** 1–5 (2013).

[89] J. Vogt, C. Huck, F. Neubrech, A. Toma, D. Gerbert, and A. Pucci, "Impact of the plasmonic near- and far-field resonance-energy shift on the enhancement of infrared vibrational signals," Phys. Chem. Chem. Phys. **17,** 21169–21175 (2015).

[90] B. Gallinet, A. Lovera, T. Siegfried, H. Sigg, and O. J. F. Martin, "Fano resonant plasmonic systems: Functioning principles and applications," AIP Conf Proc **1475,** 18–20 (2012).

[91] C. T. Chong, N. J. Halas, H. Giessen, P. Nordlander, N. I. Zheludev, S. A. Maier, and B. Luk'yanchuk, "The Fano resonance in plasmonic nanostructures and metamaterials," Nature Materials **9,** 707–715 (2010).

[92] U. Fano, "Effects of Configuration Interaction on Intensities and Phase Shifts," Physical Review **124,** 1866–1878 (1961).

[93] F. Neubrech, S. Beck, T. Glaser, M. Hentschel, H. Giessen, and A. Pucci, "Spatial extent of plasmonic enhancement of vibrational signals in the infrared," ACS Nano **8,** 6250–6258 (2014).

[94] A. Gandman, R. T. Mackin, B. Cohn, I. V. Rubtsov, and L. Chuntonov, "Radiative Enhancement of Linear and Third-Order Vibrational Excitations by an Array of Infrared Plasmonic Antennas," ACS Nano **12,** 4521–4528 (2018).

[95] J. Zuloaga and P. Nordlander, "On the energy shift between near-field and far-field peak intensities in localized plasmon systems," Nano Letters **11,** 1280–1283 (2011).

[96] P. Alonso-González *et al.*, "Experimental verification of the spectral shift between near- and far-field peak intensities of plasmonic infrared nanoantennas," Physical Review Letters **110,** 203902 (2013).

[97] Www.lumerical.com/, "Lumerical Solutions, Inc.,".

[98] A. Taflove and S. Hagness, *Computational electrodynamics: the finite-difference time-domain method. 2nd ed* (2000).

[99] E. D. Palik, *Handbook of Optical Constants of Solids* (Academic Press, Burlington, 1997).

[100] Venyaminov SYu and F. G. Prendergast, "Water (H2O and D2O) molar absorptivity in the 1000-4000 cm-1 range and quantitative infrared spectroscopy of aqueous solutions.," Analytical biochemistry (1997).

[101] P. P. Sethna, K. F. Palmer, and D. Williams, "Optical constants of D 2 0 in the infrared*," .

[102] H. R. Zelsmann, "Temperature dependence of the optical constants for liquid H2O and D2O in the far IR region,", 1995.

[103] S. Bagheri, H. Giessen, and F. Neubrech, "Large-Area Antenna-Assisted SEIRA Substrates by Laser Interference Lithography," Advanced Optical Materials **2,** 1050–1056 (2014).

[104] N. Sahu, B. Parija, and S. Panigrahi, "Fundamental understanding and modeling of spin coating process: A review," Indian Journal of Physics **83,** 493–502 (2009).

[105] J. Singh and D. E. Wolfe, "Nanostructured component fabrication by electron beam-physical vapor deposition," Journal of Materials Engineering and Performance **14,** 448–459 (2005).

[106] F. Weiher, M. Schatz, C. Steinem, and A. Geyer, "Silica precipitation by synthetic minicollagens," Biomacromolecules **14,** 683–687 (2013).

[107] B. L. Frey and R. M. Corn, "Covalent Attachment and Derivatization of Poly(L-lysine) Monolayers on Gold Surfaces As Characterized by Polarization-Modulation FT-IR Spectroscopy," Biosensors: Fundamentals and Applications Biosensors, A Practical Approach Anal. Chim. Acta J. Biosens. Bioelectron **307,** 277–289 (1987).

[108] M. A. Fallah, C. Stanglmair, C. Pacholski, and K. Hauser, "Devising self-assembled-monolayers for surface-enhanced

infrared spectroscopy of pH-driven poly-l-lysine conformational changes," Langmuir : the ACS journal of surfaces and colloids **32,** 7356–7364 (2016).

[109] T. H. Le and T. Tanaka, "Plasmonics-Nanofluidics Hydrid Metamaterial: An Ultrasensitive Platform for Infrared Absorption Spectroscopy and Quantitative Measurement of Molecules," ACS Nano **11,** 9780–9788 (2017).

[110] B. Lehmkuhl, S. D. Noblitt, A. T. Krummel, and C. S. Henry, "Fabrication of IR-transparent microfluidic devices by anisotropic etching of channels in CaF2," Lab Chip **15,** 4364–4368 (2015).

[111] F. Mörz, R. Semenyshyn, T. Steinle, F. Neubrech, U. Zschieschang, H. Klauk, A. Steinmann, and H. Giessen, "Nearly diffraction limited FTIR mapping using an ultrastable broadband femtosecond laser tunable from 1.33 to 8 μm," Optics Express **25,** 32355 (2017).

[112] T. Steinle, F. Neubrech, A. Steinmann, X. Yin, and H. Giessen, "Mid-infrared Fourier-transform spectroscopy with a high-brilliance tunable laser source : investigating sample areas down to 5 μ m diameter," Optics Express **23,** 9005–9010 (2015).

[113] C. Petibois, G. Deleris, M. Piccinini, M. Cestelli-Guidi, and A. Marcelli, "A bright future for synchrotron imaging," Nature Photonics **3,** 179 (2009).

[114] P. Dumas, F. Polack, B. Lagarde, O. Chubar, J. L. Giorgetta, and S. Lefrançois, "Synchrotron infrared microscopy at the French Synchrotron Facility SOLEIL," Infrared Physics and Technology **49,** 152 (2006).

[115] Y. L. Mathis, B. Gasharova, and D. Moss, "Terahertz radiation at ANKA, the new synchrotron light source in Karlsruhe," Journal of Biological Physics **29,** 313–318 (2003).

[116] P. Lerch *et al.*, "IR beamline at the Swiss Light Source," Journal of Physics: Conference Series **359,** 012003 (2012).

[117] J. Mandon, G. Guelachvili, and N. Picqué, "Fourier transform spectroscopy with a laser frequency comb," Nature Photonics **3,** 99–102 (2009).

[118] M. R. Alcaráz, A. Schwaighofer, C. Kristament, G. Ramer, M. Brandstetter, H. Goicoechea, and B. Lendl, "External-Cavity Quantum Cascade Laser Spectroscopy for Mid-IR Transmission Measurements of Proteins in Aqueous Solution," Analytical Chemistry **87,** 6980–6987 (2015).

[119] F. Borondics, M. Jossent, C. Sandt, L. Lavoute, D. Gaponov, A. Hideur, P. Dumas, and S. Février, "Supercontinuum-based Fourier transform infrared spectromicroscopy," Optica **5,** 378 (2018).

[120] A. Savitzky and M. J. Golay, "Smoothing and Differentiation of Data by Simplified Least Squares Procedures," Analytical Chemistry **36,** 1627–1639 (1964).

[121] P. H. C. Eilers, "A perfect smoother," Analytical Chemistry **75,** 3631–3636 (2003).

[122] J. Vogt, C. Huck, F. Neubrech, A. Toma, D. Gerbert, and A. Pucci, "Impact of the plasmonic near- and far-field resonance-energy shift on the enhancement of infrared vibrational signals," Phys. Chem. Chem. Phys. **17,** 21169–21175 (2015).

[123] M. S. Wagner and D. G. Castner, "Characterization of Adsorbed Protein Films by Time-of-Flight Secondary Ion Mass Spectrometry with Principal Component Analysis," Langmuir **17,** 4649–4660 (2001).

[124] R. Semenyshyn, M. Hentschel, C. Stanglmair, T. Teutsch, C. Tarin, C. Pacholski, H. Giessen, and F. Neubrech, "In Vitro

Monitoring Conformational Changes of Polypeptide Monolayers Using Infrared Plasmonic Nanoantennas," Nano Letters **19,** 1–7 (2019).

[125] L. Kühner, R. Semenyshyn, M. Hentschel, F. Neubrech, C. Tarín, and H. Giessen, "Vibrational Sensing Using Infrared Nanoantennas: Toward the Noninvasive Quantitation of Physiological Levels of Glucose and Fructose," ACS Sensors p. acssensors.9b00488 (2019).

[126] R. Semenyshyn, M. Hentschel, C. Huck, J. Vogt, F. Weiher, H. Giessen, and F. Neubrech, "Resonant Plasmonic Nanoslits Enable in Vitro Observation of Single-Monolayer Collagen-Peptide Dynamics," ACS Sensors **4,** 1966–1972 (2019).

[127] C. Wu, A. B. Khanikaev, R. Adato, N. Arju, A. A. Yanik, H. Altug, and G. Shvets, "Fano-resonant asymmetric metamaterials for ultrasensitive spectroscopy and identification of molecular monolayers," Nature Materials **11,** 69–75 (2012).

[128] T. P. J. Knowles, M. Vendruscolo, and C. M. Dobson, "The amyloid state and its association with protein misfolding diseases," Nature Reviews Molecular Cell Biology **15,** 384–396 (2014).

[129] D. J. Irwin, V. M.-Y. Lee, and J. Q. Trojanowski, "Parkinson's disease dementia: convergence of α-synuclein, tau and amyloid-β pathologies," Nature Reviews Neuroscience **14,** 626–636 (2013).

[130] L. Hieronymus and S. Griffin, "Role of Amylin in Type 1 and Type 2 Diabetes," The Diabetes Educator **41,** 47S–56S (2015).

[131] S. Park, T. E. Klein, and V. S. Pande, "Folding and Misfolding of the Collagen Triple Helix: Markov Analysis of Molecular Dynamics Simulations," Biophysical Journal **93,** 4108–4115 (2007).

[132] Y. L. A. Rezus and O. Selig, "Impact of local-field effects on the plasmonic enhancement of vibrational signals by infrared nanoantennas," Optics Express **24,** 12202 (2016).

[133] Q. Xu and T. A. Keiderling, "Effect of sodium dodecyl sulfate on folding and thermal stability of acid-denatured cytochrome c: A spectroscopic approach," Protein Science **13,** 2949–2959 (2004).

[134] M. A. Bryan, J. W. Brauner, G. Anderle, C. R. Flach, B. Brodsky, and R. Mendelsohn, "FTIR studies of collagen model peptides: Complementary experimental and simulation approaches to conformation and unfolding," Journal of the American Chemical Society **129,** 7877–7884 (2007).

[135] G. M. Hale, M. R. Querry, A. N. Rusk, and D. Williams, "Influence of temperature on the spectrum of water," J. Opt. Soc. Am. **62,** 1103–1108 (1972).

[136] Y. Wang and Y. C. Chang, "Synthesis and conformational transition of surface-tethered polypeptide: Poly(L-lysine)," Macromolecules **36,** 6511–6518 (2003).

[137] S. Wold, K. Esbensen, and P. Geladi, "Principal Component Analysis," Chemometrics and Intelligent Laboratory Systems **2,** 37–52 (1987).

[138] A. B. Dahlin, J. O. Tegenfeldt, and F. Ho, "Improving the Instrumental Resolution of Sensors Based on Localized Surface Plasmon Resonance interfacial refractive index of nanoscale noble metal generic data analysis algorithms and a simple experimen- comparable to that of state-of-the art SPR systems," Anal. Chem. **78,** 4416–4423 (2006).

[139] Y. Francescato, V. Giannini, and S. A. Maier, "Plasmonic systems unveiled by fano resonances," ACS Nano (2012).

[140] M. Chittchang, N. Salamat-Miller, H. H. Alur, D. G. V. Velde, A. K. Mitra, and T. P. Johnston, "Poly(L-lysine) as a model drug macromolecule with which to investigate

secondary structure and microporous membrane transport, part 2: diffusion studies," Journal of Pharmacy and Pharmacology **54,** 1497–1505 (2002).

[141] M. Jackson, P. I. Haris, and D. Chapman, "Conformational transitions in poly(L-lysine)" studies using Fourier transform infrared spectroscopy," Biochimica et Biophysica Acta **998,** 75–79 (1989).

[142] Y. P. Myer, "The pH-induced helix-coil transition of poly-L-lysine and poly-L-glutamic acid and the 238-mμ dichroic dand," Macromolecules **2,** 624–628 (1969).

[143] G. Setpke, H.-a. Arfmann, and K. G. Wagner, "Synthesis and properties of alternating poly(Lys-Phe) and comparison with the random copolymer Poly(Lys51, Phe49)," Biopolymers **13,** 1621–1633 (1974).

[144] K. Xiong, E. K. Asciutto, J. D. Madura, and S. A. Asher, "Salt dependence of an α-helical peptide folding energy landscapes," Biochemistry **48,** 10818–10826 (2009).

[145] I. W. Shepherd, "Study of poly-L-lysine conformations in aqueous methanol solution by using polarized Raman techniques," Biochem. J. **155,** 543–548 (1976).

[146] I. Satake and J. E. N. T. S. I. Yang, "Effect of Temperature and pH on the alpha-helix Transition of Poly (L-Lysine) in Sodium Dodecyl Sulfate Solution," Biopolymers **14,** 1841–1846 (1975).

[147] R. Townend, T. Kumosinski, S. N. Timasheff, G. D. Fasman, and B. Davidson, "The circular dichroism of the β structure of poly-l-lysine," Biochemical and Biophysical Research Communications **23,** 163–169 (1966).

[148] H. Fischer and O. J. F. Martin, "Engineering the optical response of plasmonic nanoantennas.," Optics express (2008).

[149] R. Pribić, "Principal component analysis of fourier transform infrared and/or circular dichroism spectra of proteins applied in a calibration of protein secondary structure and/or circular dichroism spectra of proteins applied in a calibration of protein secondary st,", 1994.

[150] R. Semenyshyn, F. Mörz, T. Steinle, M. Ubl, M. Hentschel, F. Neubrech, and H. Giessen, "Pushing down the limit : In-vitro detection of a polypeptide monolayer on a single infrared resonant nanoantenna," ACS Photonics submitted (2019).

[151] L. M. Miller and R. J. Smith, "Synchrotrons versus globars, point-detectors versus focal plane arrays: Selecting the best source and detector for specific infrared microspectroscopy and imaging applications," Vibrational Spectroscopy **38,** 237–240 (2005).

[152] R. A. Bosch, "Computed flux and brightness of infrared edge and synchrotron radiation," Nuclear Instruments and Methods in Physics Research, Section A: Accelerators, Spectrometers, Detectors and Associated Equipment **454,** 497–505 (2000).

[153] M. Brehm, T. Taubner, R. Hillenbrand, and F. Keilmann, "Infrared spectroscopic mapping of single nanoparticles and viruses at nanoscale resolution," Nano Letters **6,** 1307–1310 (2006).

[154] X. G. Xu, M. Rang, I. M. Craig, and M. B. Raschke, "Pushing the sample-size limit of infrared vibrational nanospectroscopy: From monolayer toward single molecule sensitivity," Journal of Physical Chemistry Letters **3,** 1836–1841 (2012).

[155] S. Bensmann, F. Gaußmann, M. Lewin, J. Wüppen, S. Nyga, C. Janzen, B. Jungbluth, and T. Taubner, "Near-field imaging and spectroscopy of locally strained GaN using an IR broadband laser," Optics Express **22,** 22369 (2014).

[156] L. Maidment, P. G. Schunemann, and D. T. Reid, "Molecular fingerprint-region spectroscopy from 5 to 12 μm using an orientation-patterned gallium phosphide optical parametric oscillator," Optics Letters **41,** 4261 (2016).

[157] O. Muskens, D. Christofilos, N. Del Fatti, and F. Vallée, "Optical response of a single noble metal nanoparticle," Journal of Optics A: Pure and Applied Optics 8 (2006).

[158] F. Mörz, T. Steinle, A. Steinmann, and H. Giessen, "Multi-Watt femtosecond optical parametric master oscillator power amplifier at 43 MHz," Optics Express **23,** 23960 (2015).

[159] T. Steinle, F. Mörz, A. Steinmann, and H. Giessen, "Ultra-stable high average power femtosecond laser system tunable from 1.33 to 20 μm," Optics letters **41,** 4863–4866 (2016).

[160] M. Chittchang, H. H. Alur, A. K. Mitra, and T. P. Johnston, "Poly(L-lysine) as a model drug macromolecule with which to investigate secondary structure and membrane transport, part I: physicochemical and stability studies," Journal of Pharmacy and Pharmacology **54,** 315–323 (2002).

[161] R. Hartman, R. C. Schwaner, and J. Hermans, "Beta poly(l-lysine): A model system for biological self-assembly," Journal of Molecular Biology **90,** 415–429 (1974).

[162] J. Krauth, H. Giessen, and M. Hentschel, "Wavelength-Dependent Third-Harmonic Generation in Plasmonic Gold Nanoantennas: Quantitative Determination of the d-Band Influence," ACS Photonics **5,** 1863–1870 (2018).

[163] L. V. Brown, X. Yang, K. Zhao, B. Y. Zheng, P. Nordlander, and N. J. Halas, "Fan-shaped gold nanoantennas above reflective substrates for surface-enhanced infrared absorption (SEIRA)," Nano Letters **15,** 1272–1280 (2015).

[164] W. Si and A. Aksimentiev, "Nanopore Sensing of Protein Folding," ACS Nano (2017).

[165] C. Huck, M. Tzschoppe, R. Semenyshyn, F. Neubrech, and A. Pucci, "Chemical Identification of Single Ultrafine Particles Using Surface-Enhanced Infrared Absorption," Physical Review Applied **11,** 1 (2019).

[166] A. Tittl, A. Leitis, M. Liu, F. Yesilkoy, D. Y. Choi, D. N. Neshev, Y. S. Kivshar, and H. Altug, "Imaging-based molecular barcoding with pixelated dielectric metasurfaces," Science **360,** 1105–1109 (2018).

[167] A. Tittl, A. John-herpin, A. Leitis, E. R. Arvelo, and H. Altug, "Metaoberflächen-basierte molekulare Biosensorik unterstützt von künstlicher Intelligenz," Angewandte Chemie **131,** 2–16 (2019).

[168] B. Schuler, L. Kühner, M. Hentschel, H. Giessen, and C. Tarín, "Adaptive Method for Quantitative Estimation of Glucose and Fructose Concentrations in Aqueous Solutions Based on Infrared Nanoantenna Optics," Sensors **19,** 3053 (2019).

[169] D. J. Irwin, V. M. Y. Lee, and J. Q. Trojanowski, "Parkinson's disease dementia: Convergence of α-synuclein, tau and amyloid-β pathologies," Nat Rev Neurosci. **14,** 626–636 (2013).

[170] M. L. Brongersma, N. J. Halas, and P. Nordlander, "Plasmon-induced hot carrier science and technology," Nature Publishing Group **10,** 25–34 (2015).

Acknowledgements

Like many things in life and world, this thesis and the work presented in this dissertation could not have been accomplished without the help of others. Therefore I am deeply grateful to many people who contributed scientifically or in one of many other ways, and supported me during this time:

- Prof. Dr. Harald Giessen for giving me the opportunity to work at his institute, for his advices, all the contacts he made, and his great support.
- Prof. Dr. Stefanie Barz and Prof. Dr. Christian Holm for taking their time and kindly agreeing to be part of my examination committee.
- Dr. Frank Neubrech for supervising me from the first days at the institute, help during the dissertation writing, and sharing lots of skills as well as knowledge.
- Dr. Mario Hentschel who provided essential help and good advices at numerous occasions and was involved in basically every project.
- Dr. Christine von Rekowski for all administrative affairs.
- Dr. Hans-Christian Sigg, Dr. Christoph Stanglmair, Dr. Felix Weiher, Dr. Jochen Vogt, Dr. Christian Huck for the great collaboration.
- Florian Mörz for the great team work in the Single Nanoantenna Sensing project.
- Dr. Maxim Nesterov, Steffen Both, Ramon Walter, Dr. Bettina Frank for being great officemates.
- Dr. Mario Hentschel, Dr. Bettina Frank for their kind support and help during the dissertation writing process.

- Josselin Defrance and Florian Sterl for their support on Blender visualization.
- Dr. Maxim Nesterov and Izzatjon Allayarov for the numerous interesting non-scientific discussions.
- Monika Ubl, Philipp Flad, Michael Kube, and Ramon Walter for all technical stuff in the clean room.
- All current and former members of the 4th Physics Institute for the nice working atmosphere.
- My friends Jasmin Stöhr Lindenmeyer and David Coughtrie, who read this dissertation and found numbers of typos.
- My friends Dr. Oleksii Laguta, Dr. Leonid Solianyk, Pavlo Soroka, Dr. Dmytro Bozhko, Dr. Olha Popova for their support and great times together.
- My parents Nadia and Volodymyr as well as my brother Roman for the unconditional support in every possible sense for a many years.
- My wife Iryna who shares all the good and bad times with me and has been with me all these years.

COLOPHON

This document was typeset using the typographical look-and-feel classicthesis developed by André Miede. The style was inspired by Robert Bringhurst's seminal book on typography "*The Elements of Typographic Style*". classicthesis is available for LaTeX.

Cover image is rendered using free and Open 3D Creation Software, Blender, with the help of Josselin Defrance.